

## Role of ions and interfaces for efficient and stable perovskite solar cells

Présentée le 22 novembre 2021

Faculté des sciences de base  
Laboratoire de photonique et interfaces  
Programme doctoral en chimie et génie chimique

pour l'obtention du grade de Docteur ès Sciences

par

**Anand AGARWALLA**

Acceptée sur proposition du jury

Prof. U. Röthlisberger, présidente du jury  
Prof. M. Graetzel, Prof. U. A. Hagfeldt, directeurs de thèse  
Prof. F. Sauvage, rapporteur  
Prof. J. P. Correa, rapporteur  
Prof. M. K. Nazeeruddin, rapporteur

## Acknowledgments

I would first like to thank my thesis director **Prof. Graetzel** for being patient and understanding with me while I was struggling with my mental health and guiding me to the right direction to regain motivation to finish my PhD. Your persistence is the reason I was able to get an extension and I will forever be indebted to you for that. I wish I had more time to work under your supervision to learn from you but in the short period you demonstrated to me how a person should lead and that above all is something I will cherish for the rest of my life. I also thank you for all your scientific inputs in the final phase of my thesis making my thesis something I can be proud of.

I would like to thank my thesis co-director **Prof. Hagfeldt** for providing me the opportunity to work in one of the best labs with some of the best minds on this planet. You were always supportive of my work and provided me with every resource I desired. Even after leaving EPFL, you helped me in my extension and I thank you for that. I also thank you for backing me and my work in the toughest of the times.

Thank you to the jury members for this thesis, Prof. Ursula, Prof. Nazeeruddin, Prof. Frederic and Prof. Juan Pablo for your time and evaluation.

of my work. I would like to thank **Prof. Zakeer** for looking out for me when I was struggling. Thanks for organising regular meetings to push me in the right direction. **Dr. Anurag**, you were my pillar in the final months of my PhD. Without your support and guidance, I would not have managed to get all the experiments done, for which I thank you from the bottom of my heart. You helped me in all aspects of my work as well provided me with valuable life lessons. I aspire to be like you and hope to get to work with you again in the future.

The administrative staff have been wonderful throughout my PhD for which I would like to thank **Anne Lene, Heidi, Cecile** and **Carmen**. Thank you all for making things smoother for me by communicating information promptly whenever required. I would specially like to thank **Anne Lene** for looking out for me in regards to my academic work as well as assigning me a mentor when I really needed one. I would like to thank **Prof. Berend Smit** for being a friendly mentor and advocating and helping me with my extension.

**Brian, Essa, Anwar, Thomas** and **Algirdas** thank you all for being amazing colleagues. I appreciate all discussions we had be it scientific or non-scientific. Thank you all for assisting

me whenever I needed any help. I hope I was of help to you guys too at some point. I want to thank Brian specially for not only being a great colleague but also a good friend. Thank you for introducing me to climbing, I hope I continue doing it so I can join you in one of your trips that always terrify me.

What makes our lab one of the best in the world is the amazing talents we have in our post docs. I want to take this opportunity to thank all the post-docs individually with whom I had the privilege to work with. Thank you **Dr. Simone** and **Dr Alexander** for your valuable contribution to my research and enabling me to understand a lot about fundamentals of the field. Thank you **Dr. Jovana** for teaching me a lot about organic chemistry and imparting some of your writing skills to me. You are one of the most professional and disciplined person I have ever met and I wish I can adopt a fraction of those qualities from you. Thank you **Dr. Felix** for teaching me a few things about semiconductor physics which I was then able to apply to my work. I am also indebted to you for all your help in the final phase of my PhD. Thank you **Dr. Haizhou** for trusting me with some of your work and allowing me to work in your lab where I was able to obtain some of my best results. Thanks a lot for always being there to answer any queries I had which made it really easy for me to conduct experiments. **Dr Hong**, thank you for teaching me the intricacies of experimental work and providing me with useful information which helped me get better results. **Dr Ibrahim Dar**, for the hospitality on my arrival to EPFL as well as being available for any discussion even after leaving EPFL.

I want to thank my family for all their support. Covid was not easy but it would have been worse if my parents did not motivate me. The last 4 years have seen a lot of ups and downs but one thing has been constant, your love for me and mine for you. Thank you to my brother and sister-in-law for their words of support and encouragement. And my newly born niece for bringing a big smile to my face whenever I see you. You have brought a new meaning to my life and I cannot wait to see you after all of this is done.

I would like to thank Natacha for being there for me whenever I was down. Without you none of this would have been possible. You were there when I wanted someone to listen, you were there when someone needed to talk to me. You took my challenges as your own and helped me become a better person. Finally, I want to thank all my friends and past teachers/professors who in their own way have given shape to me. I know I have room to

grow and I promise I will take this experience and become a better person professionally and personally.

## Abstract

Perovskite Solar Cells (PSCs) have grabbed global attention of the researchers due to their outstanding Photovoltaic (PV) performance. PSCs have the potential to be the future of the PV technology as they can generate power with performance being comparable with the leading Silicon solar cells, with the cost being lower than Silicon solar cells. The enormous potential of PSCs is evident from the fact that the efficiency of these cells has risen from 3.8% to 25.5% within a decade, and it is continuously rising to date.

In my thesis, I investigate the impact of ions in the bulk of perovskite and also look at the ETL-perovskite interface to create a simpler, more efficient, more reproducible and more stable system for PSCs. At first, I managed to achieve high efficiency devices with the standard triple cation perovskite on both planar and mesoporous n-i-p ETL device architecture. Adding KI to the already established compositions showed a boost in performance of the solar cells while significantly reducing hysteresis. We then performed a systematic study of KI on various perovskite compositions comprised of FA, MA, Cs, Rb, I and Br ions. We demonstrated that KI reacts with the bromide ions in perovskite passivating the grains leading to a red shift hence and improvement in current density as well as efficiency.

MAPbBr<sub>3</sub> is generally used in small proportions along with FAPbI<sub>3</sub> to stabilise the phase of FAPbI<sub>3</sub>. But the effect of Br<sup>-</sup> ions on the perovskite performance was relatively unknown. The introduction of Br<sup>-</sup> ions in the lattice causes a blue shift in the band gap pushing it further away from the ideal Shockley-Queisser limit. On top of this, the effect of MAPbBr<sub>3</sub> on phase stability of FAPbI<sub>3</sub> is similar to the effect of CsPbI<sub>3</sub>. This led me to examine the impact of reduced bromine concentration on the device performance. Interestingly, reducing the bromine concentration not only leads to a red shift in band gap, hence increasing the current density but also causes a reduced voltage loss resulting in much superior performance. Moreover, the Br<sup>-</sup> ions cause increased halide diffusion in the bulk leading to decreased stability with higher the bromide concentration.

While perovskite composition plays an important role in defining the device characteristics, it could be argued that the interfaces play an equally important role in doing the same. With the rise in usage of SnO<sub>2</sub> as a viable substitute for TiO<sub>2</sub> as ETL, I explore the effect of using TiO<sub>2</sub> particles that exhibit similar properties to the SnO<sub>2</sub> particles. These smaller size TiO<sub>2</sub> nanoparticles can form a very thin, compact, uniform and pin-hole free layer with a

morphology that follows the morphology of FTO. This results in a reduced recombination in the interface of  $\text{TiO}_2$  and perovskite causing the open circuit voltage and hence the device performance to improve significantly.

## Résumé

Les cellules solaires à perovskite ont attiré l'attention des chercheurs du monde entier grâce à leurs performances photovoltaïques exceptionnelles. Les cellules solaires à perovskite pourraient être l'avenir de la technologie photovoltaïque, car elles peuvent générer de l'énergie avec des performances comparables à celles des principales cellules solaires en silicium, tout en étant moins chères que ces dernières. L'énorme potentiel des cellules solaires à perovskite est évident, comme le prouve l'augmentation de l'efficacité de ces cellules, qui est passée de 3,8% à 25,5% en une décennie, et qui continue d'augmenter encore aujourd'hui.

Dans ma thèse, j'analyse l'impact des ions dans la masse de perovskite et je m'intéresse également à l'interface ETL-perovskite pour créer un système plus simple, plus efficace, plus reproductible et plus stable pour les cellules solaires à perovskite. Tout d'abord, je suis parvenu à mettre au point des dispositifs à haute efficacité avec la perovskite à triple cation standard, sur des architectures de dispositif n-i-p ETL à la fois planaire et mésoporeux. L'ajout de KI aux compositions déjà établies a permis d'améliorer les performances des cellules solaires tout en réduisant considérablement l'hystérésis. Par la suite, nous avons effectué une étude systématique du KI sur diverses compositions de perovskite composées d'ions FA, MA, Cs, Rb, I et Br. Nous avons démontré que le KI réagit avec les ions bromure dans la perovskite en passivant les grains, ce qui entraîne un décalage vers le rouge et une amélioration de la densité de courant ainsi que de l'efficacité.

Le  $\text{MAPbBr}_3$  est généralement utilisé dans de petites quantités avec le  $\text{FAPbI}_3$  pour stabiliser la phase de  $\text{FAPbI}_3$ . Mais les effets des ions Br sur les performances de la pérovskite étaient relativement inconnus. L'introduction d'ions Br dans le réseau provoque un décalage vers le bleu dans la band gap, l'éloignant davantage de la limite idéale de Shockley-Quessier. Par ailleurs, l'effet du  $\text{MAPbBr}_3$  sur la stabilité de la phase de  $\text{FAPbI}_3$  est similaire à l'effet du  $\text{CsPbI}_3$ . Cela m'a conduit à examiner l'impact d'une concentration réduite de bromure sur les

performances de l'appareil. Il est intéressant de noter que la réduction de la concentration de bromure entraîne non seulement un décalage vers le rouge de la band gap, augmentant ainsi la densité du courant, mais elle provoque également une réduction de la perte de tension, qui résulte en des performances bien supérieures. De plus, les ions Br déclenchent une diffusion accrue des halogénures dans la masse conduisant à une stabilité réduite avec une concentration de bromure plus élevée.

Alors que la composition de la perovskite joue un rôle important dans la définition des caractéristiques de l'appareil, on pourrait affirmer que les interfaces jouent un rôle tout aussi important à cet égard. Avec l'augmentation de l'utilisation du SnO<sub>2</sub> comme substitut viable du TiO<sub>2</sub> en tant que ETL, j'explore l'effet de l'utilisation de particules de TiO<sub>2</sub> qui présentent des propriétés similaires à celles des particules SnO<sub>2</sub>. Ces nanoparticules TiO<sub>2</sub> de plus petite taille peuvent former une couche très mince, compacte, uniforme et dépourvue de trous avec une morphologie qui suit celle du FTO. Cela se traduit par une recombinaison réduite dans l'interface du TiO<sub>2</sub> et de la perovskite, ce qui entraîne une amélioration significative de la tension en circuit ouvert et donc des performances de l'appareil.

## *Keywords*

CB	Chlorobenzene
DMF	N,N-dimethylformamide
DMSO	Dimethylsulfoxide
ETL	Electron transport layer
HTL	Hole transport layer
FF	Fill Factor
FTO	Flourine-doped Tin Oxide
IPCE	Incident photon-to-current conversion efficiency
JV	Photocurrent-Voltage
$J_{sc}$	Current density
Mp-TiO <sub>2</sub>	mesoporous Titanium oxide



## Table of Contents

<b>Acknowledgments</b> .....	2
<b>Abstract</b> .....	5
<b>Résumé</b> .....	6
<b>Keywords</b> .....	8
<b>Chapter 1. Introduction</b> .....	11
Perovskite as light absorber .....	11
Device architecture and Electron transport layer .....	16
TiO <sub>2</sub> as ETL .....	17
<b>Chapter 2: Impact of KI on various perovskite compositions</b> .....	19
Introduction .....	19
Basic characterisation .....	21
JV data .....	22
Stability .....	24
Conclusion .....	26
Supplementary Information .....	27
Comparing 3,4 and 5 cation perovskite composition JV performance parameters .....	30
Comparing different perovskite composition JV performance parameters .....	32
<b>Chapter 3: Reduced halide diffusion in triple cation perovskite solar cells for improved charge extraction and operational stability (to be submitted, abstract under preparation)</b> .....	34
Motivation .....	34
Introduction .....	34
Basic characterisation .....	35
Impedance Spectroscopy .....	37
DFT calculations .....	39
Device performance .....	43
Stability .....	45
Conclusion .....	46
Supplementary Information .....	46
<b>Chapter 4: TiO<sub>2</sub> colloids as low temperature alternative to mesoporous TiO<sub>2</sub></b> .....	61
Motivation .....	61
Introduction .....	61
Nanoparticle properties .....	63
Results and discussions .....	64
Conclusion .....	70

Experimental section .....	70
<b>Chapter 4. Experimental procedure</b> .....	72
Substrate preparation.....	72
Deposition of hole transporting layer.....	72
Perovskite film characterization .....	72
<i>J-V</i> measurements.....	73
IPCE measurements .....	73
Electrochemical impedance spectroscopy (EIS) .....	73
Stability measurements .....	73
<b>References</b> .....	75
<b>Curriculum Vitae</b> .....	88

## Chapter 1. Introduction

$\text{CH}_3\text{NH}_3\text{PbI}_3$  as a suitable perovskite light absorber was first introduced by Miyasaka et.al.<sup>1</sup> Since then, PSCs have rapidly improved with certified efficiencies of 25.5% (**Fig 1**).<sup>2</sup> These materials show excellent optical and electronic properties for photovoltaic applications and could be a cheaper alternative to existing silicon technologies.<sup>3</sup> This has sparked enormous interests in this field. But because of the novelty of the field, there is a lot still needed to be understood about these materials and the different factors that affect its performance in a device. In my thesis, we look into the effect of various components in the composition of perovskite as well as the effect of the ETL-perovskite interface on PSCs.

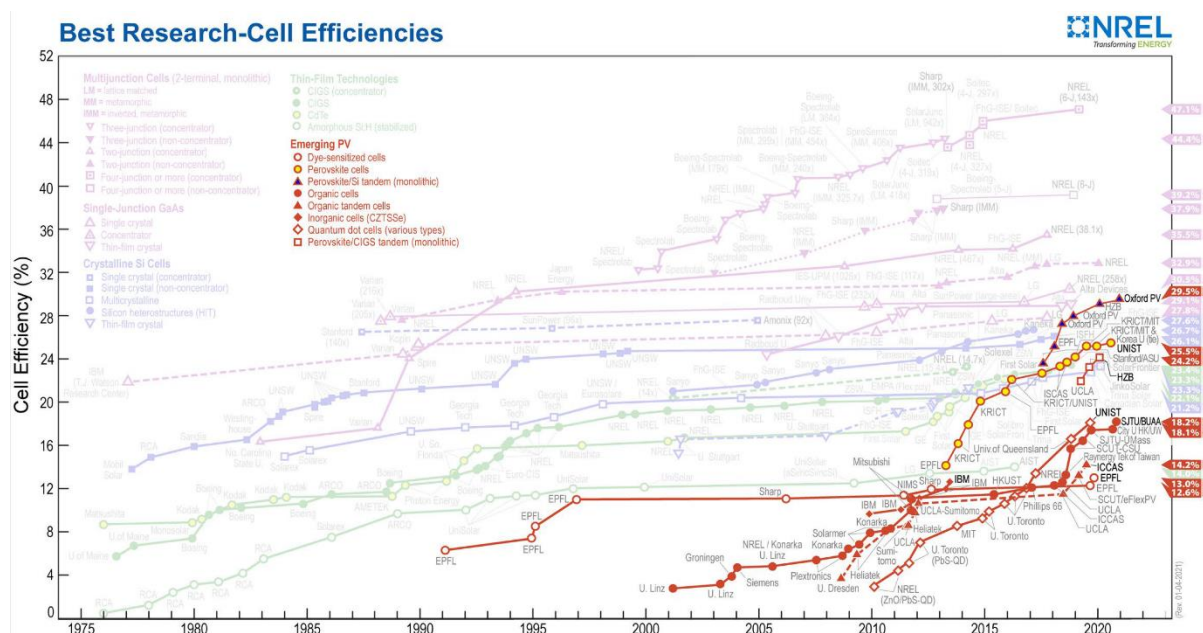


**Fig 1.** NREL chart of efficiency showing the current record efficiency for perovskite held by UNIST at 25.5% followed closely by EPFL at 25.4%.

### Perovskite as light absorber

Perovskite crystal is a cubic  $\text{AMX}_3$  structure, where A generally is an organic cation, M is a divalent metal and X is a halide (A = aliphatic or aromatic ammonium, M =  $\text{Pb}^{2+}$ ,  $\text{Sn}^{2+}$ , X = Cl<sup>-</sup>, Br<sup>-</sup>, I<sup>-</sup>). In an ideal perovskite structure featuring cubic-symmetry, the M cation is in 6-fold coordination, surrounded by an octahedron of anions ( $\text{MX}_6$ ), while A cation is 12-fold coordinated. The  $\text{MX}_6$  octahedra constitute a three-dimensional network in which they share

corners with each other. Within this framework, the A cations fill in the space between the octahedra, balancing the charge of the entire network. Based on the space available in the octahedra, one can choose an appropriate A cation. Goldschmidt derived a general formula for cubic perovskites called the Goldschmidt tolerance factor  $t^4$  (Eq.1) which can be used to determine whether an A cation can form perovskite given the M and X elements. The equation is as follows:

$$t = \frac{r_A + r_X}{\sqrt{2}(r_M + r_X)} \quad \dots\dots Eq1$$

where r is the corresponding ionic radius in an  $AMX_3$  perovskite

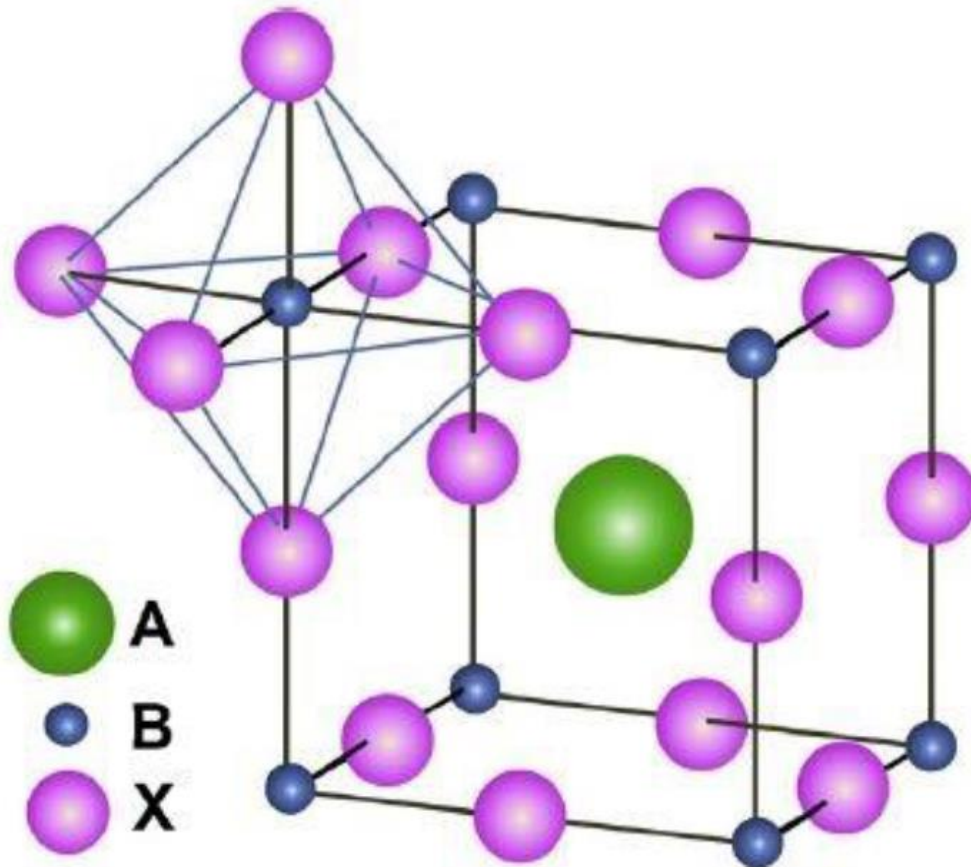


**Fig 2.** The schematic diagram of perovskite crystal structure  $ABX_3$ , where A is monovalent cation, B is a divalent metal cation and X is an anion. Adapted from Ref<sup>5</sup>

After over a decade of research we have established that for the most efficient PSCs, A is either  $\text{CH}_3\text{NH}_3$  (methyammonium or MA),  $\text{NH}_2(\text{CH})\text{NH}_2$  (formamidinium or FA) or a mix of both; M is Pb and X is predominantly Iodine mixed with some bromine. Initial success in the field of PSC was obtained with  $\text{MAPbI}_3$  (MAPI). MAPI in the cubic phase<sup>6</sup> (**Fig 3 (a)**) showed high absorption coefficient ( $10^4 - 10^5 \text{ cm}^{-1}$ )<sup>7,8</sup>, a bandgap of around  $1.59 \text{ eV}^{9-11}$ , and an exciton binding energy less than  $50 \text{ meV}^{12}$ . This along with facile low temperature crystallisation allowed MAPI to obtain efficiencies between 10-15%<sup>13,14</sup> swiftly. Around the same time period researchers discovered  $\text{FAPbI}_3$  (FAPI)<sup>15,16</sup>. FAPI showed slightly lower bandgap which made it a better candidate as an absorber material since theoretically it was closer to the Shockley-Queisser limit due to its larger size (**Fig 3 (b)**) which distorts the lattice hence reducing the bandgap<sup>17,18</sup> (**Fig 4**).

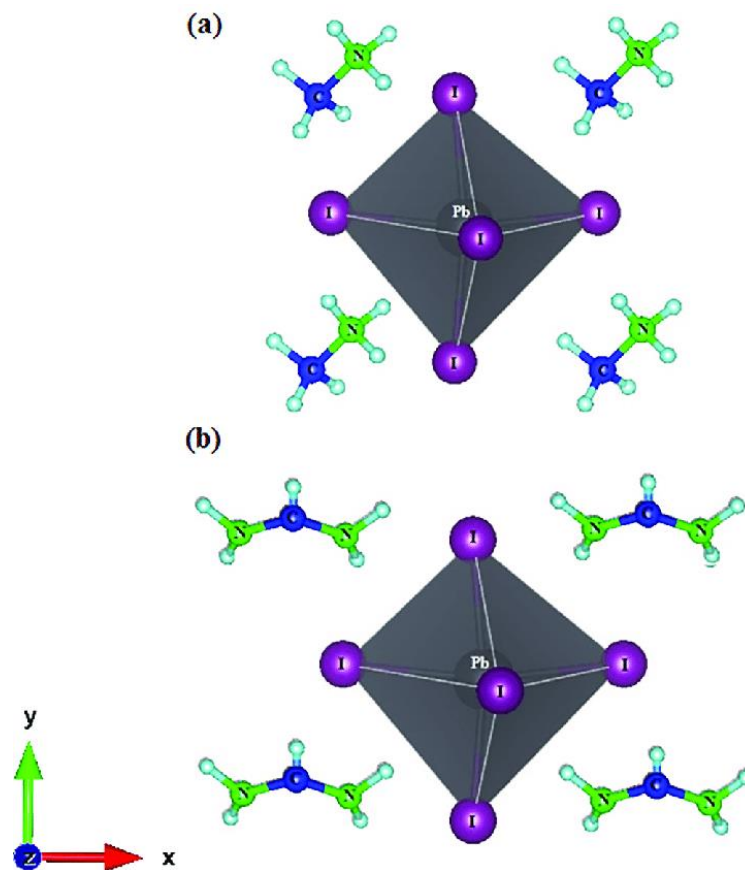


**Fig 3.** Crystal structure of **(a)** MAPI and **(b)** FAPI. Taken from Ref<sup>19</sup>

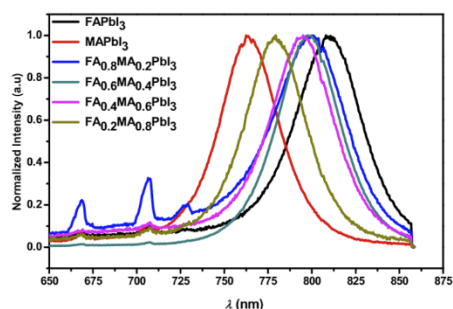


Table 1. Estimated bandgap from PL for different MA and FA ratio

Perovskites	$E_g$ (Abs) (eV)	$E_g$ (PL) (eV)
FAPbI <sub>3</sub>	1.502	1.531
FA <sub>0.8</sub> MA <sub>0.2</sub> PbI <sub>3</sub>	1.507	1.547
FA <sub>0.6</sub> MA <sub>0.4</sub> PbI <sub>3</sub>	1.514	1.569
FA <sub>0.4</sub> MA <sub>0.6</sub> PbI <sub>3</sub>	1.530	1.572
FA <sub>0.2</sub> MA <sub>0.8</sub> PbI <sub>3</sub>	1.554	1.584
MAPbI <sub>3</sub>	1.563	1.604

**Fig 4.** PL emission for different MA and FA ratio showing a red shift for pure FA compositions. Taken from Ref<sup>20</sup>

Although FAPI and MAPi both show tremendous light absorption ability<sup>21</sup>, the interaction of FA cations with the surrounding PbI<sub>6</sub> octahedra was stronger than that of MA cations due to the higher probability of forming hydrogen bonds<sup>22</sup>. It can also be demonstrated that the substitution of MA<sup>+</sup> with FA<sup>+</sup> cations inside the inorganic cage leads to greater robustness for the overall lattice and extends the material durability due to a different interaction between the organic molecules and the inorganic cage<sup>23</sup>. As a result, the perovskite phase ( $\alpha$ -phase, cubic) of FAPI may be a better solar material than MAPi, due to the improved stability<sup>24,25</sup> and lower bandgap<sup>26,27</sup>.

Even though  $\alpha$ -FAPI (**Fig 5a**) is the desired phase, unfortunately  $\alpha$ -FAPI transforms spontaneously into the undesirable  $\delta$ -FAPI (**Fig 5b**) at room temperature<sup>28–30</sup>, which hindered its practical application in stable photovoltaic devices. To stabilize the  $\alpha$ -FAPI perovskite lattice, cesium cations (Cs<sup>+</sup>)<sup>31</sup>, which have a smaller ionic radius and stability against heat are partially replaced with FA<sup>+</sup><sup>32</sup>. Addition of Cs not only improved the stability of the phase but it also helped in improving device performance<sup>33</sup>. Following this Saliba et.al<sup>34</sup>. showed that adding Rb along with Cs can further improve stability as well as efficiency. In chapter 1 of my thesis, we look at the impact of further adding KI in perovskite.

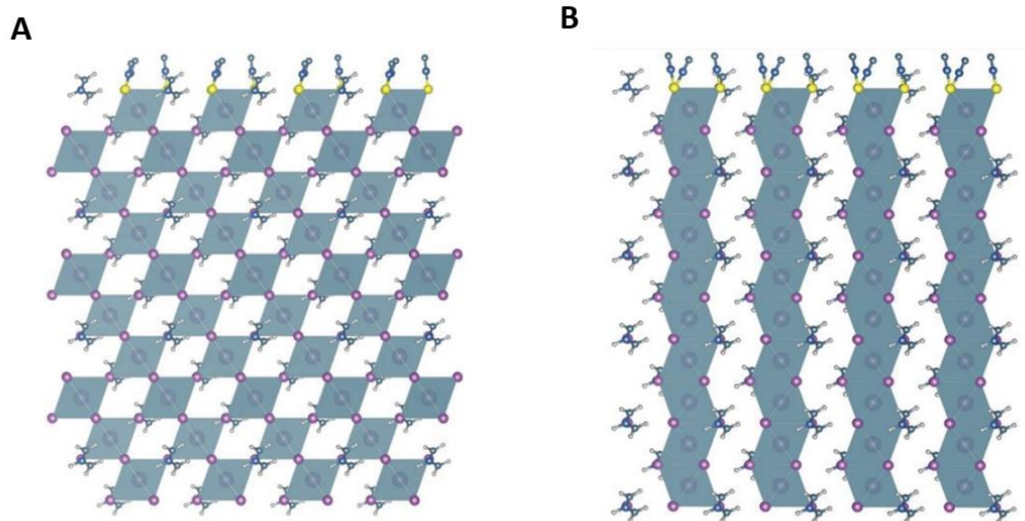


**Fig 5.** Schematic of the lattice structure of FAPI perovskite in **A.**  $\alpha$  and **B.**  $\delta$  phase. Taken from ref<sup>35</sup>

Mixing halides ( $\text{Cl}^-$ ,  $\text{I}^-$  and  $\text{Br}^-$ ) is another approach that was used to tune the bandgap of perovskite (**Fig 6**) while also stabilising the phase of FAPI<sup>36,37</sup>. But in recent studies we have seen that reducing the quantity of  $\text{Br}^-$  and driving the composition as close as possible to pure FAPI could not only improve the device efficiency due to lower bandgap but also improve the stability of the device<sup>38,39</sup> implying that the role of halide ions is still not very clear. A lot of different strategies are employed to stabilise the devices including introducing hydrophobic 2D organic molecules in the bulk of perovskite<sup>40,41</sup> to passivate the perovskite grains and interfaces to treating the interfaces themselves<sup>42,43</sup> to create a more stable architecture which prevents destructive interaction with the surroundings. But it is without a doubt that perovskite composition is a key factor in defining its ability to perform as a durable and efficient solar cell. In chapter 2 of my thesis, we look at the role of bromide ions in the perovskite composition.



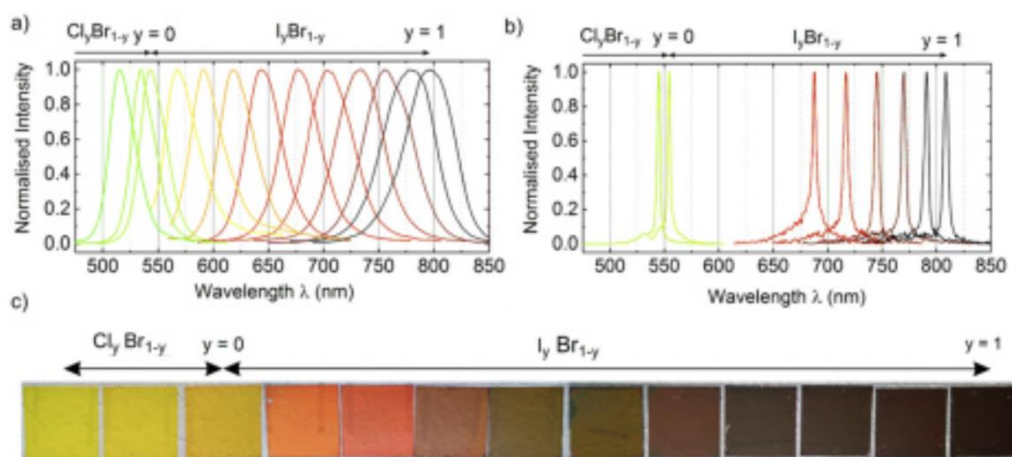


**Fig 6.** PL spectra of triple cation perovskites with halide compositions ranging from  $\text{Cl}_{0.2}\text{Br}_{0.8}$  to  $\text{I}_{1.0}$ . Taken from Ref<sup>31</sup>

### Device architecture and Electron transport layer

PSC devices are composed of mainly a n-i-p structure where the perovskite layer acts as the light absorber and the light enters through the n-type layer. The typical device architecture is composed of six layers, namely (1) transparent electrode (commonly fluorine-doped tin oxide, FTO), (2) n-type semiconductor as electron transporting layer (ETL), (3) photoactive perovskite, (4) p-type semiconductor as hole transporting layer (HTL) and (5) the metallic electrode (commonly gold, silver or carbon).

The most important characteristic of an ETL is that it must satisfy the band alignment requirement with the perovskite layer<sup>44</sup>, i.e. it should have the energy level of the lowest unoccupied molecular orbital (LUMO) slightly below and highest occupied molecular orbital (HOMO) below that of the perovskite active layer. It must have high transmittance in the UV-Vis region so that a photon can pass through easily and be absorbed by the perovskite absorber. On top of that the ETL morphology plays a key role in the growth of perovskite crystals<sup>45–47</sup>.



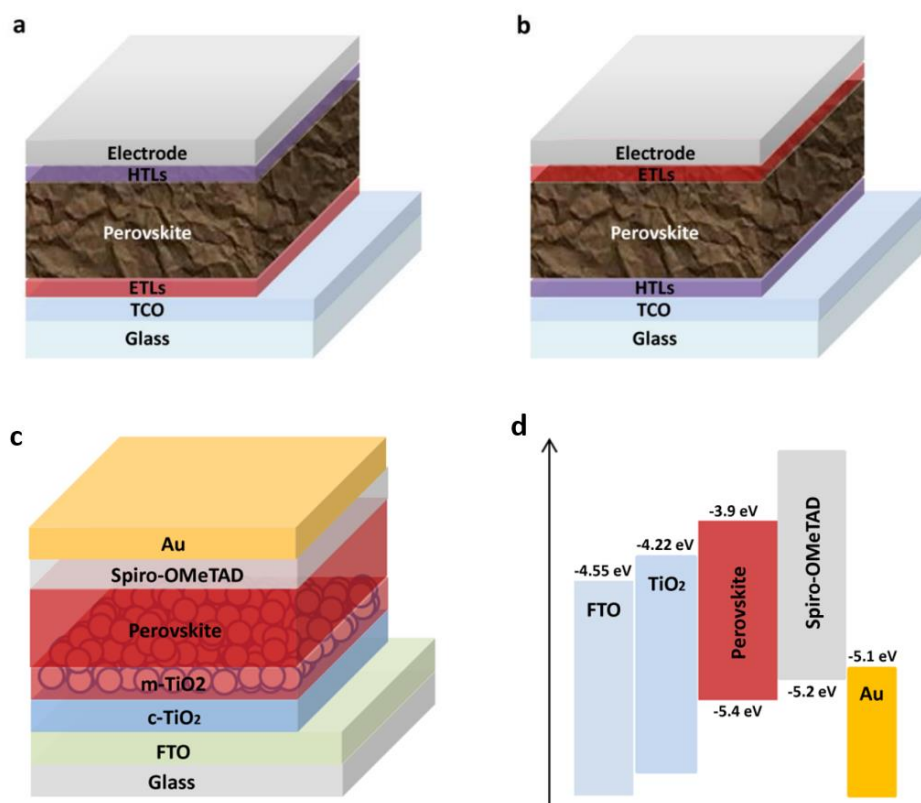


**Fig 7.** Schematic of **(a)** n-i-p architecture **(b)** p-i-n architecture **(c)** n-i-p architecture with mesoporous  $\text{TiO}_2$  and **(d)** Band diagram for the device structure with  $\text{TiO}_2$ . Taken from Ref<sup>48</sup>

### $\text{TiO}_2$ as ETL

$\text{TiO}_2$  was first popularised as a photoanode in DSSC<sup>49,50</sup> which then led to its usage in PSCs as well. The photoanode was composed of a thin compact  $\text{TiO}_2$  layer<sup>51</sup> covered by a thicker  $\text{TiO}_2$  mesoporous<sup>52</sup> film. There are various ways of depositing the compact layer which includes ALD deposition<sup>53</sup>, spin coating<sup>54</sup>, thermal oxidation<sup>55</sup>, electrochemical deposition<sup>56</sup> or spray pyrolysis<sup>57</sup>. Spray pyrolysis is the most popular method as it is scalable, fast, cheap and effective. The mesoporous film however, is deposited by spin coating. In general, for effective carrier extraction the layers are in anatase phase. To achieve this phase the layers are generally annealed at high temperature ( $450^\circ\text{C}$ )<sup>58</sup>. Even though  $\text{TiO}_2$  is well established it suffers from various issues such as unwanted surface recombination<sup>59</sup>, UV light degradation<sup>60</sup> and use of high temperature for film formation<sup>61</sup>. All these factors make it essential to look for alternatives for  $\text{TiO}_2$  or modify the  $\text{TiO}_2$  to avoid the above-mentioned issues. In chapter 3

of my thesis, we look at one such alternative and explore the impact of the size of  $\text{TiO}_2$  on its performance as an ETL.

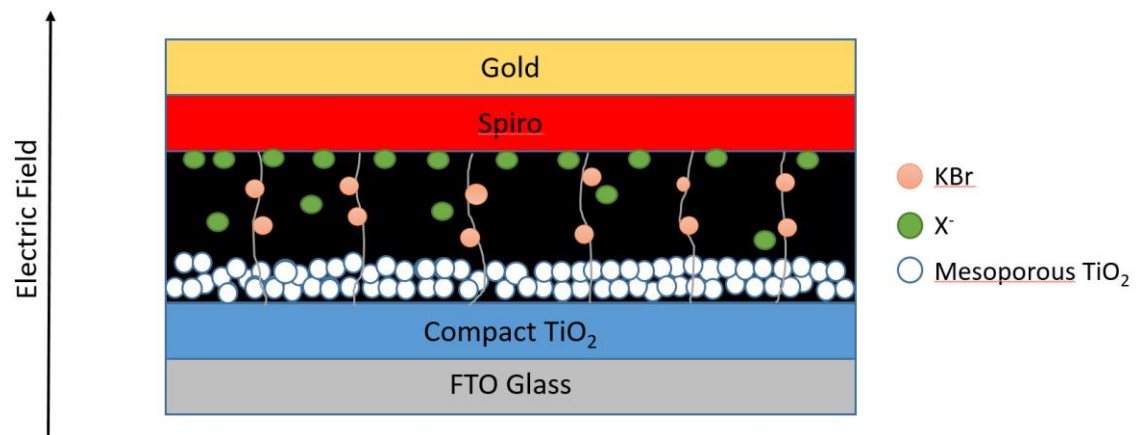


**Fig 8.** Representative image of all 3 chapters where the KBr settles on the grain boundaries, the halide ions mobilise towards the top interface of perovskite due to an electric field and defects form at the mesoporous  $\text{TiO}_2$  and perovskite interface.

## *Chapter 2: Impact of KI on various perovskite compositions*

### Introduction

Perovskite solar cells (PSCs) have attracted tremendous attention in recent years due to an unprecedented rise in power conversion efficiencies (PCEs) from 3.9%<sup>1</sup> in 2009 to now 25.5%<sup>2</sup>. These perovskite materials are  $ABX_3$  structures where A = methylammonium (MA), formamidinium (FA), or Cs; B = Pb or Sn; X = Cl, Br, or I. The solution processability of perovskites make them a very attractive candidate for commercialization. However, long-term stability and the ever-daunting danger of hysteresis caused by migration of highly mobile ions<sup>62</sup> still preclude PSCs from commercialisation. Thus far, the highest efficiency devices contain a mesoporous  $TiO_2$  layer sintered at high temperature up to 450 °C. Currently, the so-called planar configuration, which does not have a mesoporous layer and high-temperature sintering, produces slightly lower efficiencies at a certified 23.3% using, for example, a planar  $SnO_2$  layer<sup>42</sup>.

For a one-step deposition method, one of the highest efficiency and stability reported uses a cation mixture of Rb, Cs, MA, and FA. Cs was shown to improve the phase stability of FAMA perovskites by reducing yellow phase impurities<sup>33</sup> which was further improved by adding Rb<sup>63</sup>. The resulting perovskites have higher recombination resistance<sup>64</sup> and improved device performances as well as one of the highest open-circuit voltages ( $V_{oc}$ ) at 1.24 V (for a band gap of 1.63 eV)<sup>34</sup>. Improving the Rb-containing perovskites is challenging since the device parameters are relatively high already. Moreover, so far the transition towards a planar architecture has not been achieved which often suffer from lower photocurrents, hysteresis and a lower fill factor.

The motivation for adding Rb was inspired by increasing entropy in order to achieve a phase-stable, photoactive “black phase”. Thus, we explore the use of an additional cation, i.e. potassium (K) as it is oxidation stable and only slightly smaller than Rb. The introduction of K is counter-intuitive because it forms only the yellow  $ABX_3$  given its very low tolerance factor  $t$  (Eq1) which is a geometrical measure for lattice distortion. However, similar to Rb, which by itself does not form a black phase, K can also aid the phase stability by passivating the grain boundaries while at the same time improving the film morphology. This has been reported by various groups using KI in FAMA and FAMACs with PCEs of over 20%.<sup>65,66</sup>

$$t = \frac{r_A + r_X}{\sqrt{2(r_M + r_X)}} \quad \dots\dots Eq1$$

In this work, we explore the multi-cation theme fully using K systematically to map out all the feasible compounds, i.e. KFA, KMAFA, KCsFA, KRbFA, KCsRbFA, KCsMAFA, KRbMAFA and KRbCsMAFA. For this, we adopt a conventional n-i-p architecture comparing mesoporous TiO<sub>2</sub> and planar SnO<sub>2</sub> electron transport layers (ETLs) with glass/fluorine-doped tin oxide/ETL - /mesoporous TiO<sub>2</sub>/perovskite/spiro-OMeTAD/Au. We observe higher efficiencies using KI in each of the above mentioned architectures as shown in (Supplementary information). Interestingly, as previously reported, the highest efficiencies followed the trend of higher complexity, in our case the KI with FAMACs and FAMACsRb perovskites. The KI in FAMACsRb mixture resulted in a PCE of 21.7% (slightly higher than quadruple). More importantly, using K reduced hysteresis drastically, which is a particular challenge for planar PSCs. This shows that K addition offers added, unexpected advantages. Hence, we investigate the 4 and the 5 cation systems in detail.

In order to understand the effect of K<sup>+</sup> cation in perovskite we studied all the FA based perovskite composition because FA is thermally more stable than MA and has a more favourable bandgap with the highest efficiencies in literature having been reported with predominantly FA based perovskites<sup>9,67</sup>. Hence, we studied a total of eight compositions all containing FA and K. We found that for higher number of A type cations i.e. more complex systems, the effect of KI on device parameters could be clearly observed. To further understand this, we characterised all the different compositions using PL, UV-Vis and XRD.

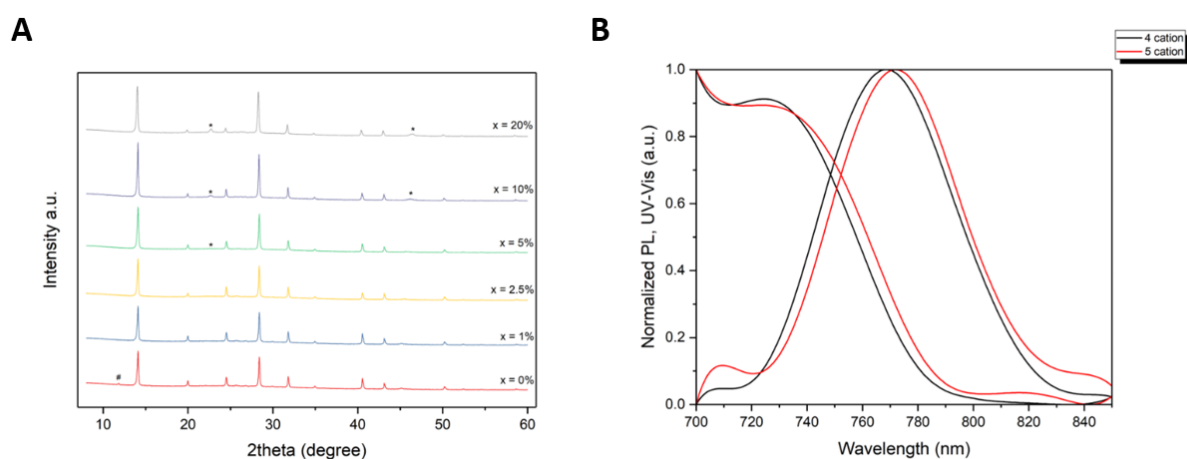
It is well reported that FAPbI<sub>3</sub> forms a photoinactive yellow  $\delta$ -phase at room temperature<sup>68,69</sup>. To stabilize the black perovskite phase, mixed cation MA and FA was used which exhibited PCEs of over 25%<sup>70</sup>. However, even with MA, often impurities remain<sup>71,72</sup>. An introduction of Cs at the A-site in this mixed perovskite improves the thermal stability of the perovskite and provides devices with both high efficiency and improved stability<sup>33</sup>. There are reports that incorporation of K can also suppress the photoinactive  $\delta$ -phase<sup>73</sup>. We noticed that the introduction of KI in the perovskite suppressed the  $\delta$ -phase for quadruple (see Supplementary Information) and quintuple (Fig 1A) perovskite composition. This shows that KI has a

stabilizing effect on the phase of the perovskite. We also do not see any shift in the peak positions implying that the potassium does not go into the lattice which is similar to what has already been reported for Rubidium and Potassium<sup>74,75</sup>. Furthermore, (Supp Info) we observe that for perovskite compositions with bromine in it the peaks of excess KI is found only for higher concentrations (more than 10 mol%) for KI whereas for no-bromine systems we could observe excess KI even at 5% concentration of KI for certain compositions. This further illustrates the hypothesis that K reacts with Br and is not a substantial part of the actual perovskite lattice.

## Basic characterisation

We performed PL and UV-Vis measurements for all the above-mentioned compositions (Supp figure). We notice a visible red-shift for the PL peak position and also the absorption on-set (see Fig 1B) which is in line with the PL<sup>76</sup> and UV-Vis<sup>77</sup> measurements already reported with KI doping in perovskite. We notice a similar nature as in XRD where the perovskite compositions containing bromine show the red shift for KI incorporation whereas the compositions without bromine had no shift.

Scanning electron microscopy (SEM) top surface images were taken (Fig 1C & 1D). We found that potassium incorporation improves the grain size significantly compared to 4 cation (CsMAFARb) perovskite which is similar to the effect of Rubidium on the film crystallinity but better. Thus, we conclude, that morphology improvement is an additional benefit of potassium incorporation.



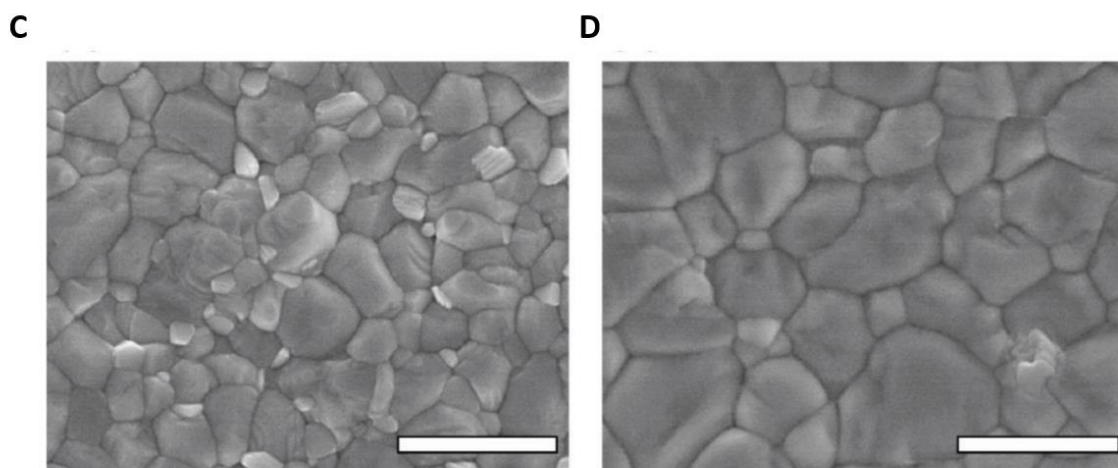


Fig 1 A. XRD data for 5 cation perovskites with different concentrations of KI (1, 2.5, 5, 10 & 20 mol%). The \* denotes the KI peaks and # denotes the  $\delta$ -phase peak. B. Normalized PL and UV-Vis absorption spectroscopy curve for 4 cation FAMACsRb and 5 cation FAMACsRbK films showing a red shift for the 5 cation perovskite with 5 mol% KI incorporation. C. SEM top view of 4 cation FAMACsRb perovskite on meso-TiO<sub>2</sub>. D. SEM top view of 5 cation FAMACsRbK perovskite on meso-TiO<sub>2</sub> showing improved grain size. (scale bar shown is 500 nm)

#### JV data

To verify whether the shift in bandgap translates into the device, we constructed solar cells with the device architecture of FTO/b-SnO<sub>2</sub>/Perovskite/Spiro-OMeTAD/Au. All the above mentioned perovskite compositions were studied to study the KI effect on device performances. All devices were measured using a mask area of 0.16cm<sup>2</sup> at a scan rate of 10mVs<sup>-1</sup> without any preconditioning. For KFAPbI<sub>3</sub>(ii), KRbFARbI<sub>3</sub>(iii), KCsFAPbI<sub>3</sub> (iv), and KRbCsFAPbI<sub>3</sub> (v), the addition of K helped improving the efficiency but the change is not significant. However, for mixed MAFA compositions the effect of K is more evident. We noticed that the hysteresis drops markedly from 2% to almost zero for 5 cation perovskites implying that more complex systems show better performance. This is consistent with previous reports of a reduced hysteresis<sup>78,79</sup> using K. There is a significant improvement in current of about 0.6 mA/cm<sup>2</sup> for 5 cation KRbCsMAFA compared to the best control device with RbCsMAFA system. The improvement in current is also reflected in the IPCE measurements where we can observe atleast 2 % improvement in integrated J<sub>sc</sub> and a clear

red shift of 5nm. This red shift matches with the red shift observed in PL emission measured for 5 cation perovskite.

For 5 cation perovskites, the champion device showed a high efficiencies of 21.7% (for a mesoporous TiO<sub>2</sub> architecture) with a  $V_{oc} = 1.168V$ ,  $J_{sc} = 23.37$ , FF = 79.6% and a hysteresis of 1.4%. For planar SnO<sub>2</sub>, the PCE was 20.8% with a  $V_{oc} = 1.167V$ ,  $J_{sc} = 22.6$ , FF = 78.9% and a negligible hysteresis of 0.1%. The current values are very close to values obtained from IPCE measurements. The maximum power point (MPP) tracking for all the devices was very stable and close to the efficiency of the device measured by scanning the J-V curves.

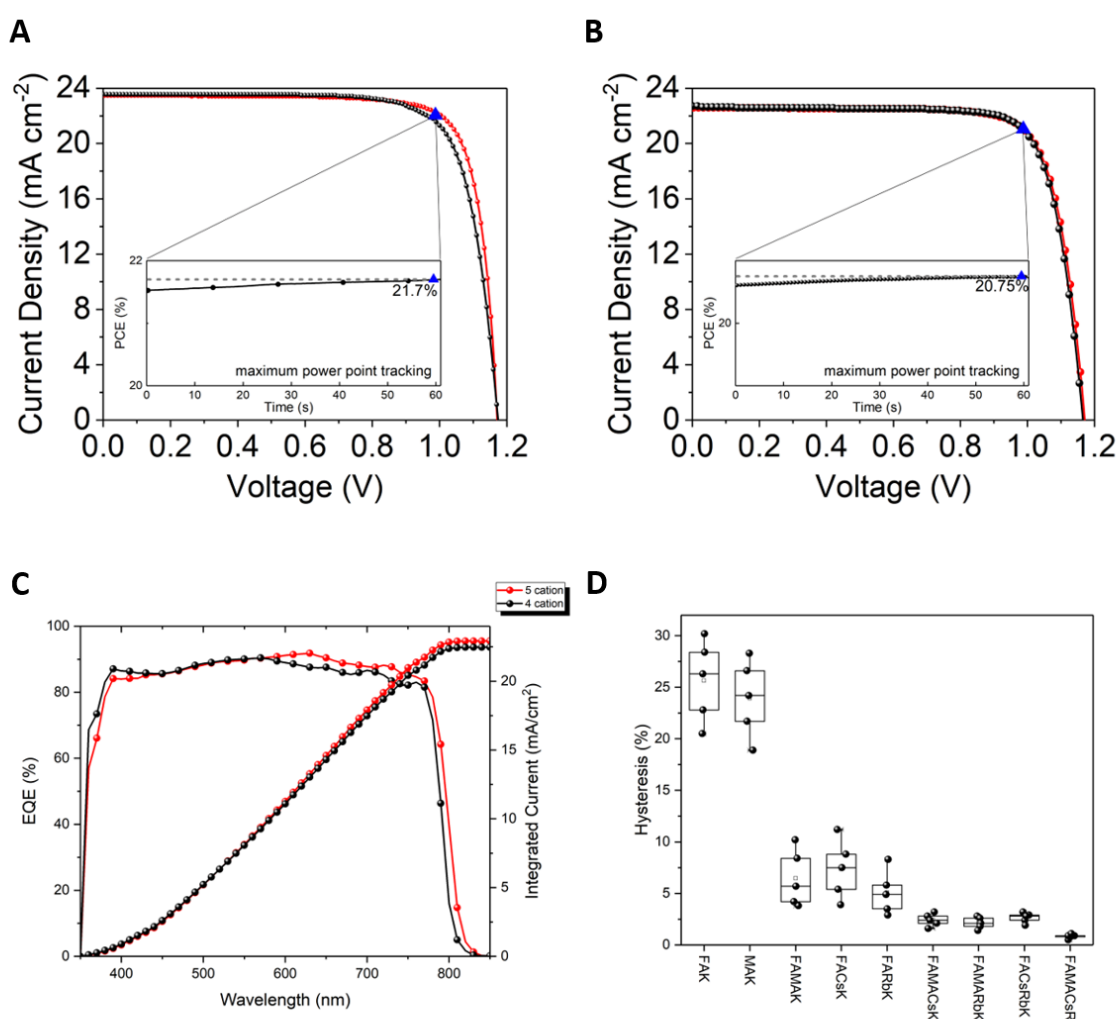


Fig 2 A. JV curve for 5 cation mesoporous champion device with a stabblized MPP of 21.7% efficiency. B. JV curve for 5 cation planar champion device with an MPP of 20.8% efficiency. C. IPCE comparison between 4 and 5 cation perovskite showing a slight red shift (approximately 5 nm) for the onset and higher EQE for 5 cation beyond 580 nm resulting in

higher integrated  $J_{sc}$ . D. Trend of hysteresis for different compositions starting with very high hysteresis for 2 cation FAK perovskite to very low and almost no hysteresis for 5 cation FAMACsRbK perovskite composition.

### Stability

While perovskite solar cells can give high performance, it is well documented that the devices can degrade quickly in air, under light and elevated heat<sup>80,81</sup>. The degradation due to high temperature has been attributed to the gold migration into the HTM where interface passivation can help significantly to improve stability<sup>82</sup>. However, degradation due to moisture and light directly affects the perovskite material<sup>80</sup>. Previous reports show an improved stability upon addition of Cs<sup>33</sup> and Rb<sup>34</sup>. In our work, we show a further improvement in terms of shelf life where the 5 cation devices were found to be more stable than both the standard 3 cation and 4 cation perovskites. In addition, under 1 sun illumination for 500 hours at room temperature, 5 cation perovskites retained higher efficiencies compared to 4 cation (which was previously reported as the most stable composition). In addition, we performed dark recovery tests and found that 5 cation perovskite devices retained over 94% of their initial efficiency whereas the 4 cation retained only close 86%.

Temperature fluctuations can also cause serious degradation.<sup>83</sup> As the devices with K showed higher recovery, we followed up with a temperature cycling test for the 4 and 5 cation devices by cycling the temperature from -10 to 40 °C and then back to -10°C 50 times. The 5 cation devices again showed much better performance retaining over 80% of initial efficiency whereas the 4 cation retained only 60%.



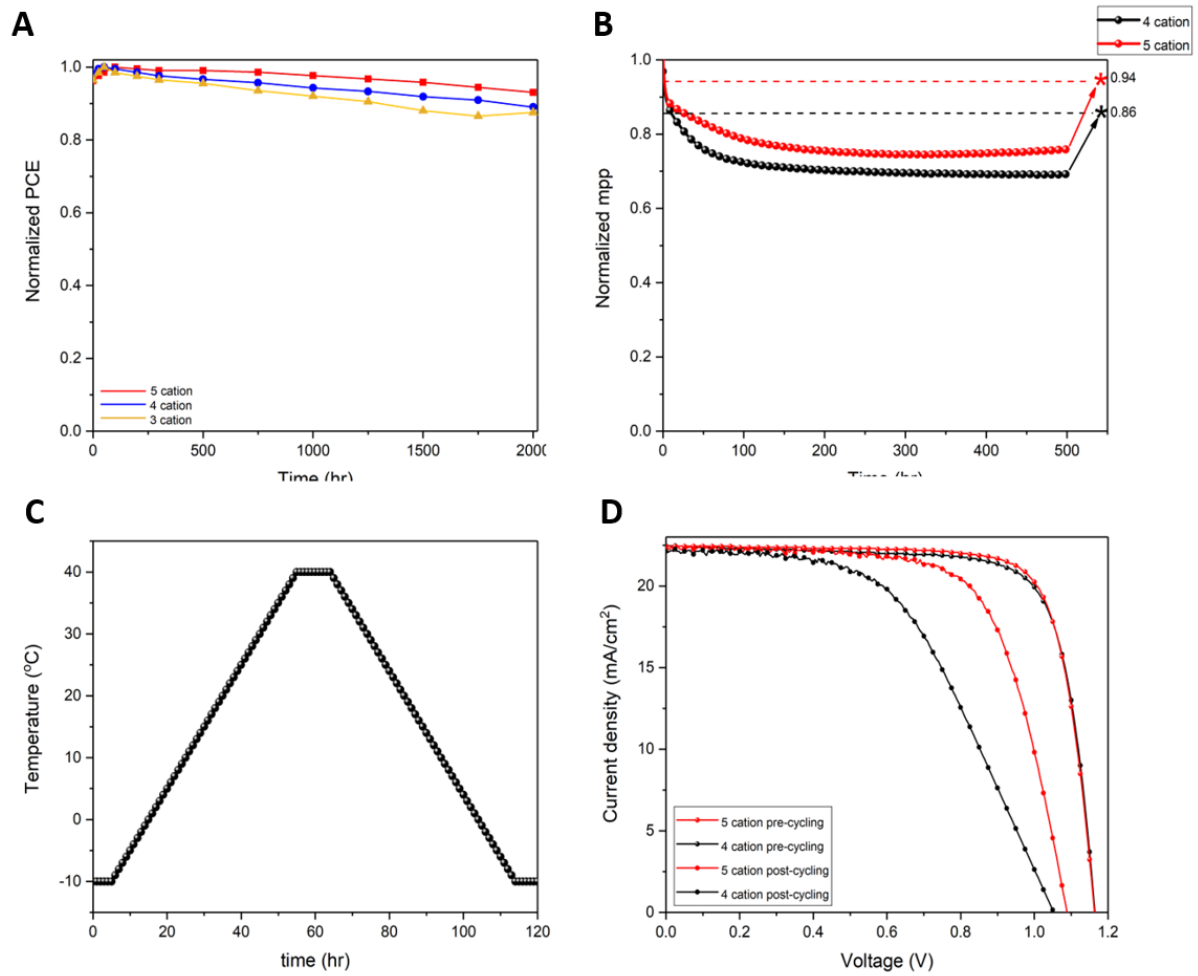


Fig 3 A. Shelf life for 3, 4 and 5 cation devices stored in an environment of 5-10% RH for 2000 hours. B. MPP comparison between 4 and 5 cation perovskite for 500 hours at room temperature under 1 sun illumination showing improved stability and much better recovery (dashed lines) for 5 cation (94%) compared to 4 cation (86%). Both devices used were above 21%. C. Temperature cycling process used for the cycling test ranging from -10 °C to 40 °C with 2 hours operation time for one complete cycle. D. JV performance of 5 and 4 cation devices pre and post cycling test showing 5 cation retains close to 80% of initial efficiency whereas 4 cation retains only 65%.

Table 1: Pre and post cycling JV parameters for 4 and 5 cation perovskite devices

	Voc (V)	Jsc (mA/cm <sup>2</sup> )	FF (%)	Efficiency(%)	Degradation(%)

4 cation pre-cycling	1.163	22.4375	76.4	19.88	<b>34.7</b>
4 cation post-cycling	1.05	22.125	55.55	12.98	
5 cation pre-cycling	1.163	22.4675	77.8	20.34	<b>19.33</b>
5 cation post-cycling	1.085	22.3125	68.01	16.41	

## Conclusion

In this work, we meticulously examined the effect of KI in various perovskite compositions containing FA, MA, Cs and Rb. We show that KI reacts with the Br<sup>-</sup> ion causing the bandgap of the absorber to red shift. This red shift is not seen with compositions not containing any Br<sup>-</sup> ions. This red shifts results in increased J<sub>sc</sub> and hence increased efficiency with minimal hysteresis for perovskite containing all the above-mentioned cations. We also observe an improved stability with higher recovery for perovskite composition containing KI. We were able to demonstrate that addition of KI to the perovskite enhances structural stability as it allows for sustained temperature recycling.

## Supplementary Information

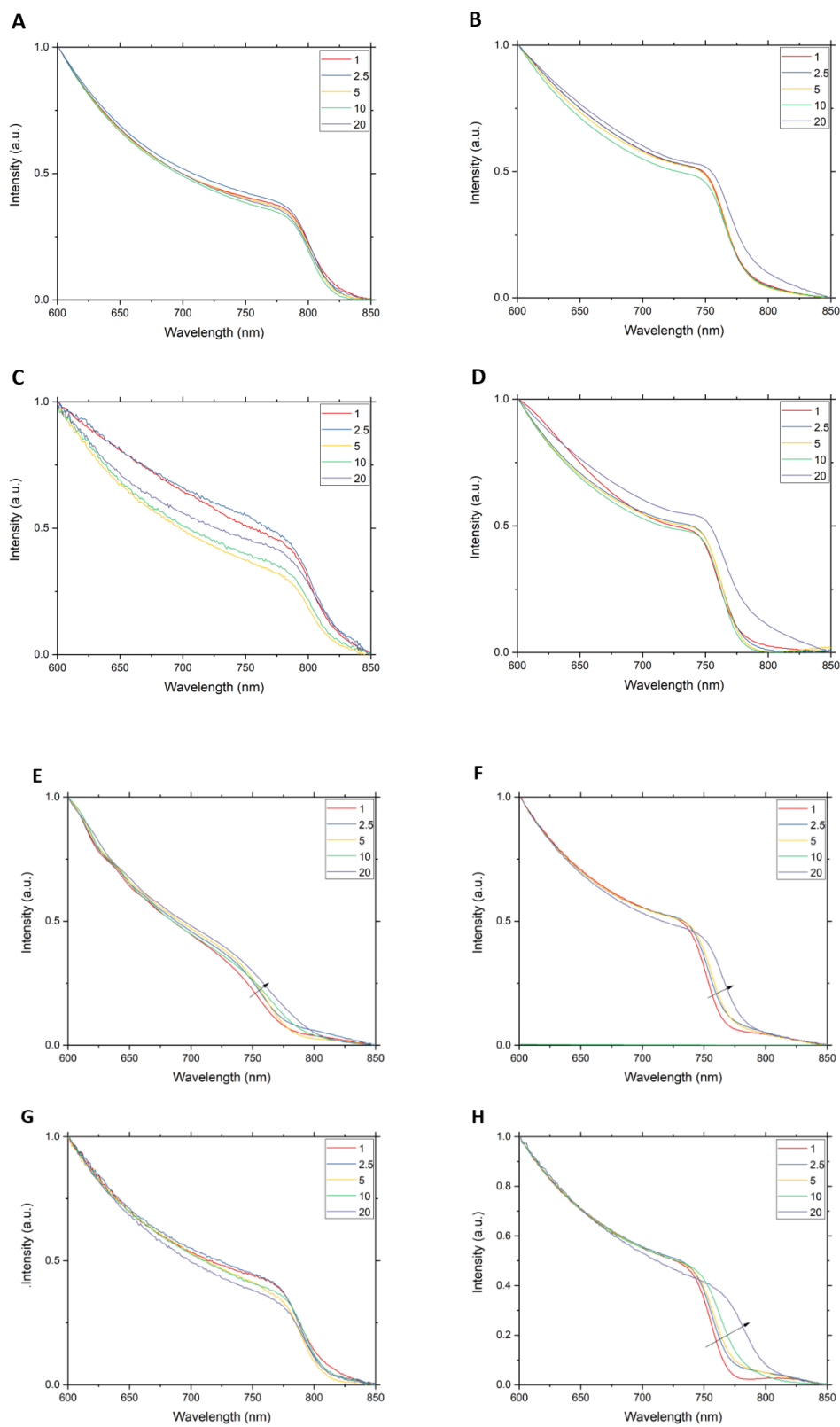


**Fig S1.** UV-Vis spectrum for KI in **A.** FAPbI **B.** MACsPbI **C.** FARbPbI **D.** FACsPbI **E.** FAMAPbIBr **F.** FAMACsPbIBr **G.** FACsRbIBr & **H.** FAMARbPbIBr perovskites

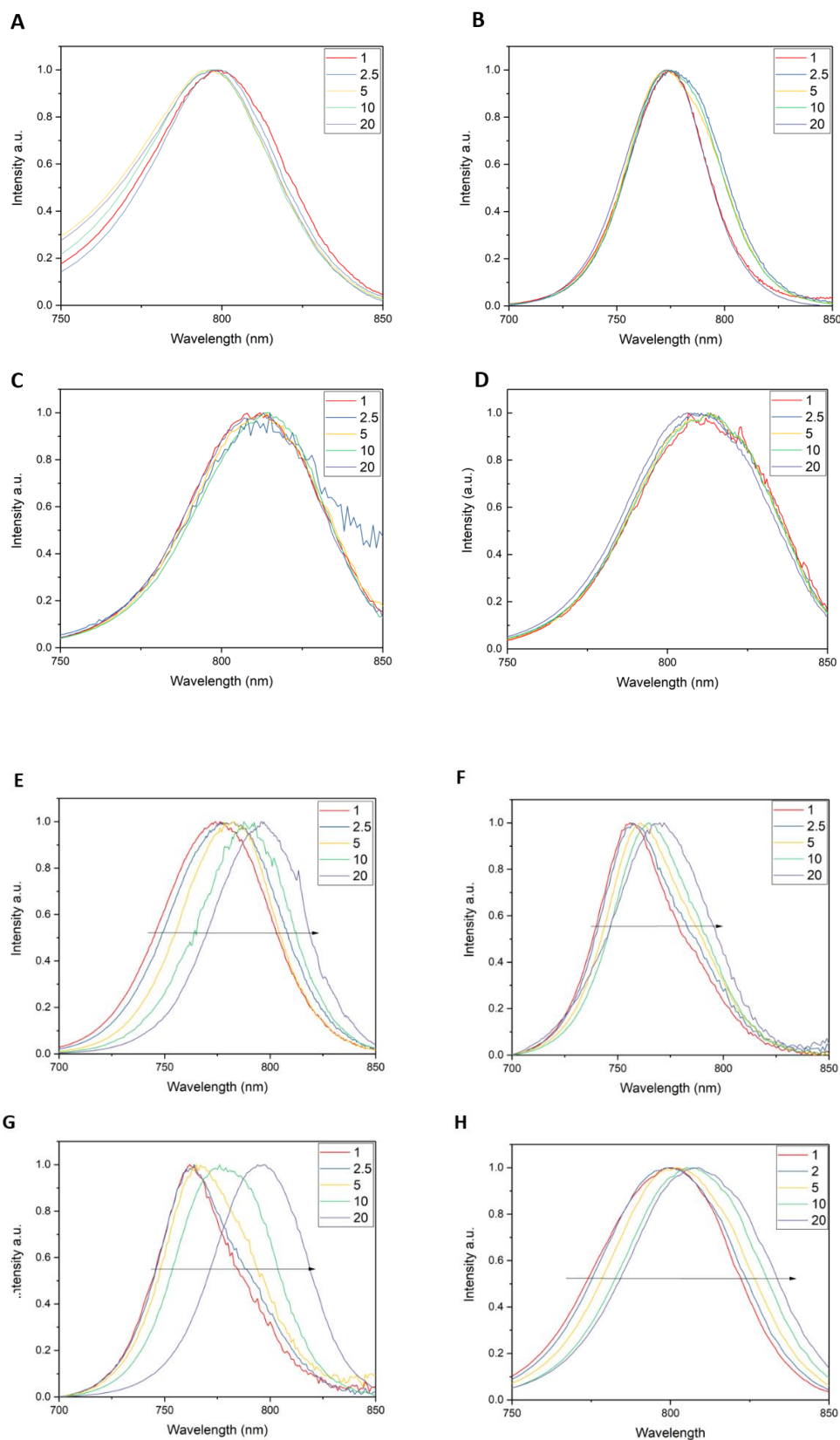


**Fig S2.** PL spectrum for KI in **A.** FAPbI **B.** MACsPbI **C.** FARbPbI **D.** FACsPbI **E.** FAMAPbIBr **F.** FAMACsPbIBr **G.** FACsRbIBr & **H.** FAMARbPbIBr perovskites

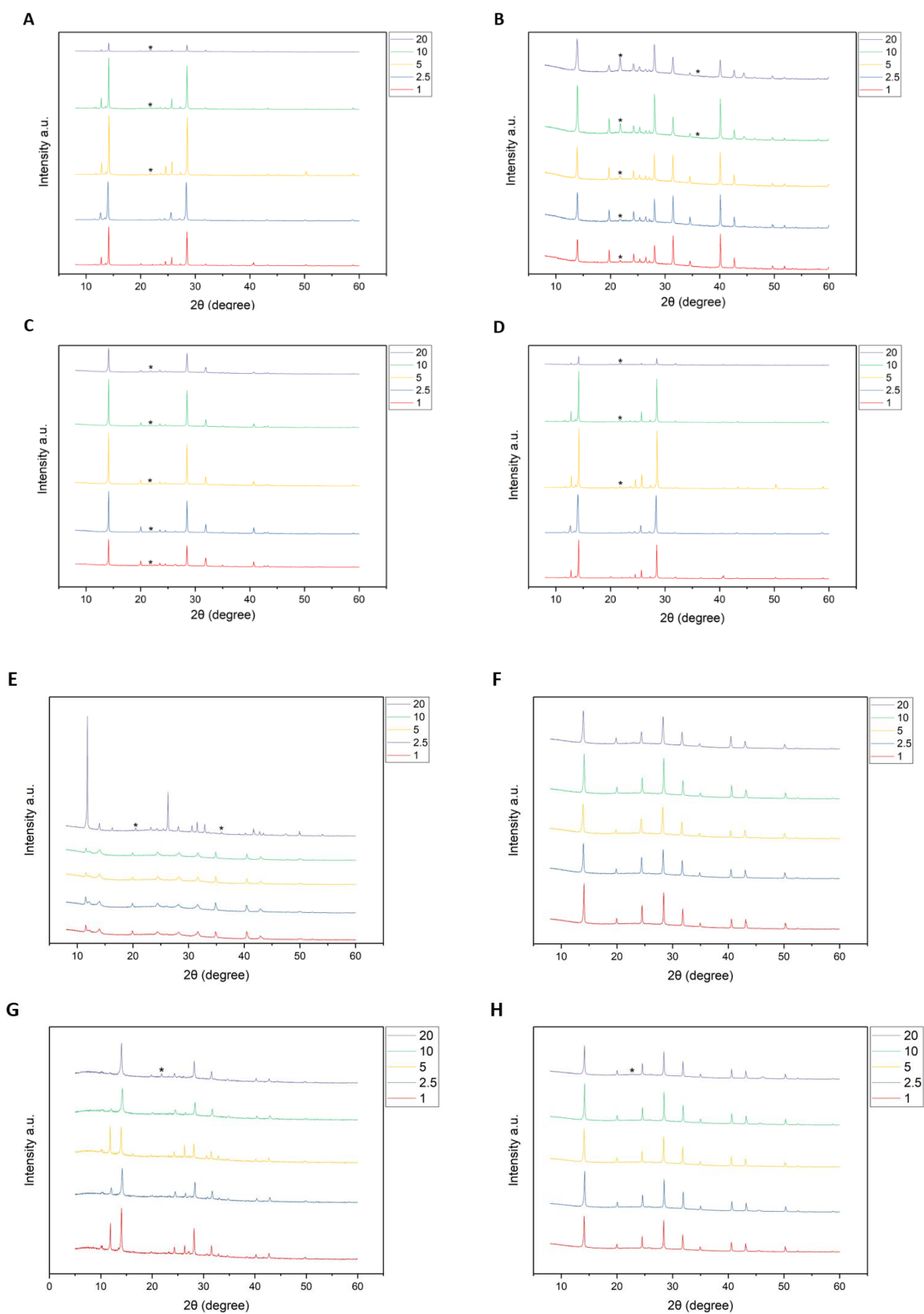


**Fig S3.** XRD plots for KI in **A.** FAPbI **B.** MACsPbI **C.** FARbPbI **D.** FACsPbI **E.** FAMAPbIBr **F.** FAMACsPbIBr **G.** FACsRbIBr & **H.** FAMARbPbIBr perovskites

# Comparing 3,4 and 5 cation perovskite composition JV performance parameters

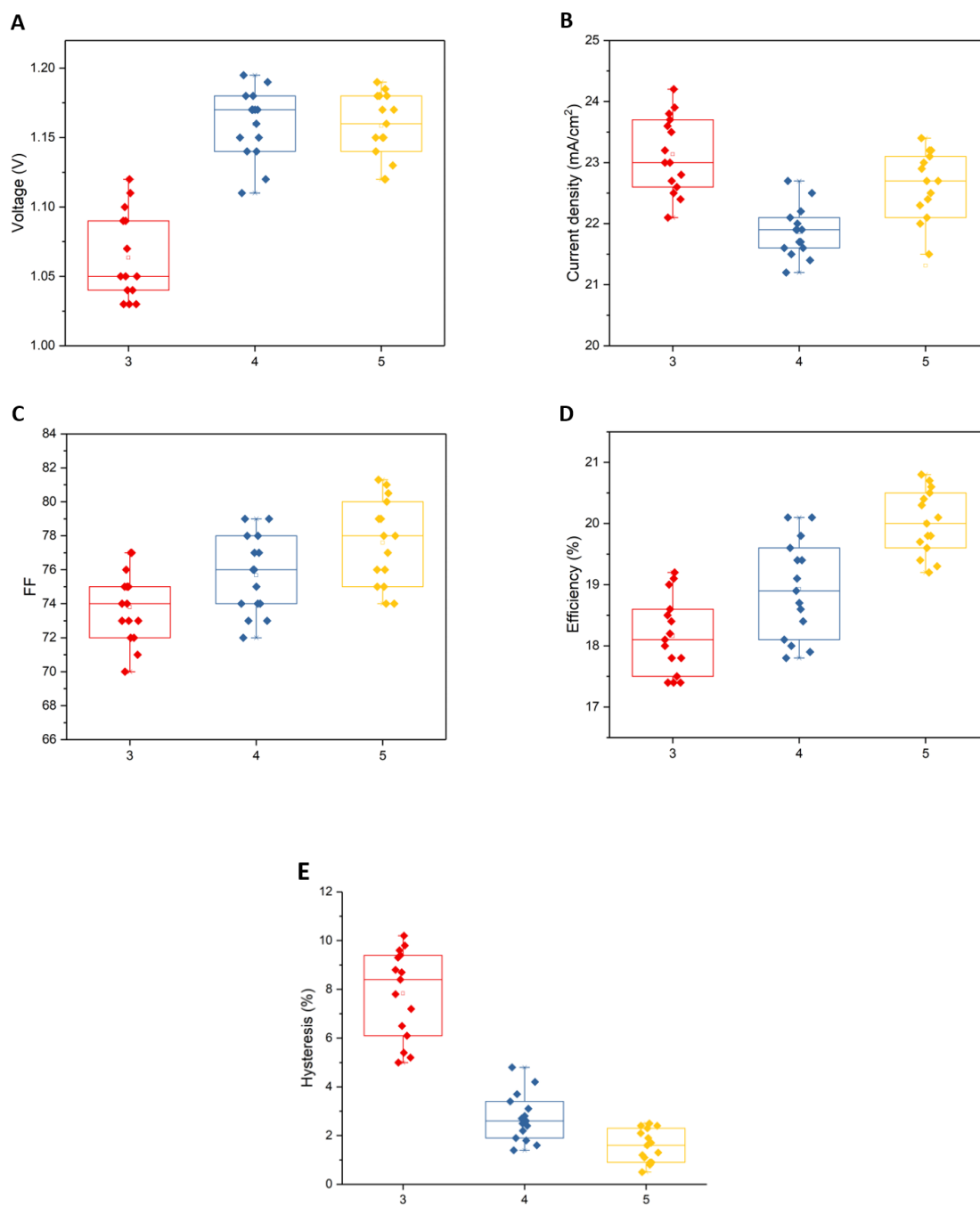


**Fig S4.** Device parameters for 3,4 and 5 cation devices on SnO<sub>2</sub> ETL.

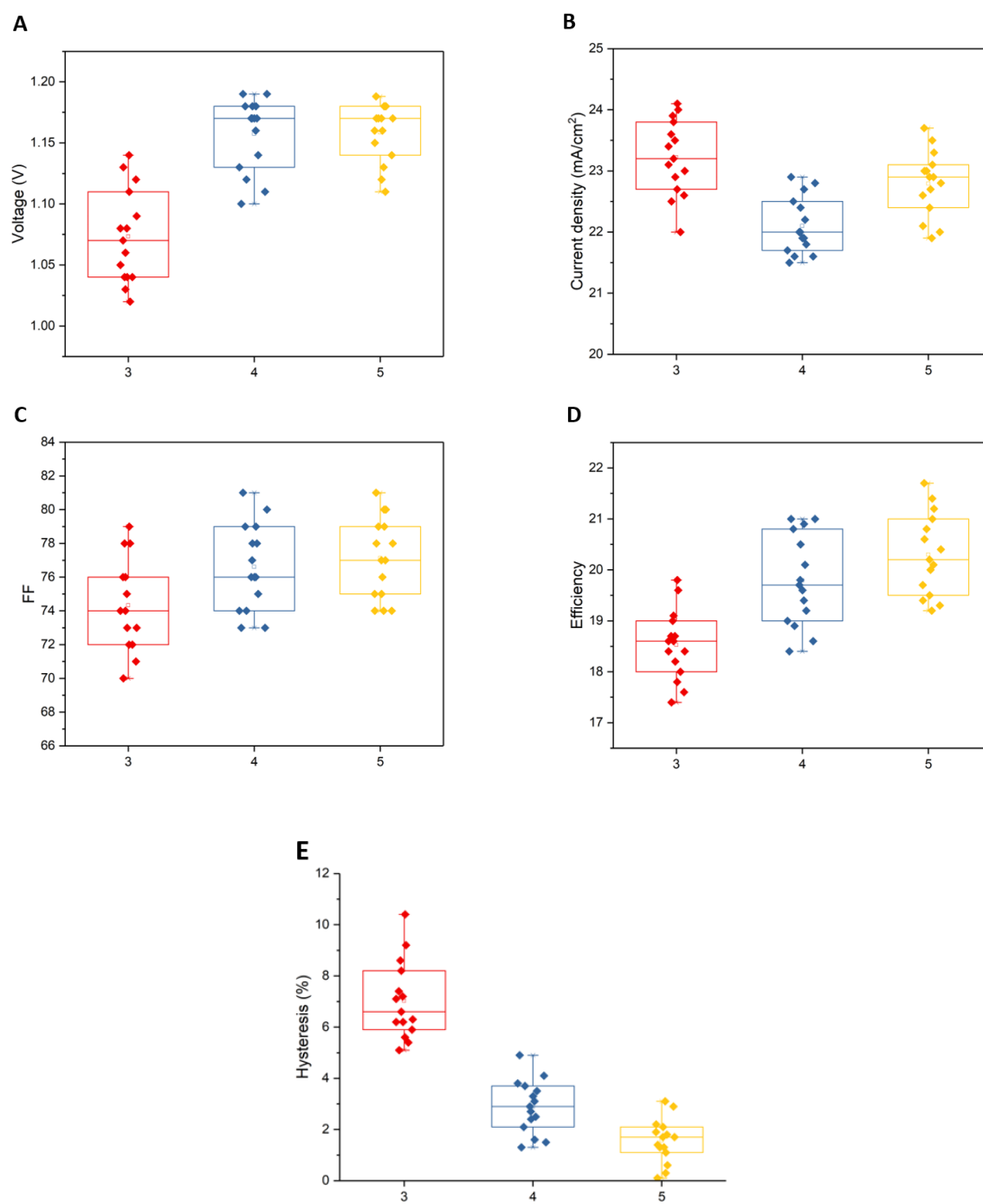


**Fig S5.** Device parameters for 3,4 and 5 cation devices on TiO<sub>2</sub> ETL.

**Table S1.** Efficiency for different concentrations of Cs,Rb and K in 5 cation perovskite (in %)

K	1				3				5			
Cs\Rb	0	1	3	5	0	1	3	5	0	1	3	5
0	16.8	17.4	16.5	16.4	17.2	17.1	17.6	18.1	18.4	17.1	17.7	19.7
1	17.9	16.8	16.7	16.8	17.7	16.2	17.1	19.4	17.8	17.1	18.1	19.8
3	18.4	17.7	19.2	19.6	17.9	17.6	20.6	20.8	18.7	18.2	19.7	19.9
5	18.9	18.8	19.3	20.1	19.2	18.7	19.4	20.7	20.4	20.2	20	20.1

Comparing different perovskite composition JV performance parameters

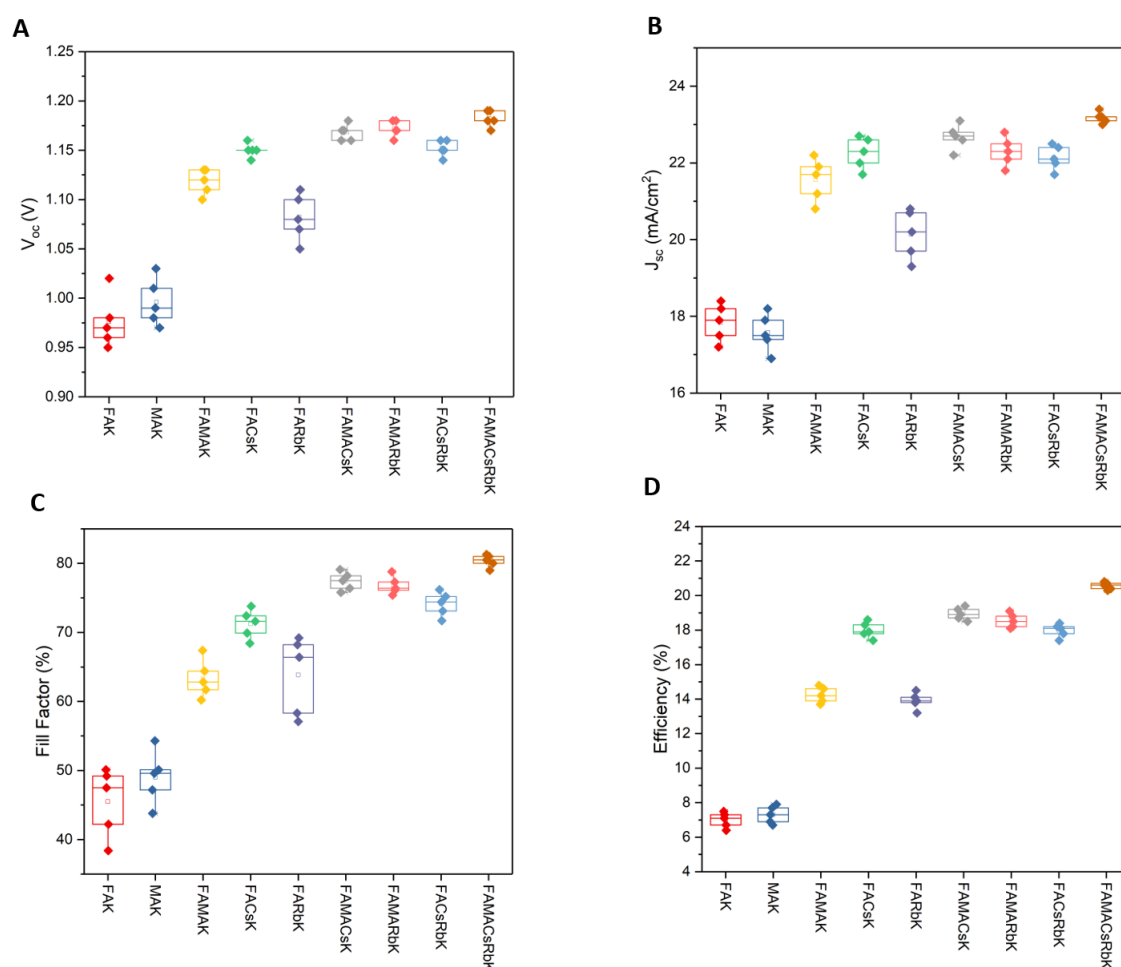




**Fig S6.** Box plot comparing the device parameters for various compositions containing 3% KI.

#### **Perovskite precursor solution**

The perovskite films were deposited using single-step deposition method from the precursor solution. 1.5 M  $\text{PbI}_2$  (TCI) and  $\text{PbBr}_2$  solutions were prepared in a mixture of DMF (99.8%, Acros) and DMSO (99.7%, Acros) in volume ratio 4:1. Then 1.25 mol of FAI and MAI (Dyesol) was added into 1 ml of  $\text{PbI}_2$  and 1.25 mol MABr (Dyesol) was added to 1 ml  $\text{PbBr}_2$  solutions. Thereafter, 1.5M CsI, RbI and KI (ABCR, GmbH, ultra dry; 99.998%) solution was prepared in DMSO. The solutions were added in appropriate ratios to together to obtain the final perovskite solution. The precursor solution was spin-coated onto the mesoporous  $\text{TiO}_2$  films in a two-step programme at 1000 and 4000 r.p.m. for 10 and 25 s, respectively. During the second step, 200  $\mu\text{l}$  of chlorobenzene (99.8%, Acros) was dropped on the spinning substrate 5 s prior to the end of the programme. This was followed by annealing the films at 100 °C for 60 min.

## *Chapter 3: Reduced halide diffusion in triple cation perovskite solar cells for improved charge extraction and operational stability*

(to be submitted, abstract under preparation)

### **Motivation**

Halide ions play a major role in defining the bandgap and optoelectronic properties of metal-halide perovskite semiconductors. Addition of bromide to iodide-based perovskite increases the bandgap which is undesired for attaining the optimum performance in a single-junction solar cell. We show that the increased diffusion of halide vacancies with higher bromide concentration contributes to charge recombination that consequently reduces current density critical to the device performance. We demonstrate that lowering the bromide concentration in the perovskite composition can achieve high efficiencies with greater reproducibility compared to higher bromide concentration. In addition, this performance was accompanied by an improved stability of spiro-OMeTAD hole-transporting-material-based devices, maintaining over 95% of the initial performance for 500 hours at room temperature upon continuous illumination.

### **Introduction**

Solar cells composed of organic-inorganic halide materials have made impressive progress in just a few years with maximum power-conversion efficiency (PCE) evolving from 3.8%<sup>84</sup> in 2009 to a certified 25.5 %<sup>85</sup>. This unprecedented rise in the PCE is largely driven by compositional engineering. Eperon et. al.<sup>17</sup> introduced the formamidinium (FA) to replace the methylammonium ( $\text{CH}_3\text{NH}_3^+$ , MA) cation in 2014, which enabled tuning the band gap from 1.53 eV to 1.48 eV, increasing the theoretical efficiency limit from 31% to 32% (Fig. S1). However, the measured performance of solar cells containing the  $\text{FAPbI}_3$  compositions was lower than for  $\text{MAPbI}_3$ .<sup>18</sup> This is because the black perovskite-type polymorph ( $\alpha$ -phase), which is stable at relatively high temperatures (above 150 °C) turns into the yellow  $\text{FAPbI}_3$  polymorph ( $\delta$ -phase) under ambient conditions.<sup>68</sup> Stability of the  $\alpha$ -phase was improved by employing mixtures of FA and MA. Introducing this approach of mixed cations, Pellet et al.,<sup>86</sup> demonstrated a PCE of 14.9% by substituting MA with FA cations. Despite still showing inferior PCE than the best  $\text{MAPbI}_3$ -based solar cells, these MAFA compositions allowed for

higher photocurrents (19% improvement), confirming the validity of this bandgap-tuning strategy towards higher theoretical efficiencies.

The approach of compositional engineering was further advanced and extended to the halides in 2014 by Jeon et. al.<sup>87</sup> who reported record efficiencies exceeding 18% by introducing 15% MAPbBr<sub>3</sub> in FAPbI<sub>3</sub>. Introducing bromine enabled both phase stabilization and better crystallization which lead to superior solar-cell performances compared to pure iodide perovskite compositions<sup>88</sup>. In 2017, Yang et. al. reported record efficiencies of 22.1%<sup>89</sup> with a lower bandgap two-step deposited perovskite film using only 2.5% bromide. Following this, lowering the bromide content resulted in the higher efficiencies compared to compositions with high bromide concentration. Generally, perovskite top surface passivations and crystalizing agents like MACl are required for optimum efficiencies but even without passivation efficiencies of over 23% was achieved. The highest PCE of 25.2% for perovskite solar cells was achieved by Yoo et.al. by reducing the bromide content to 0.8%.<sup>70</sup>

Substitution of iodide with bromide was believed to improve the quality of the films by assisting the crystallization process, but recent advances in perovskite performance by reducing the bromide content imply that higher bromide concentration affect the device performance adversely. In this work, starting from the optimum triple cation (FA<sub>0.83</sub>MA<sub>0.17</sub>)<sub>0.95</sub>CS<sub>0.05</sub>Pb(I<sub>0.83</sub>Br<sub>0.17</sub>)<sub>3</sub> composition<sup>33</sup> deposited by a single-step anti-solvent method, we systematically reduce the bromide concentrations to 1% to study the effect of higher bromide content. We were able to observe higher device efficiencies and reproducibility without any passivation. A reduced loss-in-potential and a higher external quantum efficiency over the whole wavelength range indicate reduced charge carrier recombination. Furthermore, the long-term operational stability is enhanced, which is related to a reduced concentration of mobile halide defects, as supported by calculated formation and activation energies for halide vacancies.

## Basic characterisation

The effect of varied concentrations of bromide on the perovskite structure was investigated by X-ray diffraction (XRD) measurements on films with the nominal composition (FA<sub>0.83</sub>MA<sub>0.17</sub>)<sub>0.95</sub>CS<sub>0.05</sub>Pb(I<sub>1-x</sub>Br<sub>x</sub>)<sub>3</sub> (x = 1, 5, 10, and 17%). The XRD patterns of fresh samples (**Fig. 2A**) shows identical peaks for perovskite with different compositions while the samples

aged under light for 100 hours (**Fig. 2B**) show the same perovskite peaks but for higher bromide concentrations  $\text{PbBr}_2$  peaks start becoming visible, whereas the fresh samples don't show any  $\text{PbBr}_2$  peaks. There is a slight shift to higher angles as we increase the bromide concentration, which can be clearly seen for the  $2\theta \sim 50^\circ$  peak ascribed to the (013) reflection (**Fig S2**), implying that the lattice parameter associated with the bromide is smaller. This is in accordance with the bromide featuring a smaller radius as compared to iodide. Moreover, the gradual shift in the diffraction angle suggests that the two halides are co-present in the perovskite lattice following the trend of the nominal composition. Bromide has been reported to be necessary for maintaining phase stability of the perovskite structure in MA & FA perovskite,<sup>88,90</sup> but the identical XRD patterns imply that the phase instability associated with lower bromide concentrations is suppressed for triple cation perovskites.

We performed UV-Vis absorption and photoluminescence (PL) measurements to assess the effect of different bromide concentrations on the bandgap. Both UV-Vis absorption and the PL spectra feature a gradual red shift in both the absorption onset (**Fig. 2C**) and the emission peak (**Fig. 2D**) upon reducing the bromide concentrations, which is in accordance with the known effect on the bandgap<sup>18,91</sup> (Fig. S1). From the PL, we can also see that the intensity increases with lower bromide concentrations.

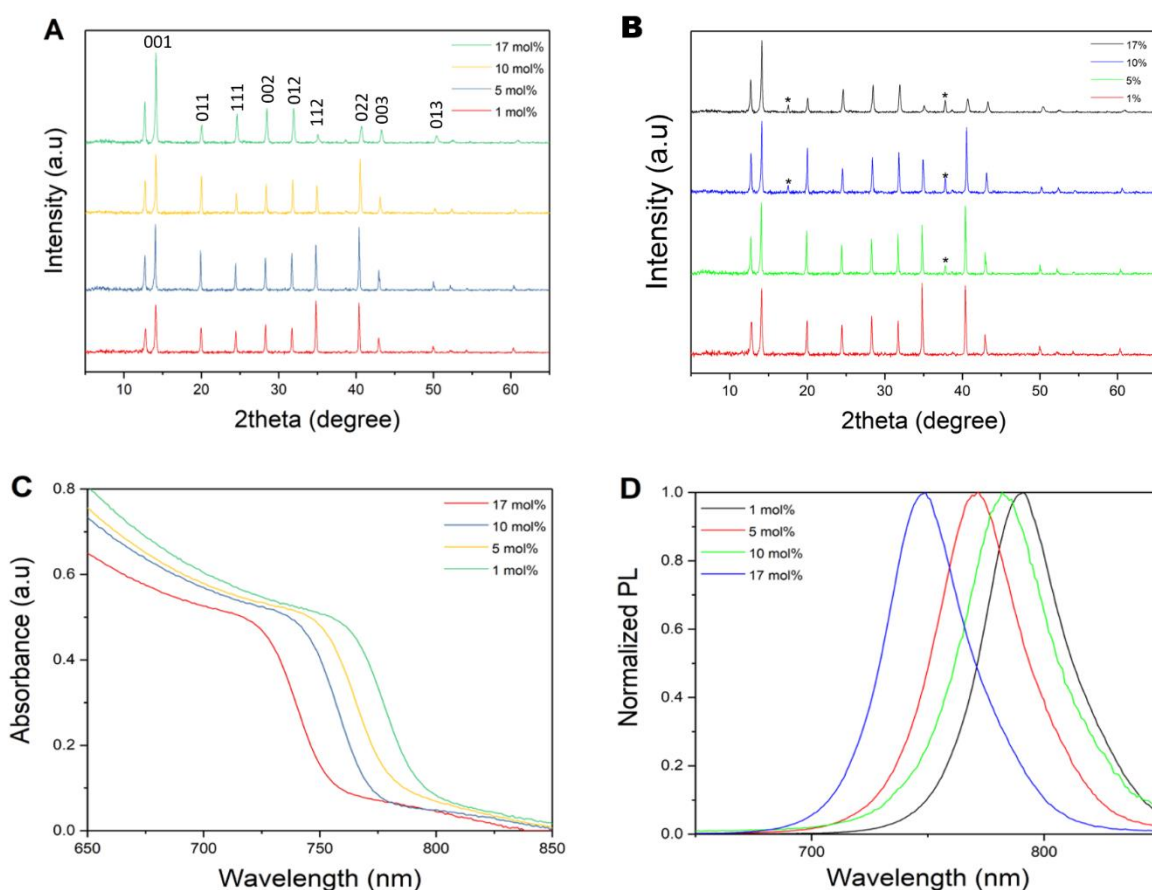


**Fig. 2. Perovskite structure analysis and optical properties depending on the bromide content.** (A) XRD pattern for compositions with different bromide concentrations. \* denotes the PbBr<sub>2</sub> peaks (B) Magnified display of the perovskite peak at  $2\theta = 50^\circ$  showing the shift in the peak position. (C) UV-Vis absorption and (D) PL spectra of different bromide concentrations (1, 5, 10, and 17%) in the perovskite composition.

### Impedance Spectroscopy

To elucidate the influence of the bromide composition on charge transport mechanisms we performed electrochemical impedance spectroscopy (EIS) on the two extreme compositions (i.e. 1% and 17%). The impedance measurements were carried out on completed devices with the conventional FTO/ blocking (b)-TiO<sub>2</sub>/ mesoporous (m)-TiO<sub>2</sub>/ perovskite/ (2,2',7,7'-tetrakis-(*N,N*-di-4-methoxyphenylamino)-9,9'-spirobifluorene) Spiro-OMeTAD/ Au architecture (for more details on the fabrication refer to the supporting information, SI). For the measurements, devices were exposed to forward bias potentials from 0 V to 1.1 V in steps of 0.05 V under light and dark conditions on which a sinusoidal perturbation of 20 mV was superimposed from 500 kHz to 100 mHz (see Fig. S2). The Nyquist plots of typical impedance

data (here at 0.6 V) is shown in Figure 2A and B for 1% Br and 17% Br samples, respectively. The 1% Br device shows the characteristic behavior with two arcs (one open and one closed), which is commonly observed for perovskite solar cells.<sup>64,92</sup> This data can be fit well with an equivalent circuit comprising a resistance  $R_s$  in series with a parallel R-CPE circuit ( $R_{HF}$ ,  $CPE_{HF}$ ; note that CPE denotes a constant phase element), the latter having embedded another R-CPE circuit ( $R_{LF}$ ,  $CPE_{LF}$ ) in series with  $R_{HF}$  (**Fig. 2A**).<sup>93</sup> In this representation,  $R_s$  is associated with resistances from wiring, FTO, and gold contacts,  $R_{HF}$  and  $CPE_{HF}$  describe the high frequency response affiliated with selective contacts to the perovskite absorber, while  $R_{LF}$  and  $CPE_{LF}$  are associated with the recombination resistance and chemical capacitance of the perovskite absorber in the low frequency range, respectively.<sup>64</sup> In contrast, the impedance data for the 17% Br-containing sample exhibits an additional third component which can be accounted for by adding a Warburg diffusion resistance in series to  $R_{HF}$  and parallel to  $CPE_{HF}$  (**Fig. 2B**). This equivalent circuit element is typically used to describe the low frequency ionic diffusion component of the resistance.<sup>92,94</sup> Notably, it appears that the reduction in bromide content can omit the occurrence of a Warburg diffusion component. Moreover, we find that 17% Br devices exhibit a higher value for  $R_{HF}$  than 1% Br devices, as seen by the larger low frequency  $Z'$ -axis intercept of the high frequency arc at short circuit conditions in **Fig. 2C**.  $R_{HF}$  values are extracted from the equivalent circuit fits of light and dark impedance data from 0 - 1.1 V and plotted in **Fig. 2D** and Fig. S3, respectively. It is apparent that the 1% Br devices exhibit significantly reduced  $R_{HF}$  values over the whole voltage range, which is expected to translate to improved charge transport characteristics of selective contacts or their interface with the absorber for our low Br devices. We point out that  $J$ - $V$  analysis in the dark at various scan rates from 10-1000 mV/s (**Fig. S4**) showed pronounced hysteretic behavior for the 17% Br devices, which further corroborates our EIS finding of higher ionic mobility for high Br devices.

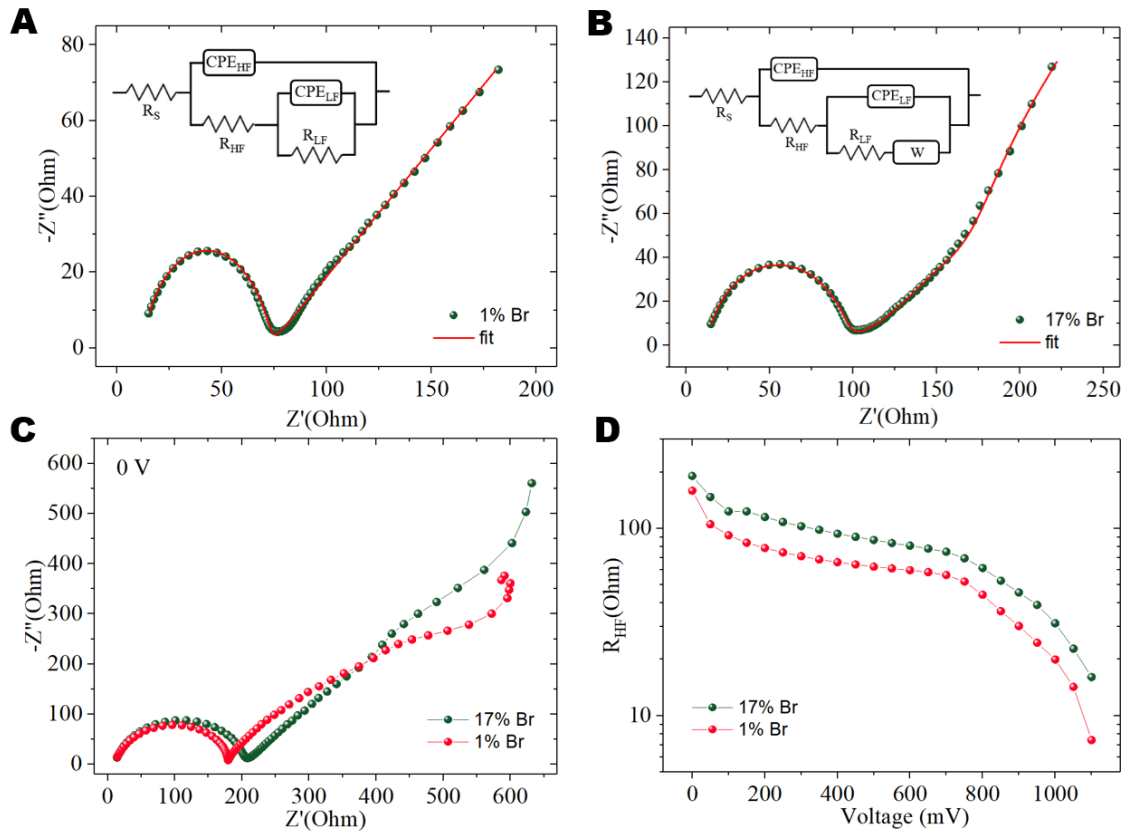


**Fig. 2. Electrical impedance spectroscopy of perovskite devices with different bromide content under light.** EIS data at 600 mV forward bias for (A) 1% Br and (B) 17% Br compositions with corresponding equivalent circuit fits. (C) Representative impedance data at 0V under light (D) Comparison of the high frequency resistance for devices with 17% and 1% Br compositions measured at different voltage bias.

## DFT calculations

To interpret these findings from EIS measurements, we investigated the halide vacancy diffusion in perovskite materials using density functional theory (DFT) calculations (for more details on the methodology refer to the SI). In perovskites, the most mobile species are halide ions, which migrate due to the presence of vacancies in their crystal sublattice.<sup>95</sup> In this regard, halide migration takes place through halide ‘jumping into’ neighboring vacant sites (Fig. S5). Thus, ionic mobility depends on both the concentration of vacancies and on the rate of migration defined by the number of successful migration events per second from the

current site of the anion to a neighboring vacancy site. Accordingly, the higher the vacancy concentration and migration rate, the higher is the mobility. In mixed halide perovskite, iodide and bromide occur on the same sublattice, thus both anions can migrate into either  $I^-$  ( $V_I^\bullet$ ) or  $Br^-$  ( $V_{Br}^\bullet$ ) vacancies. Therefore, in the case of mixed halide perovskites, the total halide diffusion coefficient can be written as [https://www.sciencedirect.com/science/article/pii/B9780125226622500078]

$$D = [V_X^\bullet]l^2(x_{I^-}J^{I^-} + x_{Br^-}J^{Br^-}) \quad (1)$$

Where  $[V_X^\bullet]$  is the fraction of halide vacancy sites, *i.e.* the number of vacant sites over the number of halide, and is the sum of the corresponding iodide  $[V_I^\bullet]$ , and bromide,  $[V_{Br}^\bullet]$ , quantities;  $J^{I^-}$  and  $J^{Br^-}$  are the migration rates of  $I^-$  and  $Br^-$ ;  $x_{I^-}$  and  $x_{Br^-}$  the atomic fractions of iodide and bromide anions in the sample; finally,  $l$  is the length of a migration event, corresponding to the distance between halide sites. In principle,  $FA^+$ ,  $MA^+$ ,  $Cs^+$  and  $Pb^{2+}$  cations also contribute to the total ionic mobility, however previous studies have shown that their migration rates are much lower than those of halides, thus their contribution to the total diffusion coefficient is negligible.<sup>96</sup> We thereby considered three computational samples of  $FAPbI_{3(1-x)}Br_{3x}$  with composition 0, 8.5 and 17 mol% of bromide (**Fig. S6**). We also assessed the effect of cation mixing on the concentration of vacancies and halide migration rates. We observed a reduction of the lattice with increasing bromide content, resulting in a shifting of the simulated XRD peaks at higher angles (**Fig. S7B**), in accordance with the experimental observations. Moreover, following the study of Walsh et al. on vacancies formation in  $MAPbI_3$ ,<sup>97</sup> we found that iodide vacancies are introduced *via* “partial” disorder reactions, leading to the formation of  $PbI_2$  (see SI) and characterized by a formation enthalpy decreasing with Br content (**Table 1** and **Table S2**). The formation of bromide vacancies follows the same mechanism as iodide ones. However, at 8.5 mol% bromide content the formation energy of  $V_{Br}^\bullet$  is as high as 0.47 eV and it gives negligible contribution to the overall vacancies atomic fraction. At 17 mol% bromide content,  $V_{Br}^\bullet$  provides a sizable contribution to the total vacancy fraction *via* both Schottky and partial disorder reactions.

**Table 1. Schottky and partial disorder reactions leading to the formation of halide vacancies with the corresponding formation enthalpy,  $H_f$ , and fraction of halide vacancies,  $[V_X^\bullet]$ .** Only the reactions giving a significant contribution to the concentration of defects are listed here,



a complete list of reactions and associated properties is reported in the Supplementary information (**Table S2**). We remark that the difference of formation energy between 0 and 8.5 mol% samples is within the numerical accuracy of the calculations and lower than the thermal energy at room temperature,  $k_B T$ .

Composition (% Br)	Reaction	$H_f(\text{eV})$	$[V_X^\bullet]$
0 mol%	$nil \rightarrow V_{Pb}'' + 2V_I^\bullet + PbI_2$	0.24	$1.6 \cdot 10^{-4}$
8.5 mol%	$nil \rightarrow V_{Pb}'' + 2V_I^\bullet + PbI_2$	0.23	$1.8 \cdot 10^{-4}$
	$nil \rightarrow V_{Pb}'' + 3V_I^\bullet + V_{FA}' + FAPbI_3$	0.20	$1.2 \cdot 10^{-3}$
	$nil \rightarrow V_{Pb}'' + 2V_I^\bullet + PbI_2$	0.19	$9 \cdot 10^{-4}$
17 mol%	$nil \rightarrow V_{Pb}'' + 2V_{Br}^\bullet + PbBr_2$	0.20	$2 \cdot 10^{-4}$
Total halide vacancies			0.0023

The halide migration rates  $J^{I^-}$  and  $J^{Br^-}$  obey the Arrhenius equation  $J^{X^-} = J_0^{X^-} \exp(-E_M^{X^-}/k_B T)$ ; here,  $E_M^{X^-}$  is the halide migration energy, the barrier that  $X^-$  has to overcome to move into a neighboring vacancy site,  $k_B$  the Boltzmann constant and  $T$  the temperature.  $J_0^{X^-}$  is the number of attempted (but not necessarily successful) migration events per second and it is often approximated by  $J_0^{X^-} = k_B T/\hbar$ . Hence a higher migration energy corresponds a lower migration rate. Using the string method,<sup>98</sup> we computed the migration barrier of  $I^-$  and  $Br^-$ . The migration mechanism of iodide and bromide is very similar and consists in the rotation of the Pb—X bond formed by the migrating halide around the correspond lead ion, with very limited rearrangements of the other atoms and organic cations (**Fig. 4A**). Consistently with our previous results in pure iodide and bromide perovskites,<sup>99</sup>  $Br^-$  has a lower migration barrier than  $I^-$ , resulting in an exponentially higher migration rate of bromide over iodide ions (**Table 2**). Thus, despite the lower concentration of bromide with respect to iodide,  $Br^-$  provides the most significant contribution to the diffusion coefficient (**Fig. 4B**). In addition, cation mixing plays a minor role on the migration mechanism and rate. We observed a minor and consistent reduction of all the barriers by  $\sim 0.02$  eV, i.e. less than the thermal energy at room temperature ( $k_B T \sim 0.026$  eV at  $T = 300$  K). Moreover, when the

MA ion is far from the migrating halide, the energy along the path remains essentially unaltered (**Fig. S8**). When the migration takes place at the crystal lattice containing the MA ion, its high dipole moment alters the relative stability of the initial and final configuration of the migrating halide. Nevertheless, the mean forth and back migration barrier, which is more relevant given the picosecond timescale of MA reorientation, is within 0.02 eV from the one in absence of MA.

In summary, the increase of halide vacancies and of the concentration of the more mobile Br species concur in enhancing the ionic diffusion coefficient in higher bromide concentration samples (**Table 2**).

**Table 2. Migration barrier,  $E_M^{X^-}$ , and rate,  $J^{X^-}$ , of  $I^-$  and  $Br^-$ , together with the contribution of either anion to the migration rate and the overall ionic diffusion coefficient depending on the ion content.**

System	$X^-$	$E_M^{X^-}$ (eV)	$J^{X^-}$ ( $s^{-1}$ )	$x_{X^-} J^{X^-}$ ( $s^{-1}$ )	D ( $cm^2/s$ )
0 mol%	$I^-$	0.49	$3 \cdot 10^4$	$3 \cdot 10^4$	$6 \cdot 10^{-14}$
8.5 mol%	$I^-$	0.53	$6 \cdot 10^4$	$5.6 \cdot 10^4$	$2 \cdot 10^{-13}$
	$Br^-$	0.40	$2 \cdot 10^6$	$1.4 \cdot 10^5$	
17 mol%	$I^-$	0.46	$8 \cdot 10^4$	$5 \cdot 10^4$	$9 \cdot 10^{-11}$
	$Br^-$	0.33	$2 \cdot 10^7$	$3.4 \cdot 10^6$	

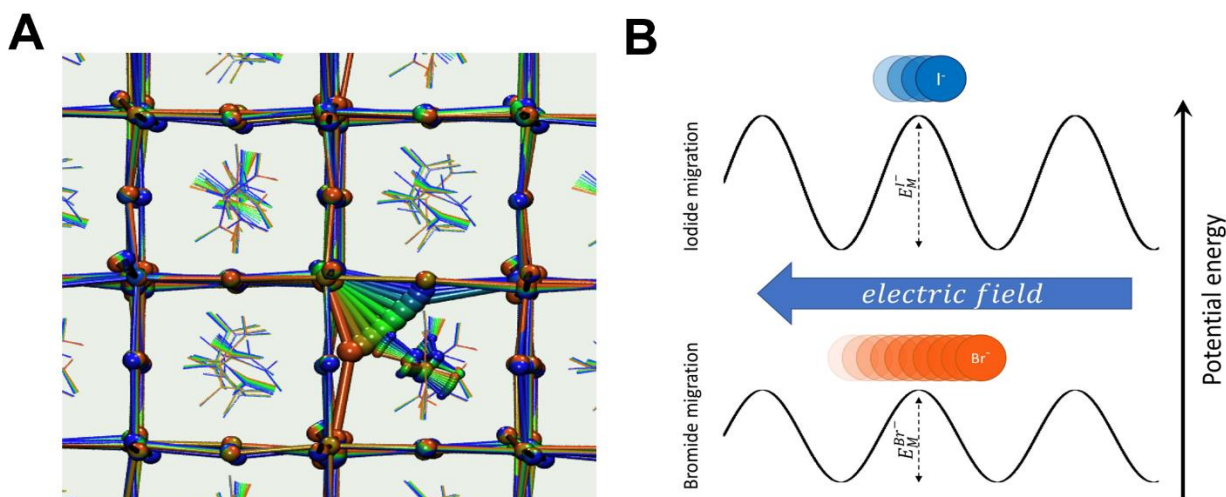


**Figure 4 A. Stroboscopic representation of a halide migration trajectory.** The color palette denotes the progress of the migration, blue is at the beginning, green is the intermediary and red is at the end of the process. Apart the migrating halide and the close  $\text{FA}^+$  all the other cations are essentially unaffected by the migration. **B.** Image potraying the movement of halide ions within the perovskite layer. Enabled by the presence of vacancies in the halide sublattice, the electric field in the solar cell drives the movement of iodide and bromide ions. The lower is the barrier the higher is the diffusion coefficient,  $D$ , the corresponding charge mobility,  $m_q$ , and, hence, the ionic current. (<https://www.sciencedirect.com/science/article/pii/B978012522662250008X>).

## Device performance

We further fabricated solar cells for all the previously analyzed bromide concentrations (i.e. 1, 5, 10, and 17 mol%) with the FTO/b-TiO<sub>2</sub>/m-TiO<sub>2</sub>/perovskite/spiro-OMeTAD/Au device architecture. We observe a clear trend of increase in power conversion efficiency with a reduction in the bromide content, except for 0% (**Fig S9 B**), which was assumed to be in accordance with a significant decrease in the grain size (**Fig S10**). The short-circuit current density ( $J_{\text{sc}}$ ) increased with the reduced bromide content (**Fig. 5A**), which was found to occur not only due to the shift in band gap, but also as a result of an increase in the external quantum efficiency over the whole wavelength range (EQE; **Fig. 5B**). This indicates lower charge recombination in the bulk for lower bromide concentration. Moreover, the loss-in-potential was calculated by subtracting the open circuit voltages,  $V_{\text{oc}}$  (**Fig. S9A**), from the bandgap values divided by elementary charge, which were extracted from Tauc plots

(Fig. S11) by assuming a direct bandgap. It is found that the loss in potential gradually decreases with the decrease of the bromide concentration (Fig. 5C) yielding a value as low as 0.41 V. This number is consistent with data from electroluminescence (EL) measurements (Fig. S12). Both the improvement in  $V_{OC}$  and  $J_{SC}$  led to an enhancement of the average device efficiency for lower bromide concentrations (Fig. 5D). Such optimization of the devices enabled achieving very high and reproducible results with the champion device featuring 22.4% efficiency (Fig. 5E). Moreover, this was accompanied by a high integrated current density values of 25.4 mA/cm<sup>2</sup> based on the incident-photo-to-electron conversion efficiency (IPCE) spectra (Fig. 5F).

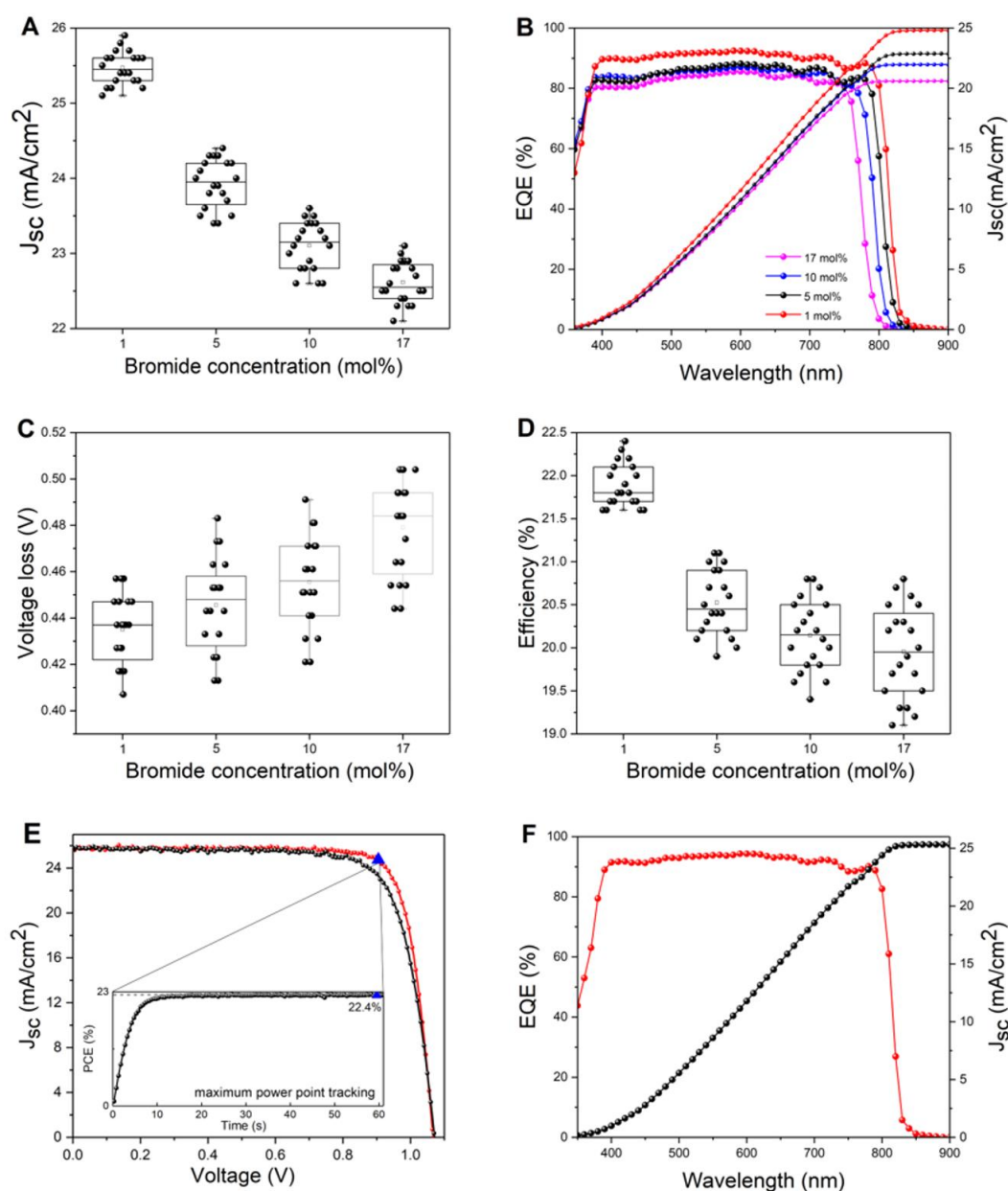


**Fig. 5. Photovoltaic performance of the compositionally engineered perovskite solar cells with different bromide content.** (A) Current density distribution. (B) EQE plot. (C) Loss in potential. (D) Efficiency distribution for different bromide concentrations. (E) *J-V* curve for the champion device with MPP at 22.4%. (F) IPCE spectra of the champion device showing record value for integrated current at 25.4 mA/cm<sup>2</sup>, confirming the values obtained from the *J-V* curves measured under the solar simulator.

## Stability

While perovskite solar cells feature high efficiency, it is well documented that the devices degrade very fast under ambient air conditions, with light, and upon exposure to higher temperatures.<sup>80,81</sup> One degradation pathway under elevated temperature has been attributed to migration of gold from the electrode into the hole-transporting material, where interface passivation can assist in significantly improving the stability.<sup>82</sup> On the contrary, the degradation due to moisture and light has been directly attributed to the instability of the perovskite layer. Typically, the PCE of a PSC with spiro-OMETAD as HTM undergoes an initial exponential decay followed by a linear decay, which has been attributed to increased halide migration during the first few hours of device operation. In this regard, changing the composition can affect the operational stability of the perovskite devices. As DFT calculations indicate that halide diffusion is reduced for lower bromide content devices, we scrutinized the effect of reduced bromide concentration on the stability of the perovskite devices. The devices containing lower bromide content showed much better stability with negligible exponential losses for 1% Br devices (Fig. 6A). The most stable 1% Br device showed remarkable stability by maintaining over 95% of the initial performance at room temperature (Fig. 6B) upon continuous illumination at 1 sun intensity for 500 hours under inert conditions. This improved stability can be attributed to decreased defect concentration in lower bromide perovskite. For spiro-OMeTAD-based devices, such high stability has not been reported previously, which highlights that the lower bromide content composition should be utilized and further improved upon.

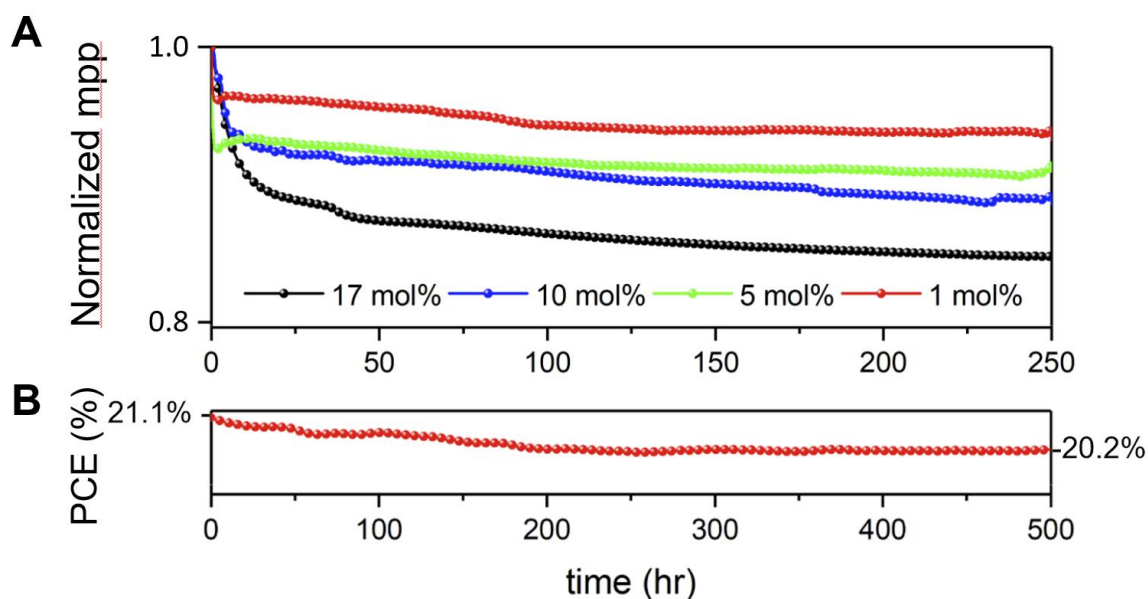


**Fig. 6. Stability of the compositionally engineered perovskite solar cells.** (A) Evaluation of Normalized PCE based on maximum power point tracking (mpp) over time for different bromide concentrations revealing an increase in stability with reduced bromide content. (B) Champion device stability with 1 mol% bromide content for 500 hours at room temperature under continuous 1 sun illumination under inert ( $N_2$ ) conditions.

## Conclusion

DFT calculations show that increased bromide content in mixed halide perovskites generates higher halide vacancy diffusion due to lower activation energies of bromide vacancies. The increased vacancies create trap states at the interface leading to a decrease in the charge extraction capacity of the device, and hence negatively affects the efficiency. This increase in halide defects also causes a significant decrease in the device stability. Reducing the bromide content not only increases the current density but also decreases the voltage recombination due to lower trap states at the interface while also improving the FF.

## Supplementary Information

### Perovskite precursor solution

The perovskite films were deposited using single-step deposition method from the precursor solution. 1.5 M  $PbI_2$  (TCI) and  $PbBr_2$  solutions were prepared in a mixture of DMF (99.8%, Acros) and DMSO (99.7%, Acros) in volume ratio 4:1. Then 1.25 mol of FAI and MAI (Dyesol) was added into 1 ml of  $PbI_2$  and 1.25 mol MABr (Dyesol) was added to 1 ml  $PbBr_2$  solutions.

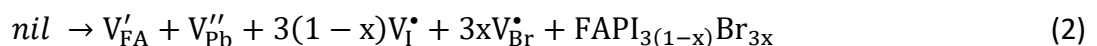
Thereafter, 1.5M CsI (ABCR, GmbH, ultra dry; 99.998%) solution was prepared in DMSO. The four solutions were added in appropriate ratios to obtain  $(\text{FA}_{0.83}\text{MA}_{0.17})_{0.95}\text{Cs}_{0.05}\text{Pb}(\text{I}_x\text{Br}_{1-x})_3$ . The precursor solution was spin-coated onto the mesoporous  $\text{TiO}_2$  films in a two-step programme at 1000 and 4000 r.p.m. for 10 and 25 s, respectively. During the second step, 200  $\mu\text{l}$  of chlorobenzene (99.8%, Acros) was dropped on the spinning substrate 5 s prior to the end of the programme. This was followed by annealing the films at 100 °C for 60 min.

### Density Functional Theory

Density functional theory (DFT) calculations were performed using the Quantum Espresso suite of codes.<sup>100</sup> We used the Perdew–Burke–Ernzerhof (PBE) formulation of the Generalized Gradient Approximation to density functional theory together with ultrasoft pseudopotentials to model the interaction between valence electrons and core electrons and nuclei. Kohn–Sham orbitals were expanded in a plane wave basis set with a kinetic energy cutoff of 40 Ry, and a cutoff of 280 Ry on the expansion of the electronic density. The Brillouin zone was sampled with a 4x4x4 Monkhorst–Pack k-points grid<sup>101</sup>. We remark that the present setup has been extensively used by the authors and other computational groups to determine the structure and energetics of halide perovskite, including systems containing defects<sup>99,102–105</sup>. This setup has proven to give well converged values of the total energy, defect energies, band gap, band energies and atomic forces.

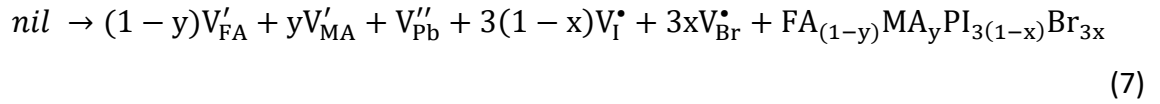
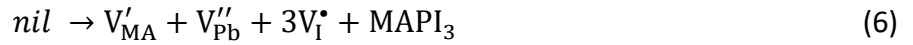
Consistently with a previous work<sup>103</sup>, initial samples were created starting from the experimental structure of  $\text{FAPbI}_3$  containing 12 stoichiometric units. The orientation of  $\text{FA}^+$  cations was randomized, and the structure was fully relaxed, including the cell parameters. Mixed halide systems were obtained by randomly replacing a suitable number of I with Br. The obtained structures were further relaxed.

Defects calculations were performed following Walsh et al.<sup>97</sup> extending their list of possible “full” Schottky and “partial” disorder reactions to include bromide compounds:





We considered also the effect of mixing cations by replacing one FA with one MA and computing the formation energies of defects by Schottky and “partial” disorder reactions when removing halides and the other ions both near or far from the MA. For FA-MA perovskites the above set of reactions was extended to include



Our results show that MA has little effect on vacancy concentration (see **Table S2**).

Samples containing defects were obtained by removing the corresponding ion from the reference bulk structure and relaxing the atomic configuration. Spurious interactions between periodic images of charged defects were considered following the approach introduced by Freysoldt, Neugebauer and Van de Walle<sup>106</sup> using the software SXDEFECTALIGN. Since the local environment of the atoms changes from site to site due to the presence of two different halide species and the orientation of  $FA^+$ , the formation energy might change depending on the ion that is extracted from the structure to produce the defect. To address this problem, we computed the formation energy for all the 36 halide anions and 12 lead and organic cations composing the system. This allowed us to compute the minimum and average formation energy of each defect, and the associated standard deviation, which represent the typical accuracy of our calculations. Data is summarized in **Table S2**.

To compute the vacancy migration paths and energies we employed the (simplified and improved) string method<sup>98</sup>, which we already used previously.<sup>99</sup> The objective of the string method is to identify the most probable path connecting reactants and products. In the present case, reactants and products are two configurations of the system with  $V_X^\bullet$  in two



neighboring sites. The string path is a parametric curve,  $\mathbf{r}(\lambda)$ , in the space of the atomic configurations ( $\mathbf{r}$  is the 3N vector of the atomic positions).  $\lambda$  is a parameter measuring the degree of progress of the vacancy migration:  $\lambda = 0$  when the vacancy is in the initial site, and  $\lambda = 1$  when it is in the final site. It can be shown that the most probable path is the one with zero component of the atomic forces in the direction orthogonal to the path,  $[-\nabla V(\mathbf{r}(\lambda))]_{\perp \mathbf{r}(\lambda)} = 0$ .<sup>98</sup> The continuous path  $\mathbf{r}(\lambda)$  is discretized into a finite number,  $L$ , of configurations (snapshots),  $\{\mathbf{r}(\lambda_i)\}_{i=1,L}$ . These snapshots must satisfy the additional constraint to be at a constant distance from each other:  $|\mathbf{r}(\lambda_i) - \mathbf{r}(\lambda_{i+1})| = |\mathbf{r}(\lambda_j) - \mathbf{r}(\lambda_{j+1})|$ . An initial guess path can be optimized evolving it by a fictitious first-order dynamic (steepest descent “dynamics”) in which at each time step each snapshot,  $\mathbf{r}(\lambda_i)$ , is evolved following the component of the atomic forces orthogonal to the path. Indeed, in the improved string method atoms are evolved according to the complete force and the effect of its tangential component is removed after each string iteration by re-establishing the equidistance condition between snapshots by moving the corresponding configuration along the 3N polygonal passing by all the snapshots that is used as an approximation of the string passing.

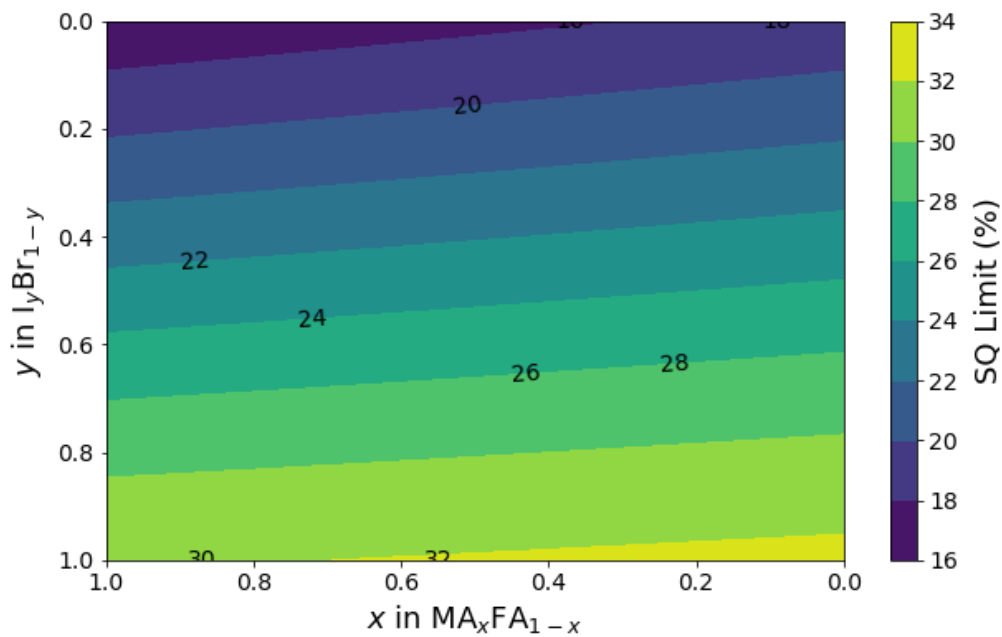


**Fig. S1.** Shockley-Queisser (SQ) limit of the power conversion efficiency (%) for different perovskite compositions based on different ratios of MA ( $x$ ) and FA ( $1-x$ ) based on different ratios of I ( $y$ ) and Br ( $1-y$ ). The values for the bandgaps of the compositions were linearly interpolated between reported values of the extrema.<sup>107</sup>

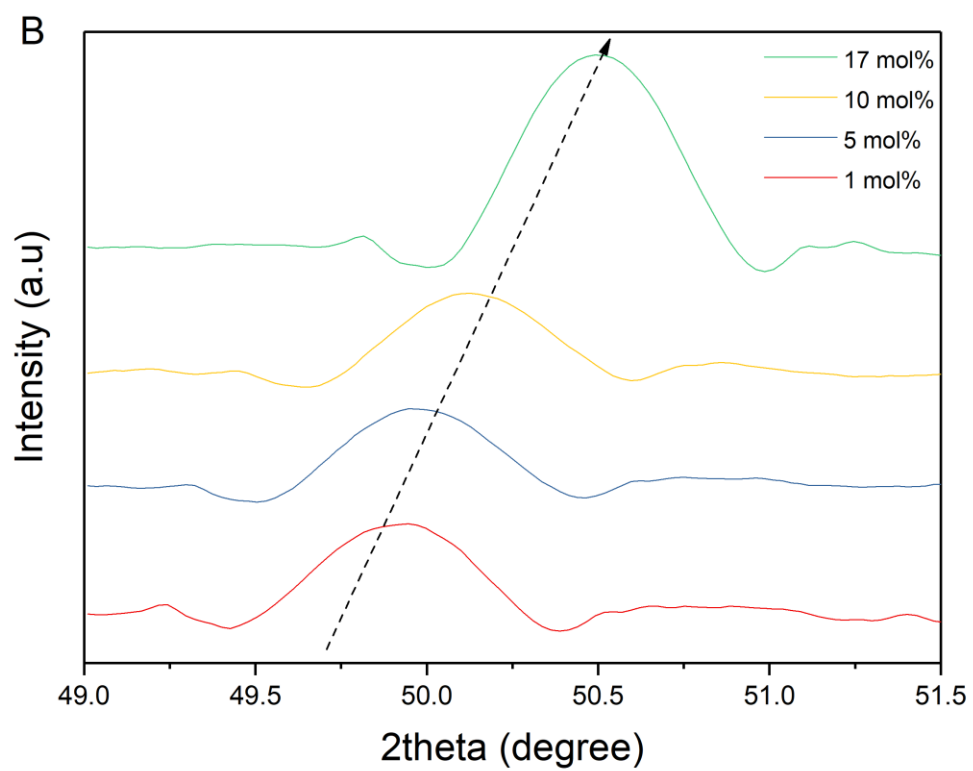


**Fig S2.** XRD image of different bromide concentrations showing a slight shift to higher 2theta for higher bromide

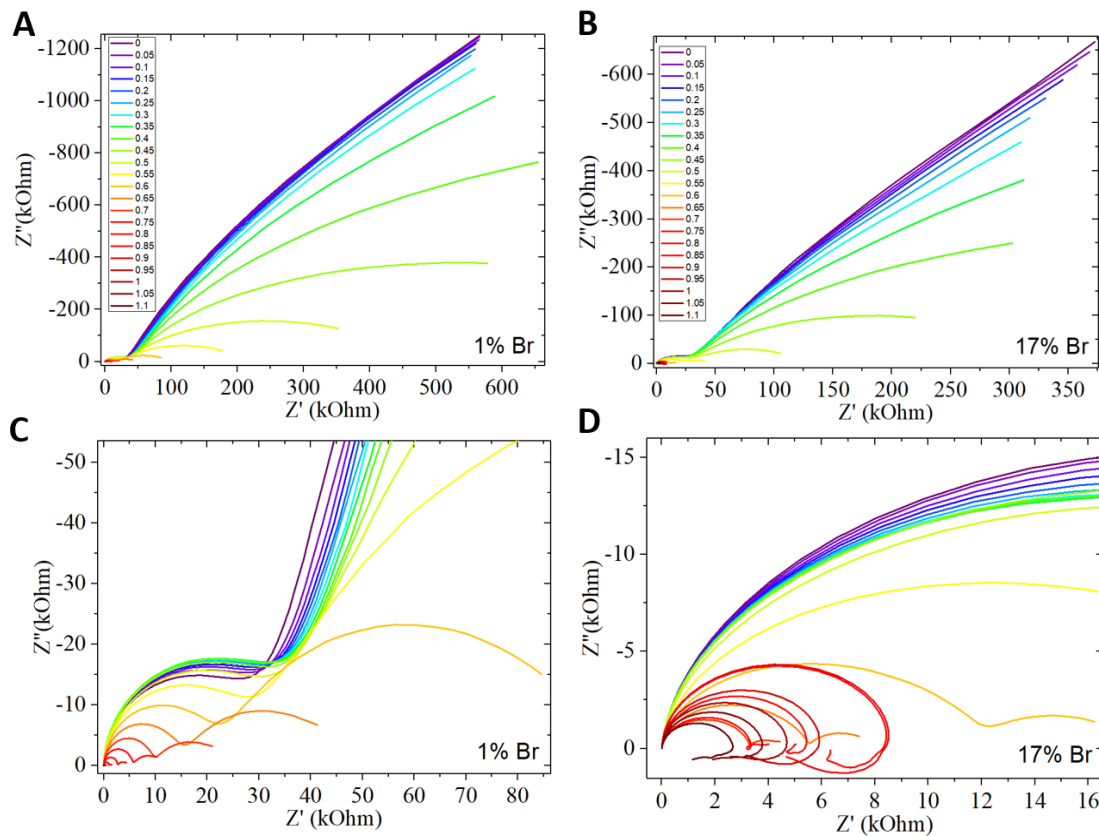


**Fig. S3.** Electrochemical impedance analysis of solar cell with (A, C) 1% Br content and (B, D) 17% Br content in the dark. Figure indices denote the applied voltage in V during the measurement.

**Table S1.** Device data pre and post EIS measurements showing the change in the PV parameters.

Composition	$V_{OC}$ (V)	FF (%)	$J_{SC}$ (mA/cm <sup>2</sup> )	PCE (%)	$R_s$ (Ohm cm <sup>2</sup> )
17% Br	1.074	70.8	23.38	17.88	2.81
1% Br	1.03	74.4	24.65	18.83	1.52
17% Br-EIS	1.018	62.3	22.74	14.98	6.87
1% Br-EIS	1.04	73.5	23.51	18.67	2.09
rel. change (%) 17%	-5.21	-12.01	-2.74	<b>-16.22</b>	<b>144.50</b>
rel. change (%) 1%	0.97	-1.21	<b>-4.62</b>	-0.85	37.87

$V_{OC}$  = open circuit voltage;  $J_{SC}$  = short circuit current density;  $R_s$  = series resistance; FF = fill factor; PCE = solar-to-electric power conversion efficiency.

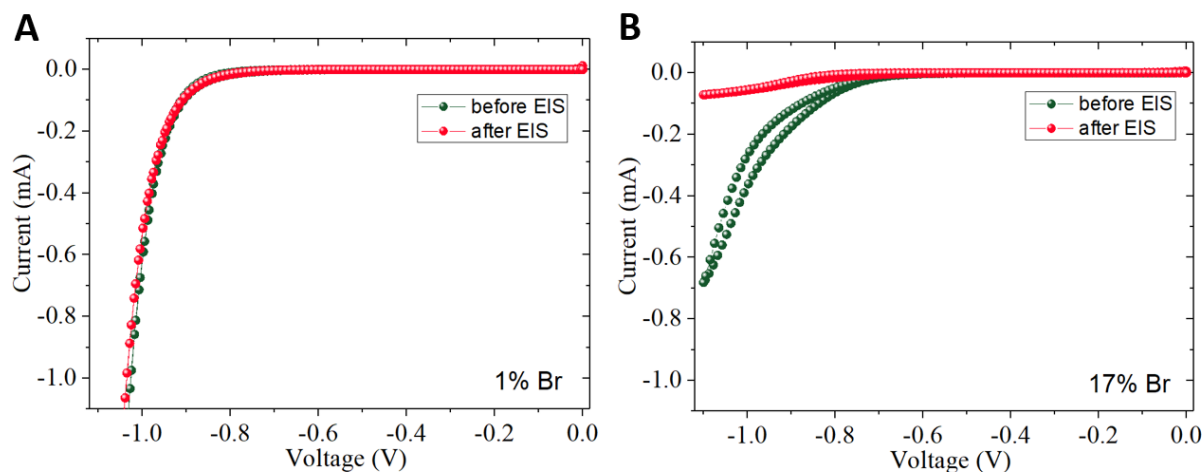


**Fig. S4.** Dark current-voltage characteristics of devices with (A) 1% and (B) 17% bromide content before and immediately after the EIS analysis. The scan speed was 20 mV/s.

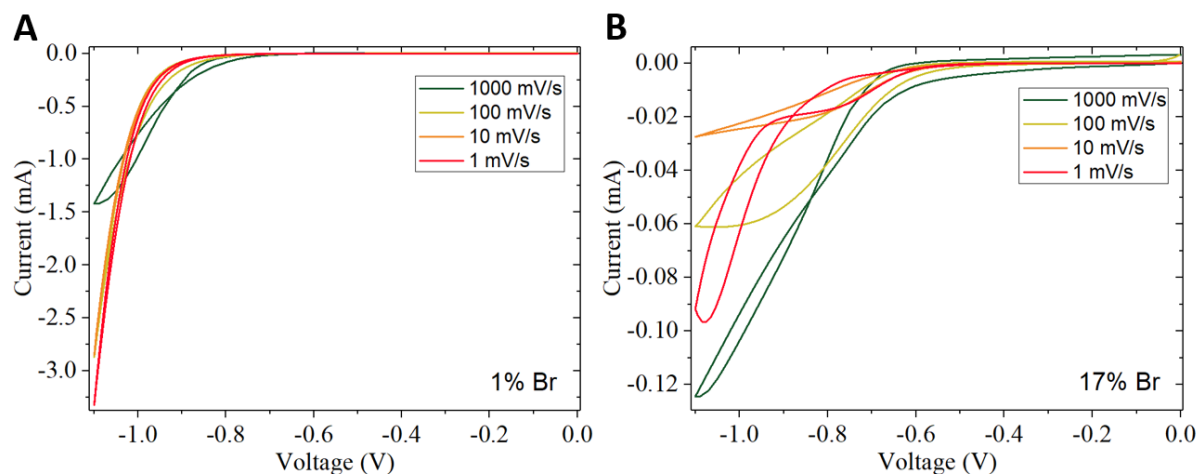


**Fig. S5.** Dark current voltage characteristics of devices with (A) 1% and (B) 17% Br content immediately after EIS analysis with varying scan speeds from 1 mV/s to 1000 mV/s. Note that hysteretic effects for the 1% Br device at highest scan speeds of 1000 mV/s are expected to reflect capacitive effects in the device.

**Table S2.** Schottky and partial disorder reactions leading to the formation of halide vacancies with the corresponding formation enthalpy,  $H_f$ , its average value computed over all sites of the same kind,  $\bar{H}_f$ , and total atomic fraction halide vacancies,  $[V_x^\bullet]$ . The standard deviation of  $H_f$  is  $\sim 0.05$  eV (i.e. twice the thermal energy at room temperature), suggesting that the effect of halide composition on  $\bar{H}_f$  of the most relevant reactions, those producing most of the vacancy defects, is within the computational accuracy.

Composition	Reaction	$H_f(\text{eV})$	$\bar{H}_f(\text{eV})$	$[V_x^\bullet]$
FA (% Br)				
0 mol%	$\text{nil} \rightarrow V''_{\text{Pb}} + 3V_I^\bullet + V'_{\text{FA}} + \text{FAPbI}_3$	0.34	0.85	$2 \cdot 10^{-9}$
	$\text{nil} \rightarrow V_I^\bullet + V'_{\text{FA}} + \text{FAI}$	0.43	0.61	$6 \cdot 10^{-8}$
	$\text{nil} \rightarrow V''_{\text{Pb}} + 2V_I^\bullet + \text{PbI}_2$	0.24	0.34	$1.6 \cdot 10^{-4}$
8 mol%	$\text{nil} \rightarrow V''_{\text{Pb}} + (3-x)V_I^\bullet + xV_{\text{Br}}^\bullet + V'_{\text{FA}} + \text{FAPbI}_{3(1-x)}\text{Br}_{3x}$	0.36	0.90	$2 \cdot 10^{-6}$
	$\text{nil} \rightarrow V''_{\text{Pb}} + 3V_I^\bullet + V'_{\text{FA}} + \text{FAPbI}_3$	0.34	0.89	$5 \cdot 10^{-6}$
	$\text{nil} \rightarrow V_I^\bullet + V'_{\text{FA}} + \text{FAI}$	0.45	0.63	$2 \cdot 10^{-8}$
	$\text{nil} \rightarrow V_{\text{Br}}^\bullet + V'_{\text{FA}} + \text{FABr}$	0.51	0.62	$1 \cdot 10^{-10}$
	$\text{nil} \rightarrow V''_{\text{Pb}} + 2V_I^\bullet + \text{PbI}_2$	0.23	0.36	$1.8 \cdot 10^{-4}$
	$\text{nil} \rightarrow V''_{\text{Pb}} + 2V_{\text{Br}}^\bullet + \text{PbBr}_2$	0.47	0.53	$2 \cdot 10^{-9}$
17 mol%	$\text{nil} \rightarrow V''_{\text{Pb}} + (3-x)V_I^\bullet + xV_{\text{Br}}^\bullet + V'_{\text{FA}} + \text{FAPbI}_{3(1-x)}\text{Br}_{3x}$	0.24	0.83	$1.8 \cdot 10^{-4}$
	$\text{nil} \rightarrow V''_{\text{Pb}} + 3V_I^\bullet + V'_{\text{FA}} + \text{FAPbI}_3$	0.20	0.83	$1.2 \cdot 10^{-3}$
	$\text{nil} \rightarrow V_I^\bullet + V'_{\text{FA}} + \text{FAI}$	0.4	0.61	$2 \cdot 10^{-7}$
	$\text{nil} \rightarrow V_{\text{Br}}^\bullet + V'_{\text{FA}} + \text{FABr}$	0.44	0.59	$3 \cdot 10^{-8}$
	$\text{nil} \rightarrow V''_{\text{Pb}} + 2V_I^\bullet + \text{PbI}_2$	0.19	0.32	$9 \cdot 10^{-4}$
	$\text{nil} \rightarrow V''_{\text{Pb}} + 2V_{\text{Br}}^\bullet + \text{PbBr}_2$	0.20	0.45	$2 \cdot 10^{-4}$
FAMA (% Br)				
0 mol%	$\text{nil} \rightarrow V'_{\text{MA}} + V''_{\text{Pb}} + 3V_I^\bullet + \text{MAPbI}_3$	0.48	0.75	$9 \cdot 10^{-9}$
	$\text{nil} \rightarrow V_I^\bullet + V'_{\text{MA}} + \text{MAI}$	0.26	0.40	$5 \cdot 10^{-5}$
	$\text{nil} \rightarrow (1-y)V'_{\text{FA}} + yV'_{\text{MA}} + V''_{\text{Pb}} + 3V_I^\bullet + \text{FA}_{(1-y)}\text{MA}_y\text{PbI}_3$	0.74	0.74	$9 \cdot 10^{-9}$
8 mol%	$\text{nil} \rightarrow V'_{\text{MA}} + V''_{\text{Pb}} + 3V_I^\bullet + \text{MAPbI}_3$	0.81	1.01	$2 \cdot 10^{-14}$
	$\text{nil} \rightarrow V_I^\bullet + V'_{\text{MA}} + \text{MAI}$	0.28	0.32	$2 \cdot 10^{-5}$

17 mol%	$\text{nil} \rightarrow (1-y)V'_{\text{FA}} + yV'_{\text{MA}} + V''_{\text{Pb}} + 3(1-x)V_I^* + 3xV_{\text{Br}}^* + \text{FA}_{(1-y)}\text{MA}_y\text{PI}_{3(1-x)}\text{Br}_{3x}$	0.57	0.71	$6 \cdot 10^{-10}$
	$\text{nil} \rightarrow V'_{\text{MA}} + V''_{\text{Pb}} + 3V_I^* + \text{MAPbI}_3$	0.80	1.09	$3 \cdot 10^{-14}$
	$\text{nil} \rightarrow V_I^* + V'_{\text{MA}} + \text{MAI}$	0.29	0.39	$1 \cdot 10^{-5}$
	$\text{nil} \rightarrow (1-y)V'_{\text{FA}} + yV'_{\text{MA}} + V''_{\text{Pb}} + 3(1-x)V_I^* + 3xV_{\text{Br}}^* + \text{FA}_{(1-y)}\text{MA}_y\text{PbI}_{3(1-x)}\text{Br}_{3x}$	0.72	1.01	$2 \cdot 10^{-12}$

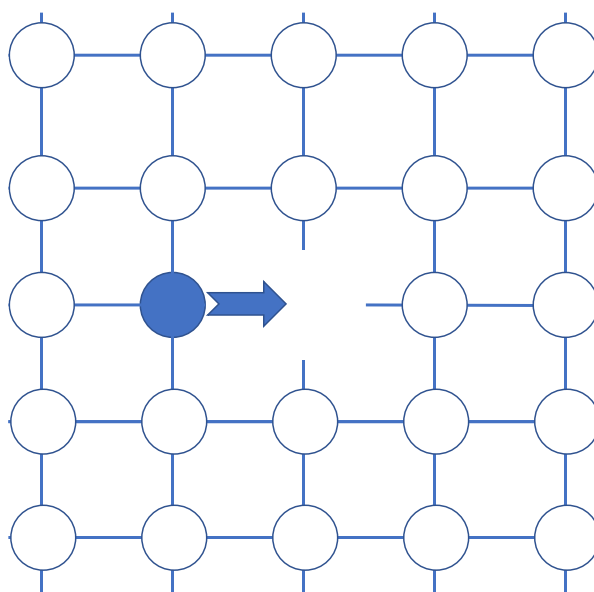


**Fig. S6.** Cartoon of the vacancy mechanism diffusion mechanism. The blue atom moves into the vacancy. In absence of a driving force this movement is random and produces no ionic current. However, in presence of an electric field movement along and against the field have different probability, resulting in a net current.

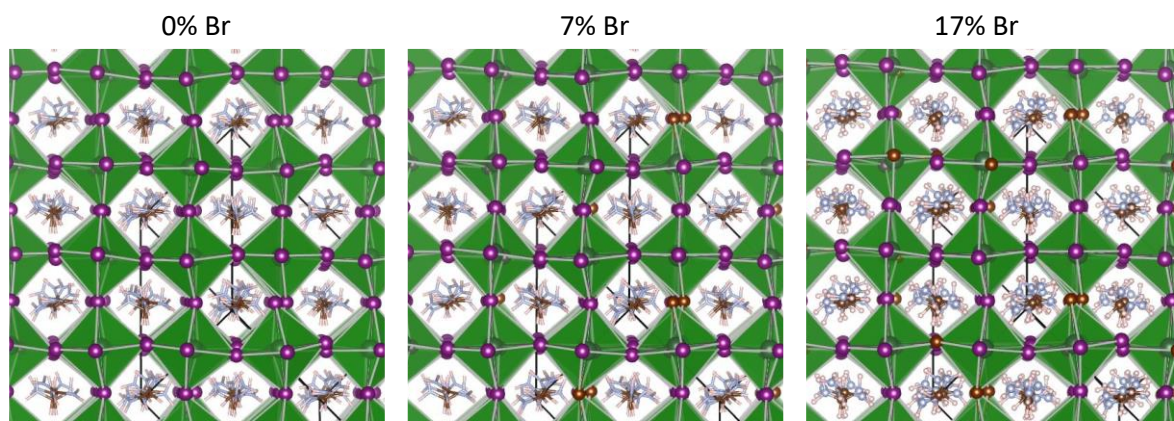


**Fig. S7.**  $\text{FAPbI}_{3(1-x)}\text{Br}_{3x}$  computational samples with 0, 7 and 17 mol% Br content; grey, violet and brown spheres represent Pb, I and Br, respectively. The FA cation is drawn in stick representation.

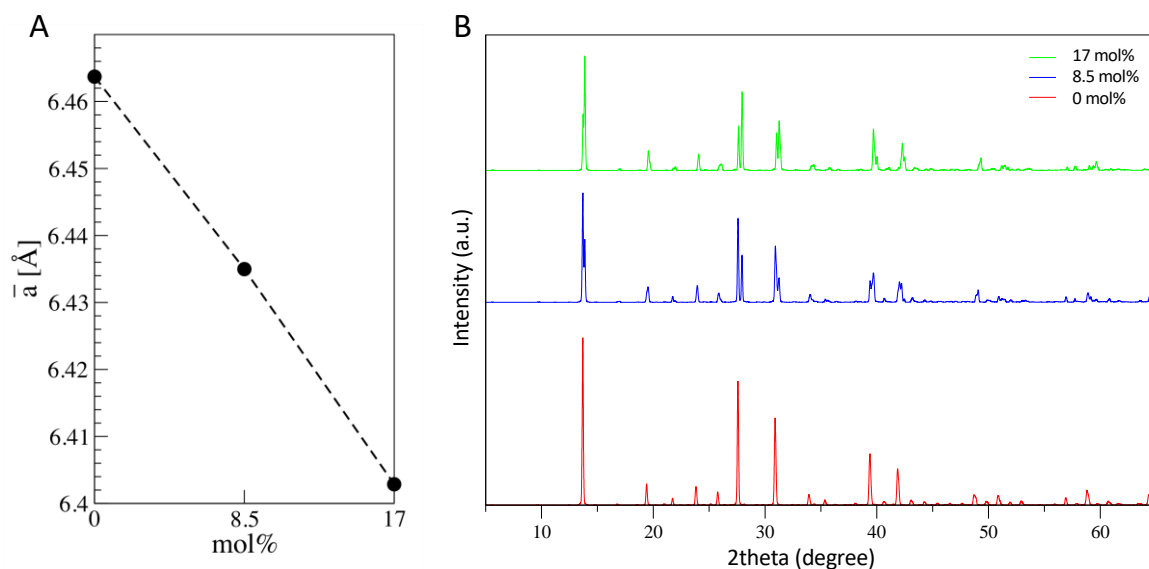


**Fig. S8. (A)** Pseudo-cubic lattice parameter,  $\bar{a} = \sqrt[3]{V}$  with  $V$  volume of the unit cell, vs the bromide content of the sample.  $\bar{a}$  shows a reduction of  $\sim 0.4\%$  in going from 0 to 8.5 mol% and of  $\sim 0.4\%$  in going from 8.5 to 17 mol% of bromide. **(B)** Theoretical XRD pattern at the 0, 8.5, 17 mol% bromide content obtained from the atomistic structure after configuration and lattice optimization. We remark that the theoretical pattern has been obtained assuming no preferential orientation of the crystallites, which might affect the relative intensity of the peaks with respect to the experimental data. We also remark that in (static) DFT calculations one can observe an ‘artificial’ splitting of peak associated to a break of symmetry induced by the given orientation of FA ions in the sample.



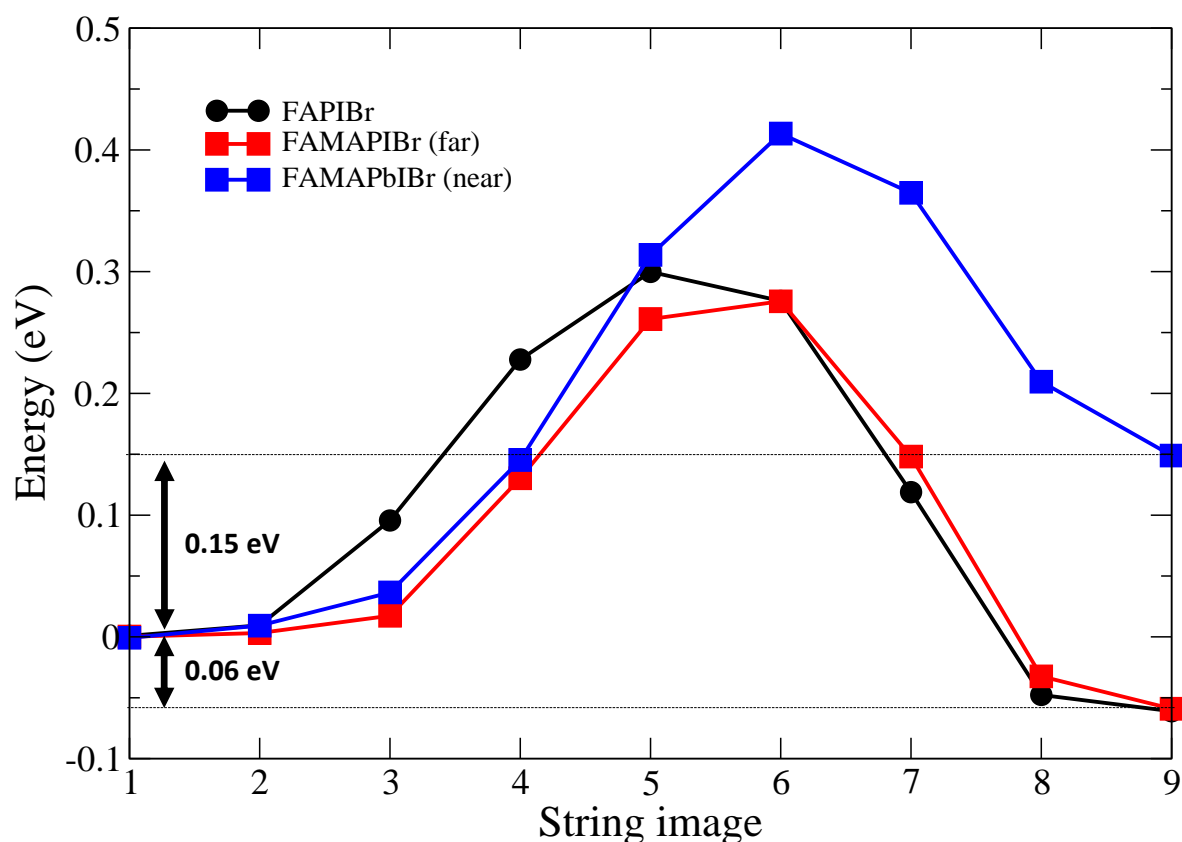


**Fig. S9.** Energy profile along the migration path of a  $\text{Br}^-$  ion in a 17 mol% bromide sample without (black) and with (red and blue) FA/MA mixed cations. We considered two cases, i) when the halide migration event takes place on the edge of a cubic-like cell containing the MA cation (blue) and ii) when it takes place in a cell sharing a corner with the one containing MA (red). One notices that the free energy profile of the pure FA sample is very similar to that of the mixed cation when MA is not in the cell of the migrating  $\text{Br}^-$ : the barriers differ by only 0.02 eV and the difference of relative stability between the initial and final configuration has the same sign and magnitude (the final state is more stable of the initial one by 0.06 eV). On the contrary, when the MA is in the cell of the migrating  $\text{Br}^-$  its dipole moment alters the relative stability of the final vs initial state. However, also in this case the average forth and back barrier is within 0.02 eV from the barrier of the pure FA cation sample.

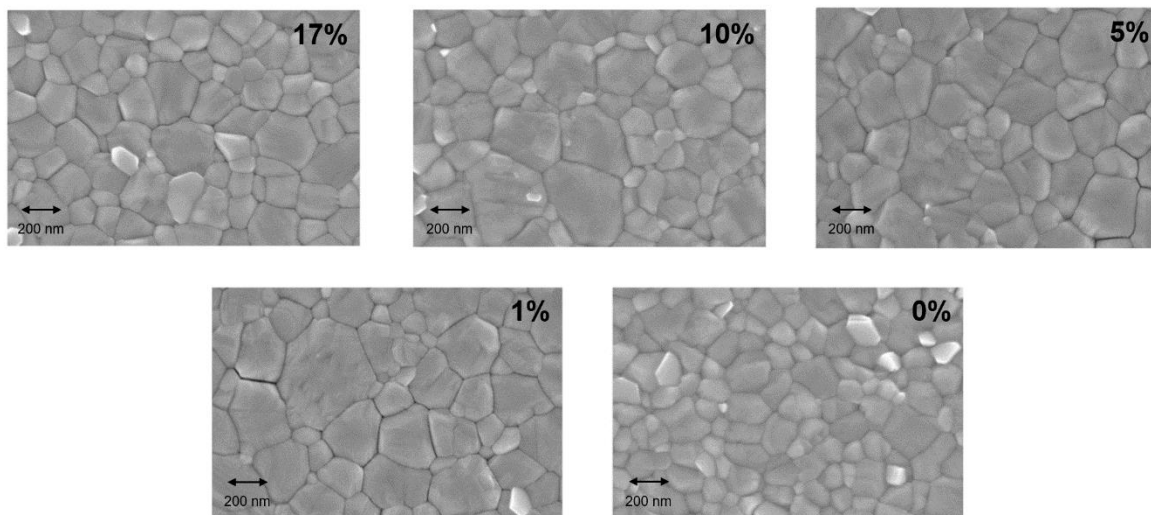


**Fig. S10.** Top surface SEM images for triple cation perovskite with different bromide concentrations.

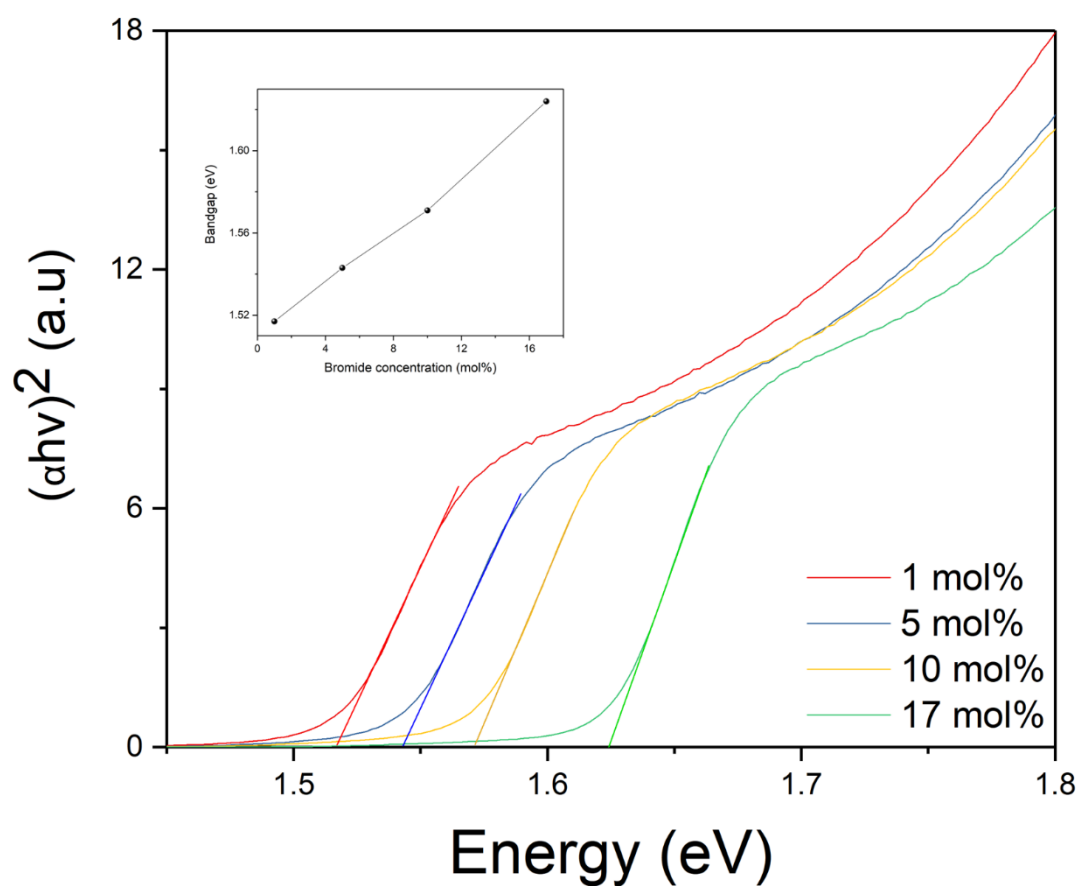


**Fig. S11.** Tauc plot showing the shift in bandgap with change in bromide concentration.

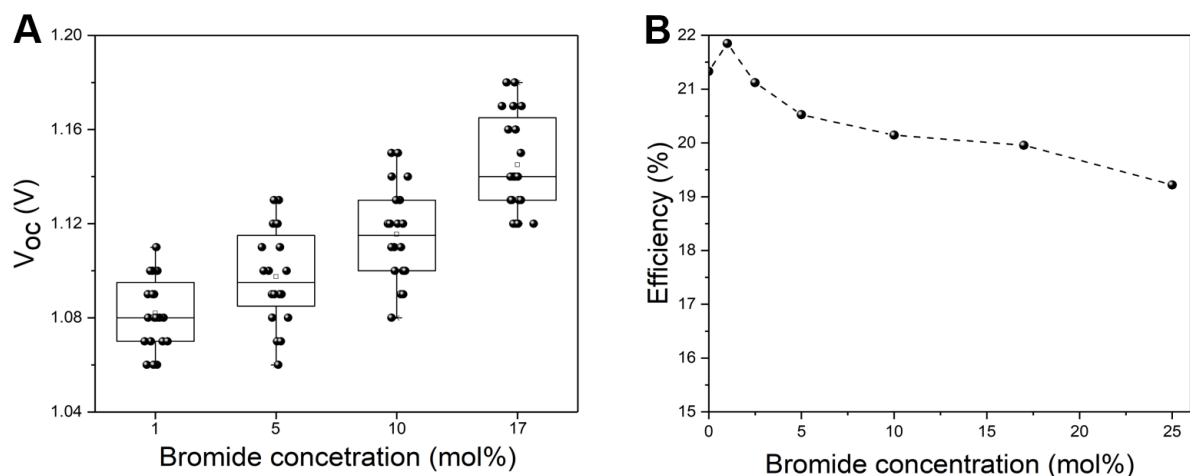


**Fig. S12. (A)** Trend of  $V_{oc}$  with different bromide concentration. **(B)** Trend of average power conversion efficiency with change in bromide concentration for  $(FA_{0.83}MA_{0.7})_{0.95}Cs_{0.05}Pb(I_{1-x}Br_x)_3$

**Table S3.** JV parameters with variation in FA, MA and Cs concentrations with 1% bromine

Composition	$V_{oc}$ (V)	$J_{sc}$ (mA/cm <sup>2</sup> )	FF (%)	PCE (%)
$(FA_{0.5}MA_{0.5})_{0.95}Cs_{0.05}Pb(I_{0.99}Br_{0.01})_3$	0.87	11.4	57	5.85
$(FA_{0.75}MA_{0.25})_{0.95}Cs_{0.05}Pb(I_{0.99}Br_{0.01})_3$	1.08	21.9	73	17.2
$(FA_{0.83}MA_{0.17})_{0.95}Cs_{0.05}Pb(I_{0.99}Br_{0.01})_3$	1.07	25.8	81	22.4
$(FA_{0.9}MA_{0.1})_{0.95}Cs_{0.05}Pb(I_{0.99}Br_{0.01})_3$	1.06	25.8	80	21.9
$(FA_{0.95}MA_{0.05})_{0.95}Cs_{0.05}Pb(I_{0.99}Br_{0.01})_3$	1.05	25.4	78	21.2
$FA_{0.95}Cs_{0.05}Pb(I_{0.99}Br_{0.01})_3$	1.06	24.2	76	19.5
$(FA_{0.83}MA_{0.17})_{0.95}Cs_{0.1}Pb(I_{0.99}Br_{0.01})_3$	1.0	23.3	65	15.5
$(FA_{0.83}MA_{0.17})_{0.95}Cs_{0.025}Pb(I_{0.99}Br_{0.01})_3$	1.11	24.8	79	22.1
$(FA_{0.83}MA_{0.17})Pb(I_{0.99}Br_{0.01})_3$	0.99	23.8	64	15.4



## *Chapter 4: TiO<sub>2</sub> colloids as low temperature alternative to mesoporous TiO<sub>2</sub>*

(to be submitted, manuscript under preparation)

### **Motivation**

Perovskite solar cells have shown steep improvement in performance in a short period of time. Replacing mesoporous TiO<sub>2</sub> with a thinner layer of SnO<sub>2</sub> has been demonstrated to improve open circuit voltage ( $V_{oc}$ ). But SnO<sub>2</sub> suffers from a lower current density ( $J_{sc}$ ) which limits its overall efficiency. Herein, we show that using a thin layer of smaller size TiO<sub>2</sub> nanoparticles provide an even higher  $V_{oc}$  of around 1.19V without compromising  $J_{sc}$  with an efficiency of 24.3%. We demonstrate via PLQY and TRPL measurements that a thin layer of TiO<sub>2</sub> can reduce interfacial recombination. Moreover, these nanoparticles provide an added advantage of low temperature processability at around 150°C which enables scaling up.

### **Introduction**

Perovskite solar cells (PSCs) have managed to reach high efficiencies crossing 25%<sup>2</sup> in a very short period of time, making it a viable alternative to Silicon solar cells. In general, PSC uses a device structure of n-i-p stack where the n-type layer generally is transparent metal oxide electrode. Currently, numerous n-type metal oxides such as TiO<sub>2</sub><sup>84,108</sup>, SnO<sub>2</sub><sup>109,110</sup>, ZnO<sup>110,111</sup>, Zn<sub>2</sub>SO<sub>4</sub><sup>112–114</sup>, WO<sub>3</sub><sup>115–117</sup>, In<sub>2</sub>O<sub>3</sub><sup>118–120</sup>, SrTiO<sub>3</sub><sup>121,122</sup>, Nb<sub>2</sub>O<sub>3</sub><sup>123–125</sup>, CeO<sub>x</sub><sup>126</sup>, BaTiO<sub>3</sub><sup>127,128</sup> and BaSnO<sub>3</sub><sup>129</sup> have been reported as ETLs. Among these, TiO<sub>2</sub> is the most commonly used ETL in PSCs, especially in high efficiency PSCs. A standard device consists of a compact amorphous layer of TiO<sub>2</sub> deposited by spray pyrolysis and a mesoporous scaffold layer of TiO<sub>2</sub><sup>84</sup> (30-50 nm in size) on top of it before depositing the perovskite absorber layer. The compact layer allows for effective electron collection and the scaffold layer provides extra area for charge extraction to compensate for the lower diffusion lengths compared to that of the perovskite absorbers.

Mesoporous TiO<sub>2</sub> exhibits good chemical and thermal stability along with excellent optical and electronic properties. Uniform mesoporous channels of TiO<sub>2</sub> can not only provide increased density of active sites but also facilitate the diffusion of electrons, the high surface area and large pore enable the growth of a compact and uniform perovskite layer.<sup>130</sup> But

mesoporous TiO<sub>2</sub> layers suffer from issues of charge recombination at the interface and hence voltage loss along with photo induced instability.<sup>131</sup> This led to the researchers exploring substitutes for TiO<sub>2</sub>.

Among the alternate options, SnO<sub>2</sub> emerged as the most successful substitute for TiO<sub>2</sub>. SnO<sub>2</sub> could be used as both a compact<sup>132</sup> and a mesoporous layer<sup>133</sup> in PSCs. SnO<sub>2</sub> showed better band alignment with perovskite solar cells which resulted in higher V<sub>oc</sub>.<sup>134,135</sup> Initial results by Hagfeldt et.al.<sup>109</sup> with an amorphous layer of SnO<sub>2</sub> deposited using chemical bath deposition showed higher V<sub>oc</sub> but lower current densities. But jingbi you et.al.<sup>42</sup> managed to get very high currents with certified efficiencies of 23.3% using SnO<sub>2</sub> nanoparticles. Thus SnO<sub>2</sub> emerged as a more desirable alternative for TiO<sub>2</sub> because it could maintain high device performance with the added advantage of low temperature processability and no toxic solvents required for dispersion.

Even with all the success of SnO<sub>2</sub> as ETL including the record efficiencies achieved by Jason et.al. of 25.2%<sup>70</sup> using CBD deposited SnO<sub>2</sub> as ETL, it still does not match the currents that could be achieved with mesoporous TiO<sub>2</sub><sup>136</sup>. And while mesoporous TiO<sub>2</sub> can generate higher currents it fails to provide the V<sub>oc</sub> that SnO<sub>2</sub> can achieve. To tackle this problem, we replace 30-50nm TiO<sub>2</sub> with smaller TiO<sub>2</sub> nanoparticles (4-8 nm in size). Smaller size TiO<sub>2</sub> nanoparticles have been tried in the past with some success but its main application has been as a surface treatment (TiCl<sub>4</sub> treatment)<sup>137,138</sup> on compact TiO<sub>2</sub> layer to improve the band alignment. In our case we use TiO<sub>2</sub> nanoparticles (4-8 nm) dispersed in water. We discovered that these nanoparticles can be used just like SnO<sub>2</sub> nanoparticles as a stand-alone ETL replacing the much thicker mesoscopic TiO<sub>2</sub> ETL whose fabrication require a temperature of around 500 °C to achieve high efficiency PSCs. Our new method employs low temperature without the use of any toxic solvents. However, these nanoparticles show much improved optoelectronics when used along with a compact TiO<sub>2</sub> layer.

In this work, we show that replacing the mesoporous TiO<sub>2</sub> with smaller size TiO<sub>2</sub> nanoparticles results in an improved open circuit voltage of PSCs while removing the need of high temperature annealing. We also compare these nanoparticles with the commercially obtained SnO<sub>2</sub> nanoparticles and showing that these nanoparticles are a better low

temperature alternative to both mesoporous  $\text{TiO}_2$  nanoparticles as well as the  $\text{SnO}_2$  nanoparticles.

### Nanoparticle properties

For the  $\text{TiO}_2$  nanoparticles it is important to have them in the anatase phase as in this phase the perovskite crystal growth is best. For the standard mesoporous  $\text{TiO}_2$ , anatase phase is obtained after annealing the particles at  $450^\circ\text{C}$  (ref) to get rid of the organic ligands attached to the particles. In contrast, the nanoparticles we use are dispersed in deionised water without any organic ligands. Hence, there is no need to anneal the particles at high temperatures. We annealed the film by spin coating the dispersed particles on FTO and annealing the substrate at  $150^\circ\text{C}$  to ensure the evaporation of any water remaining on the film. XRD (**Fig 1A**) shows that the film obtained after annealing at  $150^\circ\text{C}$  show identical peaks with the mesoporous  $\text{TiO}_2$ , the 101 plane at  $2\theta=26^\circ$  being the dominant plane. This was further verified with HRTEM images (**Fig 1B**) of the nanoparticles which show the presence of the **101** plane with an average particle size of about 4nm. This is in accordance with previously published results of similar nanoparticles.<sup>139,140</sup>

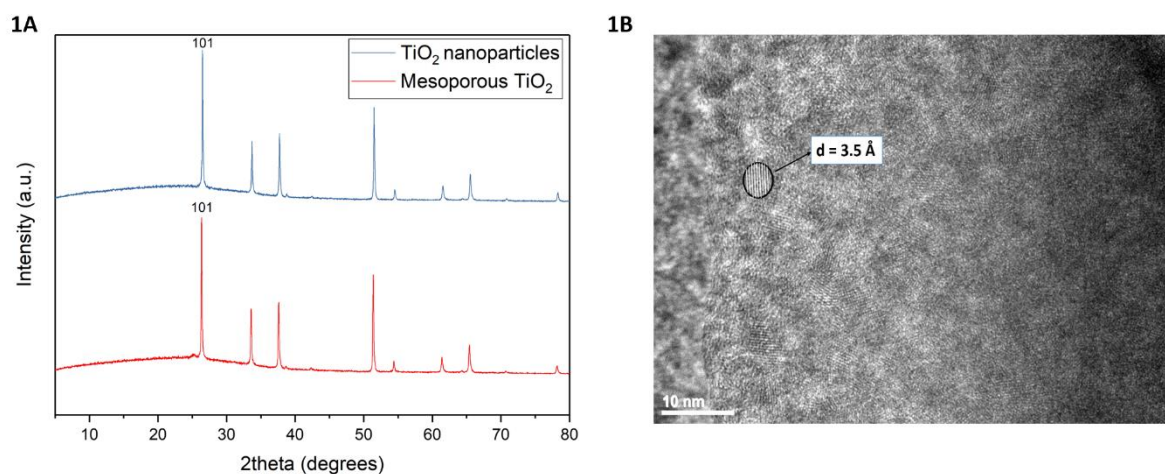


**Fig 1A.** XRD measurements showing identical peaks for both mesoporous and colloidal  $\text{TiO}_2$  films prepared on FTO. **Fig 1B.** HRTEM images of colloidal  $\text{TiO}_2$  nanoparticles showing the presence of 101 plane with particles of around 4nm.

We measured the Tyndall effect to check for light scattering due to particle agglomeration. We used commercially obtained  $\text{SnO}_2$  nanoparticles as the standard. We found that the light scattering was higher for  $\text{SnO}_2$  nanoparticles compared to our  $\text{TiO}_2$  nanoparticles at the same

concentration **Fig 2A**. We discovered that these nanoparticles can be used just like  $\text{SnO}_2$  nanoparticles as a stand-alone ETL replacing the much thicker mesoscopic  $\text{TiO}_2$  ETL whose fabrication require a temperature of around  $500^\circ\text{C}$  to achieve high efficiency PSCs. Our new method employs a low temperatures without the use of any toxic solvents. However, these nanoparticles show much improved optoelectronics when used along with a compact  $\text{TiO}_2$  layer.

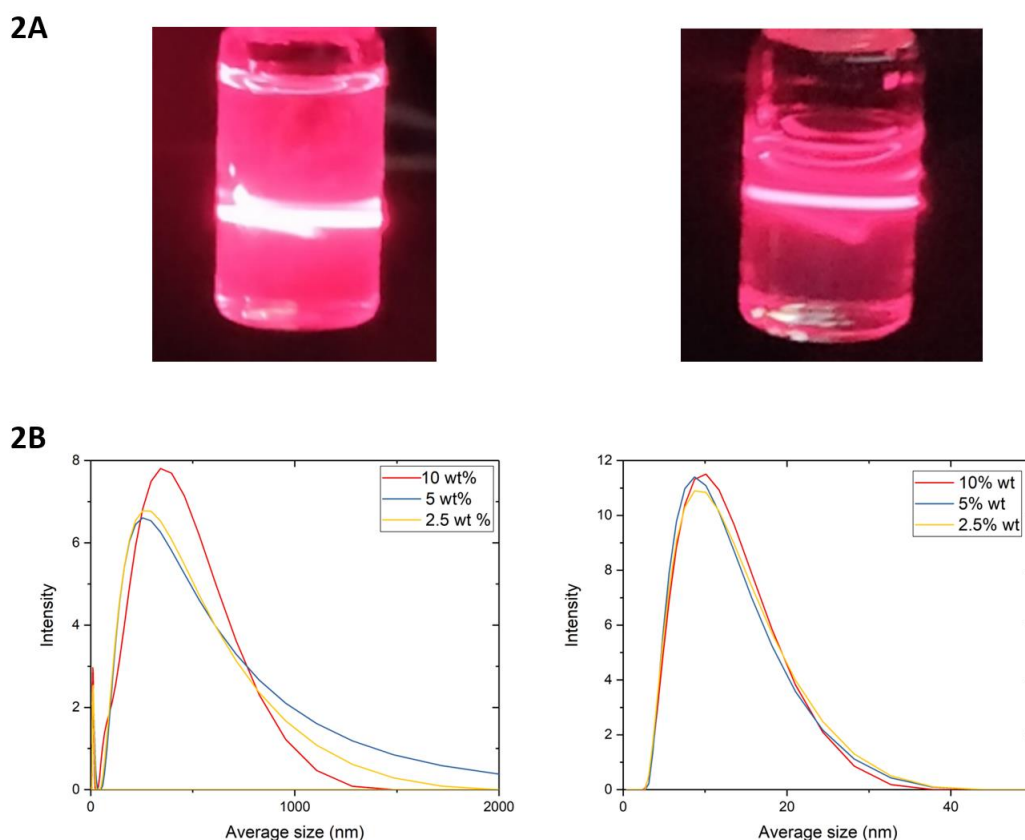


**Fig 2A.** Photograph showing the light scattering in nanoparticles  $\text{SnO}_2$  (left) and  $\text{TiO}_2$  (right) at 5% wt concentration of nanoparticles dispersed in DI  $\text{H}_2\text{O}$ . **Fig 2B.** DLS comparison between  $\text{SnO}_2$  (left) and  $\text{TiO}_2$  (right) nanoparticles at 2.5, 5, 10 wt% of solution showing much higher agglomeration for  $\text{SnO}_2$  compared to  $\text{TiO}_2$  nanoparticles.

## Results and discussions

We then study the morphology of the film obtained by depositing these nanoparticles on FTO. Due to the small size of the colloids we can see that the nanoparticles go and settle in the crevices of FTO for both  $\text{TiO}_2$  and  $\text{SnO}_2$  forming a very compact layer of the ETL. But for the



same concentrations the SnO<sub>2</sub> nanoparticles seem to not fully cover the FTO (**Fig 3A**). This results in a lack of reproducibility of SnO<sub>2</sub> devices. This can be partly countered by increasing the concentration of SnO<sub>2</sub> solution concentration. Even though the TiO<sub>2</sub> seems to cover the FTO well but we can still see cracks at the edge of the FTO (**Fig 3B**) which results in a decrease of FF due to bad contact at those cracks.

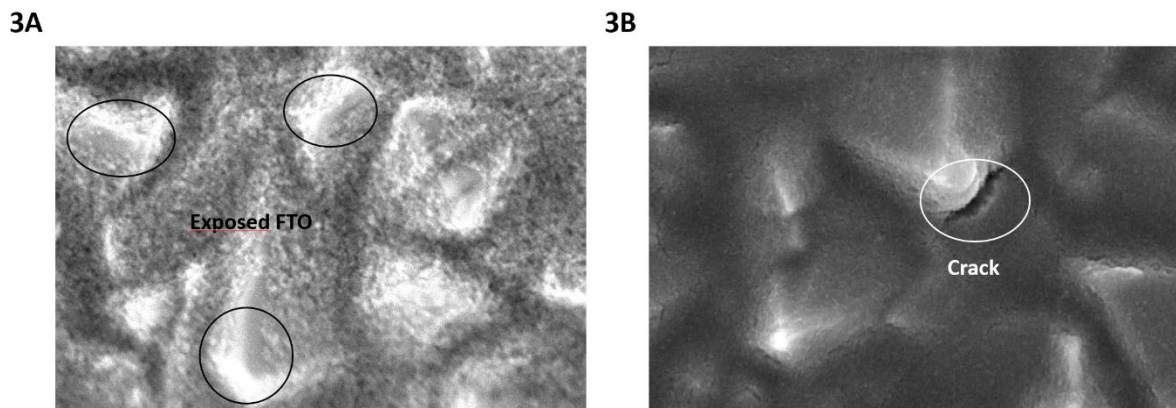
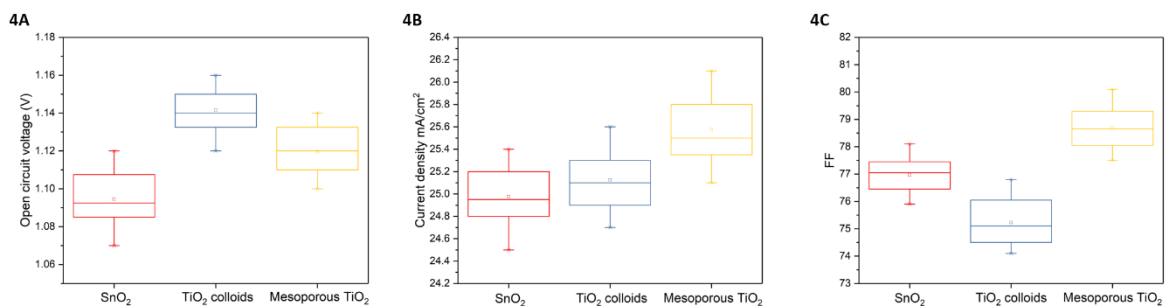


Fig 3. Top surface SEM images of SnO<sub>2</sub> (**3A**) and TiO<sub>2</sub> (**3B**) nanoparticles at 5 wt% of solution

We fabricated devices with an n-i-p structure where the absorber is a predominantly FAPbI<sub>3</sub> with 2.5% wt of MAPbBr<sub>3</sub> and 35% MACl and the p-type hole conductor is the standard Spiro-OMETAD. We saw an improved device performance for TiO<sub>2</sub> nanoparticles in regards to current and voltage (**Fig 4**) compared to the SnO<sub>2</sub> nanoparticles there is a significant drop in FF which made it undesirable in comparison to the mesoporous TiO<sub>2</sub> nanoparticles as the decrease in FF was higher than the increase in V<sub>oc</sub>.



**Fig 4.** Box plot showing the distribution of device parameters **A.** V<sub>oc</sub> **B.** J<sub>sc</sub> and **C.** FF for SnO<sub>2</sub>, TiO<sub>2</sub> colloids and mesoporous TiO<sub>2</sub>

To solve this problem, we deposited our  $\text{TiO}_2$  nanoparticles on top of a compact  $\text{TiO}_2$  similar to mesoporous  $\text{TiO}_2$  instead of directly on FTO. We notice that the film morphology is significantly improved with the  $\text{TiO}_2$  nanoparticles following the morphology of the FTO (**Fig 5**) instead of filling the cracks and hence avoiding the cracks.

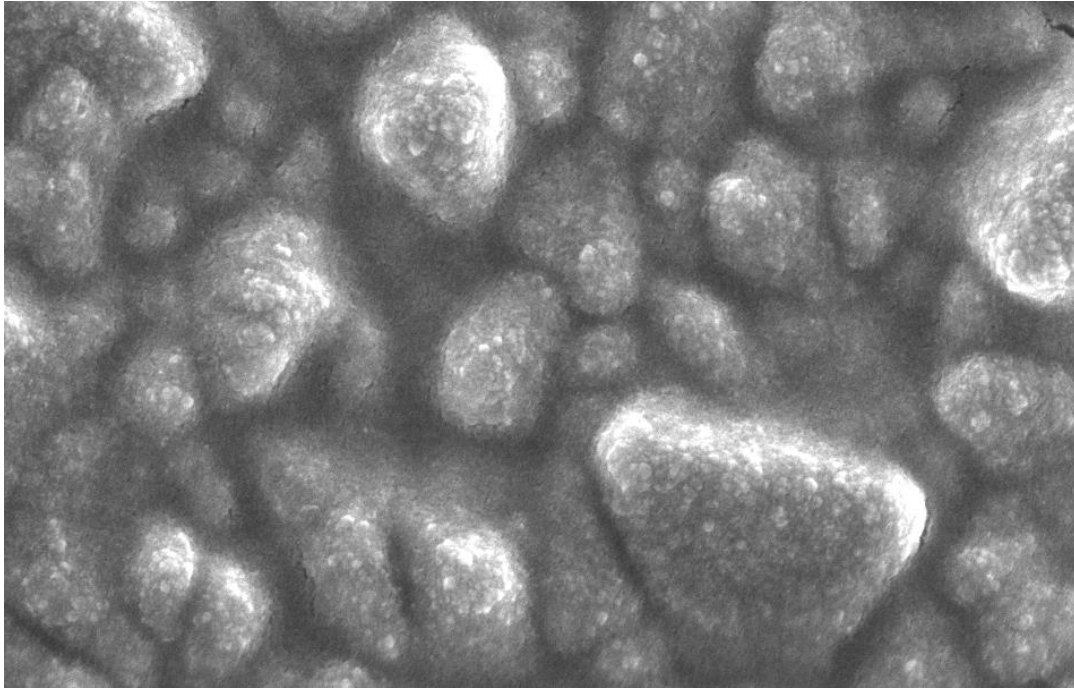


**Fig 5.** Top surface SEM image of  $\text{TiO}_2$  nanoparticles deposited on top of compact  $\text{TiO}_2$

The interface of perovskite and ETL can act as a centre for charge recombination because of the presence of defect states. To measure the effect of different ETL structure on carrier recombination time-resolved photoluminescence (TRPL) was measured. A reduced carrier lifetime implies higher trap densities. The TRPL measurements show (Fig 6A) that the  $\text{TiO}_2$  colloids on top of compact  $\text{TiO}_2$  shows the longest lifetimes compared to standard mesoporous  $\text{TiO}_2$  or a single layer of  $\text{TiO}_2$  or  $\text{SnO}_2$ . This suggests that a thinner layer of  $\text{TiO}_2$  nanoparticles reduces the trap densities while a compact layer of  $\text{TiO}_2$  is also necessary for appropriate charge extraction.

To further verify our measurements from TRPL we measured the photoluminescence quantum yield (PLQY) to calculate the quasi-fermi level splitting. We found that the results of the PLQY match very well with the TRPL measurements with the  $\text{TiO}_2$  colloids on top of

compact TiO<sub>2</sub> showing higher QFLS with over 30eV (Table 1) increase over the standard mesoporous TiO<sub>2</sub>.

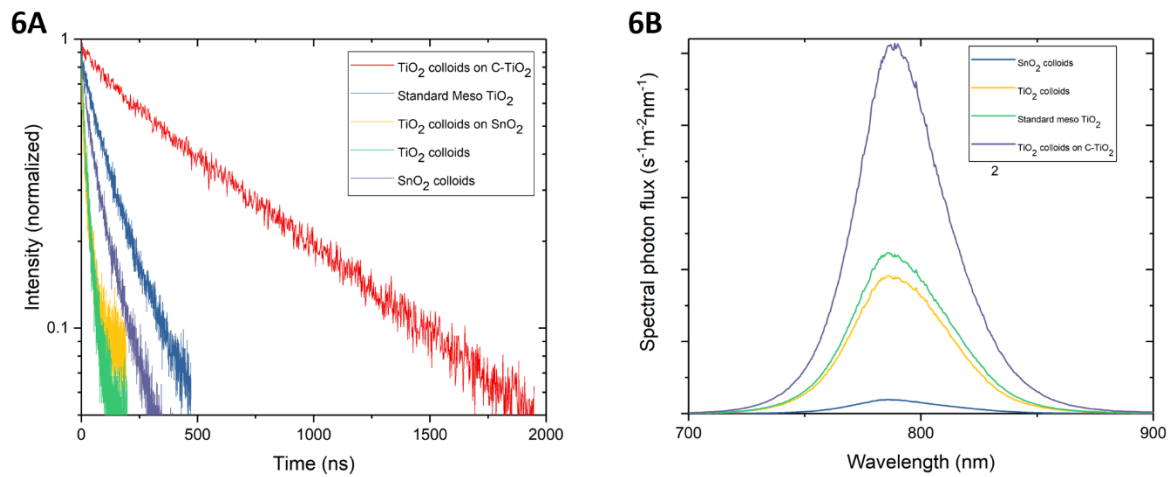


**Fig 6A.** TRPL measurements showing much improved carrier lifetimes for perovskite deposited on top TiO<sub>2</sub> colloids deposited on top of compact TiO<sub>2</sub> compared to mesoporous TiO<sub>2</sub> or SnO<sub>2</sub>. **Fig 6B.** PLQY measurements showing same results as TRPL with the yield being highest for perovskite deposited on top TiO<sub>2</sub> colloids deposited on top of compact TiO<sub>2</sub>

**Table 1.** QFLS derived from the PLQY measurements show that TiO<sub>2</sub> colloids show an improvement of around 30 meV compared to the mesoporous TiO<sub>2</sub>

	PLQY	QFLS/q (V)
TiO <sub>2</sub> colloids on c-TiO <sub>2</sub>	2e-2	1.203
Standard meso TiO <sub>2</sub>	7.2e-3	1.173
TiO <sub>2</sub> colloids	1.8e-3	1.133
SnO <sub>2</sub> colloids	1.5e-4	1.078

Based on our devices we notice a significant increase in the open circuit voltage with TiO<sub>2</sub> colloids compared to the standard mesoporous TiO<sub>2</sub>. The colloids show an average increase of around 55 mV when deposited on top of compact TiO<sub>2</sub> layer similar to the standard

mesoporous TiO<sub>2</sub> devices (**Fig 7**). But we also notice the FF with these colloidal nanoparticles was still on average 2% lower than the mesoporous TiO<sub>2</sub>. This was because the concentration of the solution and hence the thickness of the layer was not optimised. So we varied the solution concentration from 20 wt% to 0.5 wt%. We measured the TEM (**Fig 8**) for 10 wt% and 2 wt% concentration solutions noticing that the particles aggregate at higher concentrations while at lower concentration we don't see any aggregation. At 2 wt% concentration we were able to obtain the best device performance (Table 2) with FF and J<sub>sc</sub> almost identical to mesoporous TiO<sub>2</sub> devices with an increase of 55 mV in V<sub>oc</sub>. Our champion device showed an efficiency of 24.3% with a V<sub>oc</sub> of 1.19, J<sub>sc</sub> of 25.78 mA/cm<sup>2</sup> and FF of 79.5 with a hysteresis of around 0.7% due to a lower FF of 77% in the forward bias. This was an increase of 1% in efficiency compared to our best mesoporous TiO<sub>2</sub> devices (**Fig 9**).

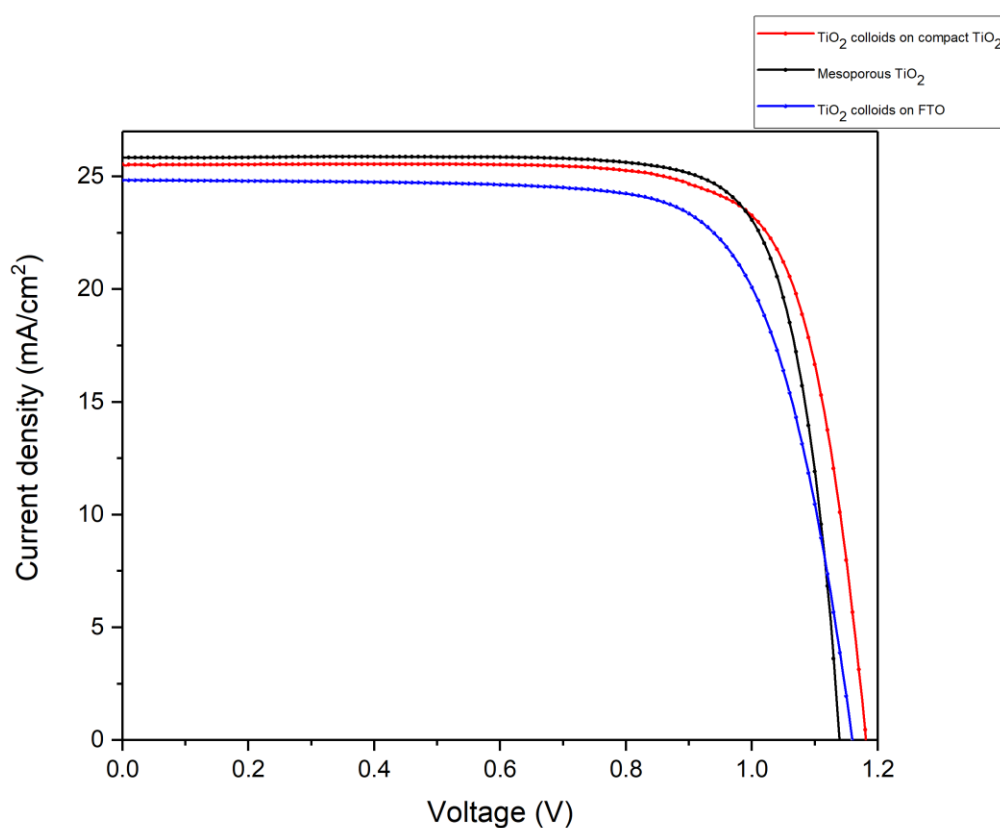
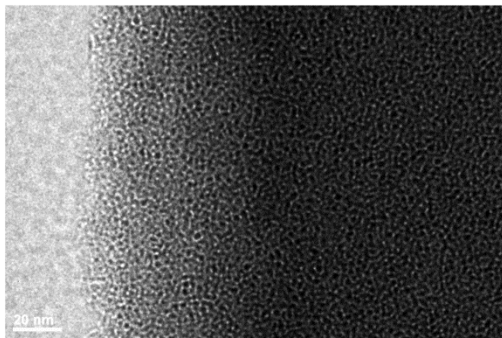


**Fig. 7.** JV plot showing the difference in performance between the best devices obtained with TiO<sub>2</sub> colloids on FTO, Mesoporous TiO<sub>2</sub> and TiO<sub>2</sub> colloids on compact TiO<sub>2</sub> as ETL

Table 2. JV parameters of devices shown in **Fig 7**.

	$V_{oc}$ (V)	$J_{sc}$ (mA/cm <sup>2</sup> )	FF (%)	Efficiency (%)
TiO <sub>2</sub> colloids on FTO	1.16	24.8	73.3	21.1
Mesoporous TiO <sub>2</sub>	1.135	25.8	79.7	23.3
TiO <sub>2</sub> colloids on compact TiO <sub>2</sub>	1.185	25.5	77.5	23.4

**8A**



**8B**

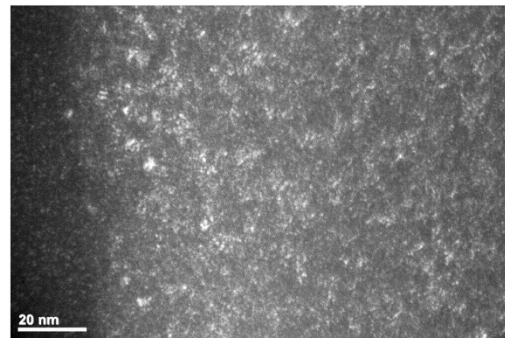


**Fig 8.** Dark field TEM images for **A.** 10 wt% and **B.** 2 wt% solutions

Table 3. Best devices obtained with different concentration of TiO<sub>2</sub> colloids solution

Concentration (wt%)	$V_{oc}$ (V)	$J_{sc}$ (mA/cm <sup>2</sup> )	FF (%)	Efficiency (%)
20	1.11	24.8	71.4	19.5
10	1.14	25.6	76.2	22.1
5	1.16	25.8	77.3	23.1
<b>2</b>	<b>1.19</b>	<b>25.8</b>	<b>79.5</b>	<b>24.3</b>
1	1.18	25.5	78.6	23.6

0.5	1.12	24.4	72.2	19.7
-----	------	------	------	------

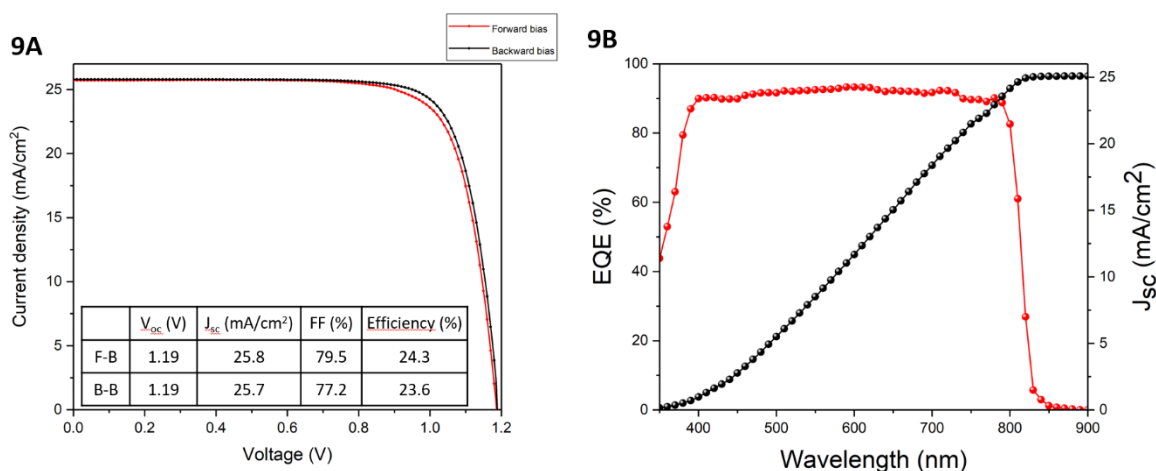


**Fig 9A.** JV plot for the champion device obtained with TiO<sub>2</sub> colloids deposited on compact TiO<sub>2</sub> as ETL. **9B.** IPCE for the same device showing EQE of over 90% between 400 and 700 nm with an integrated current of 25.05 mA/cm<sup>2</sup>

## Conclusion

From this work, we demonstrate that smaller size TiO<sub>2</sub> nanoparticles are better to reduce charge carrier recombination at the ETL-perovskite interface thus resulting in higher V<sub>oc</sub>. We also show that the compact layer is important to support the contiguous and conformal deposition of these nanoparticles. Moreover, the thickness of the layer plays an important role in determining the FF of the device. Further treatment of this layer could help us push the efficiency to new record levels.

## Experimental section

### ETL deposition

TiO<sub>2</sub> and SnO<sub>2</sub> nanoparticles were diluted in DI water and spin coated on FTO or compact TiO<sub>2</sub> at 3000 rpm for 30 seconds. The film was then annealed at 150°C for an hour.

### Perovskite precursor solution

The perovskite films were deposited using single-step deposition method from the precursor solution. 1.5 M PbI<sub>2</sub> (TCI) and PbBr<sub>2</sub> solutions were prepared in a mixture of DMF (99.8%,

Acros) and DMSO (99.7%, Acros) in volume ratio 4:1. Then 1.25 mol of FAI and MAI (Dyesol) was added into 1 ml of  $\text{PbI}_2$  and 1.25 mol MABr (Dyesol) was added to 1 ml  $\text{PbBr}_2$  solutions. Thereafter, 1.5M CsI, RbI and KI (ABCR, GmbH, ultra dry; 99.998%) solution was prepared in DMSO. The solutions were added in appropriate ratios to together to obtain the final perovskite solution. The precursor solution was spin-coated onto the mesoporous  $\text{TiO}_2$  films in a two-step programme at 1000 and 4000 r.p.m. for 10 and 25 s, respectively. During the second step, 200  $\mu\text{l}$  of chlorobenzene (99.8%, Acros) was dropped on the spinning substrate 5 s prior to the end of the programme. This was followed by annealing the films at 100 °C for 60 min

## Chapter 4. Experimental procedure

### Substrate preparation

Nippon Sheet Glass 10  $\Omega/\text{sq}$  was cleaned by sonication in 2% Hellmanex water solution for 15 minutes. After rinsing with deionised water and ethanol, the substrates were further cleaned with UV ozone treatment for 15 min. Then, 30 nm  $\text{TiO}_2$  compact layer was deposited on FTO via spray pyrolysis at 450 °C from a precursor solution of titanium diisopropoxide bis(acetylacetonate) (0.6 ml) in anhydrous ethanol (9 ml). After the spraying, the substrates were left at 450 °C for 45 min and left to cool down to room temperature. Then, mesoporous  $\text{TiO}_2$  layer was deposited by spin coating for 20 s at 4000 rpm with a ramp of 2000 rpm/s, using 30 nm particle paste (Dyesol 30 NR-D) diluted in ethanol (1:6 wt) to achieve 150-200 nm thick layer. After the spin coating, the substrates were immediately dried at 100 °C for 10 min and then sintered again at 450 °C for 30 min under dry air flow.

### Deposition of hole transporting layer

To complete the fabrication of devices, 2,2',7,7'-tetrakis(N,N-di-pmethoxyphenylamine)-9,9-spirobifluorene (spiro-OMeTAD, 70 mM in chlorobenzene) as a hole-transporting material (HTM) was deposited by spin coating 40  $\mu\text{L}$  of the prepared solution at 4000 rpm for 30 s. The spiro-OMeTAD (Merck) was doped with bis(trifluoromethylsulfonyl)imide lithium salt, tris(2-(1H-pyrazol-1-yl)-4-tertbutylpyridine)-cobalt(III) tris(bis(trifluoromethylsulfonyl) imide) (FK 209, from Dyenamo) and 4-tert-Butylpyridine (96%, Sigma-Aldrich) in a molar ratio of 0.5, 0.03 and 3.3, respectively. Finally, device fabrication was completed by thermally evaporating 80 nm of gold layer as a back contact.

### Perovskite film characterization

Perovskite films were characterized by high resolution scanning electron microscopy (SEM), X-ray diffraction (XRD), UV-Vis absorption, and photoluminescence (PL) spectroscopy. Samples for XRD were mounted on the reflection-transmission spinner. XRD were recorded by Empyrean (Panalytical) equipped with a ceramic tube (Cu anode,  $\lambda = 1.54060 \text{ \AA}$ ) and a PIXcel<sup>1D</sup> (Panalytical) in an angle range of  $2\theta = 5^\circ$  to  $60^\circ$  under ambient conditions. ZEISS Merlin were used for collecting SEM images. UV-vis measurements were performed on a Varian Cary 5 to analyse optical properties of perovskite. PL spectra were obtained with Fluorolog 322 (Horiba Jobin Yvon Ltd) with the range of wavelength from 620 nm to 850 nm



by exciting at 460 nm. The samples were mounted at 60° and the emission recorded at 90° from the incident beam path.

### **J-V measurements**

The solar cells were measured using a 450-W Xenon light source (Oriel). The spectral mismatch between AM1.5G and the simulated illumination was reduced by the use of a Schott K113 Tempax filter (Präzisions Glas & Optik GmbH). The light intensity was calibrated with a Si photodiode equipped with an IR-cutoff filter (KG3, Schott) and it was recorded during each measurement. Current–voltage characteristics of the cells were obtained by applying an external voltage bias while measuring the current response with a digital source meter (Keithley 2400) at a scan rate of 5 mV/s.

### **IPCE measurements**

Incident photon-to-current conversion efficiency measurements were carried from the monochromated visible photons, from Gemini-180 double monochromator Jobin Yvon Ltd. (UK), powered by a 300 W Xenon light source (ILC Technology, USA) superimposed on a 1 mW/cm<sup>2</sup> LED light. The monochromatic incident light was passed through a chopper running at 8 Hz frequency and the on/off ratio was measured by an operational amplifier.

### **Electrochemical impedance spectroscopy (EIS)**

EIS measurements were performed on perovskite devices in the dark using a Biologic SP300 potentiostat and Faraday cage. Devices were exposed to forward bias potentials from 0 V up to 1.1 V in steps of 0.05 V on which a sinusoidal perturbation of 20 mV with a frequency from 500 kHz to 100 mHz was superimposed. Data analysis and equivalent circuit fitting of Nyquist plots was performed using Zview v.2.80, Scriber Associates Inc.

### **Stability measurements**

Stability measurements were performed with a Biologic MPG2 potentiostat under a full AM 1.5 Sun-equivalent white LED lamp. The devices were masked (0.16 cm<sup>2</sup>) and flushed with nitrogen for several hours before the start of the experiment in order to remove residual oxygen and water from the environment of an in-house developed sample holder. Then, the devices were measured with a maximum power point (MPP) tracking routine under continuous illumination (and nitrogen). The MPP was updated every 10 s by a standard perturb and observe method. The temperature of the devices was controlled with a Peltier element in direct contact with the films. The temperature was measured with a surface

thermometer located between the Peltier element and the film. Every 30 min a  $J$ - $V$  curve was recorded in order to track the evolution of individual  $J$ - $V$  parameters.

## References

1. Akihiro Kojima,<sup>†</sup> Kenjiro Teshima,<sup>‡</sup> Yasuo Shirai, and T. M. Organometal Halide Perovskites as Visible- Light Sensitizers for Photovoltaic Cells. *J Am Chem Soc* **131**, 6050–6051 (2009).
2. National Renewable Energy Laboratory (NREL). Research Cell Efficiency Records Chart. *National Center for Photovoltaics* (2020).
3. Roy, P., Kumar Sinha, N., Tiwari, S. & Khare, A. A review on perovskite solar cells: Evolution of architecture, fabrication techniques, commercialization issues and status. *Solar Energy* **198**, (2020).
4. Bartel, C. J. *et al.* New tolerance factor to predict the stability of perovskite oxides and halides. *Sci. Adv.* **5**, (2019).
5. Park, N. G. Perovskite solar cells: An emerging photovoltaic technology. *Materials Today* **18**, (2015).
6. Guo, X. *et al.* Identification and characterization of the intermediate phase in hybrid organic-inorganic MAPbI<sub>3</sub> perovskite. *Dalt. Trans.* **45**, (2016).
7. Lin, C., Li, S., Zhang, W., Shao, C. & Yang, Z. Effect of Bromine Substitution on the Ion Migration and Optical Absorption in MAPbI<sub>3</sub> Perovskite Solar Cells: The First-Principles Study. *ACS Appl. Energy Mater.* **1**, (2018).
8. Zhang, X. M. *et al.* Optical absorption coefficient red shift effect of iodine vacancy in MAPbI<sub>3</sub>. *Comput. Mater. Sci.* **154**, (2018).
9. Jeong, M. J., Yeom, K. M., Kim, S. J., Jung, E. H. & Noh, J. H. Spontaneous interface engineering for dopant-free poly(3-hexylthiophene) perovskite solar cells with efficiency over 24%. *Energy Environ. Sci.* **14**, (2021).
10. Jono, R. & Segawa, H. Theoretical study of the band-gap differences among lead triiodide perovskite materials: CsPbI<sub>3</sub>, MAPbI<sub>3</sub>, and FAPbI<sub>3</sub>. *Chem. Lett.* **48**, (2019).
11. Jiang, S. *et al.* Pressure-dependent polymorphism and band-gap tuning of methylammonium lead iodide perovskite. *Angew. Chemie - Int. Ed.* **55**, (2016).
12. Galkowski, K. *et al.* Determination of the exciton binding energy and effective masses

- for methylammonium and formamidinium lead tri-halide perovskite semiconductors. *Energy Environ. Sci.* **9**, (2016).
13. Mei, A. *et al.* A hole-conductor-free, fully printable mesoscopic perovskite solar cell with high stability. *Science* (80-. ). **345**, (2014).
  14. Wang, D. *et al.* Reproducible one-step fabrication of compact MAPbI<sub>3</sub>-xCl<sub>x</sub> thin films derived from mixed-lead-halide precursors. *Chem. Mater.* **26**, (2014).
  15. Hu, M. *et al.* Efficient hole-conductor-free, fully printable mesoscopic perovskite solar cells with a broad light harvester NH<sub>2</sub>CH=NH<sub>2</sub>PbI<sub>3</sub>. *J. Mater. Chem. A* **2**, (2014).
  16. Lee, J. W., Seol, D. J., Cho, A. N. & Park, N. G. High-efficiency perovskite solar cells based on the black polymorph of HC(NH<sub>2</sub>)<sub>2</sub>PbI<sub>3</sub>. *Adv. Mater.* **26**, (2014).
  17. Eperon, G. E. *et al.* Formamidinium lead trihalide: a broadly tunable perovskite for efficient planar heterojunction solar cells. *Energy Environ. Sci.* (2014).  
doi:10.1039/c3ee43822h
  18. Koh, T. M. *et al.* Formamidinium-containing metal-halide: An alternative material for near-IR absorption perovskite solar cells. *J. Phys. Chem. C* (2014).  
doi:10.1021/jp411112k
  19. Targhi, F. F., Jalili, Y. S. & Kanjouri, F. MAPbI<sub>3</sub> and FAPbI<sub>3</sub> perovskites as solar cells: Case study on structural, electrical and optical properties. *Results Phys.* **10**, (2018).
  20. Li, G. *et al.* Ion-Exchange-Induced 2D–3D Conversion of HMA<sub>1</sub>–xFaxPbI<sub>3</sub>Cl Perovskite into a High-Quality MA<sub>1</sub>–xFaxPbI<sub>3</sub>Perovskite. *Angew. Chemie - Int. Ed.* **55**, (2016).
  21. Kato, M. *et al.* Universal rules for visible-light absorption in hybrid perovskite materials. *J. Appl. Phys.* **121**, (2017).
  22. Leyden, M. R., Jiang, Y. & Qi, Y. Chemical vapor deposition grown formamidinium perovskite solar modules with high steady state power and thermal stability. *J. Mater. Chem. A* **4**, (2016).
  23. Binek, A., Hanusch, F. C., Docampo, P. & Bein, T. Stabilization of the trigonal high-temperature phase of formamidinium lead iodide. *J. Phys. Chem. Lett.* **6**, (2015).

24. Alberti, A. *et al.* Similar Structural Dynamics for the Degradation of CH<sub>3</sub>NH<sub>3</sub>PbI<sub>3</sub> in Air and in Vacuum. *ChemPhysChem* **16**, (2015).
25. Deretzis, I. *et al.* Atomistic origins of CH<sub>3</sub>NH<sub>3</sub>PbI<sub>3</sub> degradation to PbI<sub>2</sub> in vacuum. *Appl. Phys. Lett.* **106**, (2015).
26. Amat, A. *et al.* Cation-induced band-gap tuning in organohalide perovskites: Interplay of spin-orbit coupling and octahedra tilting. *Nano Lett.* **14**, (2014).
27. Lv, S. *et al.* One-step, solution-processed formamidinium lead trihalide (FAPbI<sub>3-x</sub>Cl<sub>x</sub>) for mesoscopic perovskite-polymer solar cells. *Phys. Chem. Chem. Phys.* **16**, (2014).
28. Xu, X. *et al.* Elimination of Yellow Phase: An Effective Method to Achieve High Quality HC(NH<sub>2</sub>)<sub>2</sub>PbI<sub>3</sub>-based Perovskite Films. *ChemSusChem* **13**, (2020).
29. Zheng, X. *et al.* Improved Phase Stability of Formamidinium Lead Triiodide Perovskite by Strain Relaxation. *ACS Energy Lett.* **1**, (2016).
30. Jiang, S. *et al.* Phase Transitions of Formamidinium Lead Iodide Perovskite under Pressure. *J. Am. Chem. Soc.* **140**, (2018).
31. Brenner, P. *et al.* Triple cation mixed-halide perovskites for tunable lasers. *Opt. Mater. Express* **7**, (2017).
32. Service, R. F. Cesium fortifies next-generation solar cells. *Science (80-. ).* **351**, (2016).
33. Saliba, M. *et al.* Cesium-containing triple cation perovskite solar cells: improved stability, reproducibility and high efficiency. *Energy Environ. Sci.* **9**, 1989–1997 (2016).
34. Saliba, M. *et al.* Incorporation of rubidium cations into perovskite solar cells improves photovoltaic performance. *Science (80-. ).* **354**, 206 LP – 209 (2016).
35. Lu, H. *et al.* Vapor-assisted deposition of highly efficient, stable black-phase FAPbI<sub>3</sub> perovskite solar cells. *Science* **370**, (2020).
36. Gil-Escrig, L., Miquel-Sempere, A., Sessolo, M. & Bolink, H. J. Mixed Iodide-Bromide Methylammonium Lead Perovskite-based Diodes for Light Emission and Photovoltaics. *J. Phys. Chem. Lett.* **6**, (2015).
37. Deschler, F. *et al.* High photoluminescence efficiency and optically pumped lasing in

- solution-processed mixed halide perovskite semiconductors. *J. Phys. Chem. Lett.* **5**, (2014).
38. Jeong, J. *et al.* Pseudo-halide anion engineering for  $\alpha$ -FAPbI<sub>3</sub> perovskite solar cells. *Nature* **592**, (2021).
  39. Kim, J. *et al.* Unveiling the Relationship between the Perovskite Precursor Solution and the Resulting Device Performance. *J. Am. Chem. Soc.* **142**, (2020).
  40. Zhang, C. *et al.* Fabrication Strategy for Efficient 2D/3D Perovskite Solar Cells Enabled by Diffusion Passivation and Strain Compensation. *Adv. Energy Mater.* **10**, (2020).
  41. Niu, T. *et al.* Stable High-Performance Perovskite Solar Cells via Grain Boundary Passivation. *Adv. Mater.* **30**, (2018).
  42. Jiang, Q. *et al.* Surface passivation of perovskite film for efficient solar cells. *Nat. Photonics* **13**, (2019).
  43. Xia, J. *et al.* Deep surface passivation for efficient and hydrophobic perovskite solar cells. *J. Mater. Chem. A* **9**, (2021).
  44. Wang, H. *et al.* Semiconductor heterojunction photocatalysts: Design, construction, and photocatalytic performances. *Chemical Society Reviews* **43**, (2014).
  45. Wu, M. C. *et al.* Achieving High-Performance Perovskite Photovoltaic by Morphology Engineering of Low-Temperature Processed Zn-Doped TiO<sub>2</sub> Electron Transport Layer. *Small* **16**, (2020).
  46. Shahvaranfard, F. *et al.* Engineering of the Electron Transport Layer/Perovskite Interface in Solar Cells Designed on TiO<sub>2</sub> Rutile Nanorods. *Adv. Funct. Mater.* **30**, (2020).
  47. Prochowicz, D. *et al.* Suppressing recombination in perovskite solar cells via surface engineering of TiO<sub>2</sub> ETL. *Sol. Energy* **197**, (2020).
  48. Xiong, L. *et al.* Review on the Application of SnO<sub>2</sub> in Perovskite Solar Cells. *Advanced Functional Materials* **28**, (2018).
  49. Lou, Y. *et al.* A simple route for decorating TiO<sub>2</sub> nanoparticle over ZnO aggregates

- dye-sensitized solar cell. *Chem. Eng. J.* **229**, (2013).
50. Lee, K. N., Kim, W. B., Lee, C. S. & Lee, J. S. Enhancement of photoelectric efficiency in a dye-sensitized solar cell using hollow TiO<sub>2</sub> nanoparticles as an overlayer. *Bull. Korean Chem. Soc.* **34**, (2013).
  51. Burke, A. *et al.* The function of a TiO<sub>2</sub> compact layer in dye-sensitized solar cells incorporating 'planar' organic dyes. *Nano Lett.* **8**, (2008).
  52. Chen, D., Huang, F., Cheng, Y. B. & Caruso, R. A. Mesoporous anatase TiO<sub>2</sub> beads with high surface areas and controllable pore sizes: A superior candidate for high-performance dye-sensitized solar cells. *Adv. Mater.* **21**, (2009).
  53. Hu, H. *et al.* Atomic Layer Deposition of TiO<sub>2</sub> for a High-Efficiency Hole-Blocking Layer in Hole-Conductor-Free Perovskite Solar Cells Processed in Ambient Air. *ACS Appl. Mater. Interfaces* **8**, (2016).
  54. Wu, Y. *et al.* Highly compact TiO<sub>2</sub> layer for efficient hole-blocking in perovskite solar cells. *Appl. Phys. Express* **7**, (2014).
  55. Ke, W. *et al.* Perovskite solar cell with an efficient TiO<sub>2</sub> compact film. *ACS Appl. Mater. Interfaces* **6**, (2014).
  56. Anuratha, K. S., Peng, H. S., Hsieh, C. K., Xiao, Y. & Lin, J. Y. Electrochemical formation of TiO<sub>2</sub> porous layer for perovskite solar cells. *Thin Solid Films* **660**, (2018).
  57. Möllmann, A. *et al.* Highly Compact TiO<sub>2</sub> Films by Spray Pyrolysis and Application in Perovskite Solar Cells. *Adv. Eng. Mater.* **21**, (2019).
  58. Lv, Y. *et al.* High-Efficiency Perovskite Solar Cells Enabled by Anatase TiO<sub>2</sub> Nanopyramid Arrays with an Oriented Electric Field. *Angew. Chemie - Int. Ed.* **59**, (2020).
  59. Idígoras, J. *et al.* The Role of Surface Recombination on the Performance of Perovskite Solar Cells: Effect of Morphology and Crystalline Phase of TiO<sub>2</sub> Contact. *Adv. Mater. Interfaces* **5**, (2018).
  60. Wan, F. *et al.* Accelerated electron extraction and improved UV stability of TiO<sub>2</sub> based perovskite solar cells by SnO<sub>2</sub> based surface passivation. *Org. Electron.* **59**, (2018).

61. Wang, J. T., Ball, J. M., Barea, E. M., Abate, A. & Alexander-, J. a. Supporting Information For : Low-temperature processed electron collection layers of Graphene / TiO<sub>2</sub> nanocomposites in thin film perovskite solar cells. *Nano Lett.* **14**, (2013).
62. Chen, B., Yang, M., Priya, S. & Zhu, K. Origin of J-V Hysteresis in Perovskite Solar Cells. *Journal of Physical Chemistry Letters* (2016). doi:10.1021/acs.jpclett.6b00215
63. Park, Y. H. *et al.* Inorganic Rubidium Cation as an Enhancer for Photovoltaic Performance and Moisture Stability of HC(NH<sub>2</sub>)<sub>2</sub>PbI<sub>3</sub> Perovskite Solar Cells. *Adv. Funct. Mater.* (2017). doi:10.1002/adfm.201605988
64. Yadav, P. *et al.* The Role of Rubidium in Multiple-Cation-Based High-Efficiency Perovskite Solar Cells. *Adv. Mater.* (2017). doi:10.1002/adma.201701077
65. Zheng, F. *et al.* Triggering the Passivation Effect of Potassium Doping in Mixed-Cation Mixed-Halide Perovskite by Light Illumination. *Adv. Energy Mater.* **9**, (2019).
66. Yang, Y. *et al.* Beneficial effects of potassium iodide incorporation on grain boundaries and interfaces of perovskite solar cells. *RSC Adv.* **9**, (2019).
67. Zhu, H. *et al.* Synergistic Effect of Fluorinated Passivator and Hole Transport Dopant Enables Stable Perovskite Solar Cells with an Efficiency near 24%. *J. Am. Chem. Soc.* **143**, (2021).
68. Han, Q. *et al.* Single Crystal Formamidinium Lead Iodide (FAPbI<sub>3</sub>): Insight into the Structural, Optical, and Electrical Properties. *Adv. Mater.* (2016). doi:10.1002/adma.201505002
69. Stoumpos, C. C., Malliakas, C. D. & Kanatzidis, M. G. Semiconducting tin and lead iodide perovskites with organic cations: Phase transitions, high mobilities, and near-infrared photoluminescent properties. *Inorg. Chem.* (2013). doi:10.1021/ic401215x
70. Yoo, J. J. *et al.* Efficient perovskite solar cells via improved carrier management. *Nature* **590**, (2021).
71. Conings, B. *et al.* Intrinsic Thermal Instability of Methylammonium Lead Trihalide Perovskite. *Adv. Energy Mater.* (2015). doi:10.1002/aenm.201500477
72. Saliba, M. *et al.* Cesium-containing triple cation perovskite solar cells: improved



- stability, reproducibility and high efficiency. *Energy Environ. Sci.* (2016). doi:10.1039/C5EE03874J
73. Yao, D. *et al.* Hindered Formation of Photoinactive  $\delta$ -FAPbI<sub>3</sub> Phase and Hysteresis-Free Mixed-Cation Planar Heterojunction Perovskite Solar Cells with Enhanced Efficiency via Potassium Incorporation. *J. Phys. Chem. Lett.* (2018). doi:10.1021/acs.jpclett.8b00830
74. Kubicki, D. J. *et al.* Phase Segregation in Cs-, Rb- and K-Doped Mixed-Cation (MA)<sub>x</sub>(FA)<sub>1-x</sub>PbI<sub>3</sub> Hybrid Perovskites from Solid-State NMR. *J. Am. Chem. Soc.* (2017). doi:10.1021/jacs.7b07223
75. Alanazi, T. I. *et al.* Potassium iodide reduces the stability of triple-cation perovskite solar cells. *RSC Adv.* **10**, (2020).
76. Nam, J. K. *et al.* Potassium Incorporation for Enhanced Performance and Stability of Fully Inorganic Cesium Lead Halide Perovskite Solar Cells. *Nano Lett.* (2017). doi:10.1021/acs.nanolett.7b00050
77. Muzammal uz Zaman, M. *et al.* Potassium doped methylammonium lead iodide (MAPbI<sub>3</sub>) thin films as a potential absorber for perovskite solar cells; structural, morphological, electronic and optoelectric properties. *Phys. B Condens. Matter* (2017). doi:10.1016/j.physb.2017.07.067
78. Son, D.-Y. *et al.* Universal Approach toward Hysteresis-Free Perovskite Solar Cell via Defect Engineering. *J. Am. Chem. Soc.* (2018). doi:10.1021/jacs.7b10430
79. Tang, Z. *et al.* Hysteresis-free perovskite solar cells made of potassium-doped organometal halide perovskite. *Sci. Rep.* (2017). doi:10.1038/s41598-017-12436-x
80. Tiep, N. H., Ku, Z. & Fan, H. J. Recent Advances in Improving the Stability of Perovskite Solar Cells. *Adv. Energy Mater.* (2016). doi:10.1002/aenm.201501420
81. Bush, K. A. *et al.* Thermal and Environmental Stability of Semi-Transparent Perovskite Solar Cells for Tandems Enabled by a Solution-Processed Nanoparticle Buffer Layer and Sputtered ITO Electrode. doi:10.1002/adma.201505279
82. Domanski, K. *et al.* Not All That Glitters Is Gold: Metal-Migration-Induced Degradation

- in Perovskite Solar Cells. *ACS Nano* (2016). doi:10.1021/acsnano.6b02613
83. Sheikh, A. D. *et al.* Effects of High Temperature and Thermal Cycling on the Performance of Perovskite Solar Cells: Acceleration of Charge Recombination and Deterioration of Charge Extraction. *ACS Appl. Mater. Interfaces* (2017). doi:10.1021/acsami.7b11250
  84. Kojima, A., Teshima, K., Shirai, Y. & Miyasaka, T. Organometal halide perovskites as visible-light sensitizers for photovoltaic cells. *J. Am. Chem. Soc.* (2009). doi:10.1021/ja809598r
  85. NREL. Solar cell efficiency chart. *Sol. cell Effic. chart* (2017).
  86. Pellet, N. *et al.* Mixed-organic-cation perovskite photovoltaics for enhanced solar-light harvesting. *Angew. Chemie - Int. Ed.* (2014). doi:10.1002/anie.201309361
  87. Jeon, N. J. *et al.* Compositional engineering of perovskite materials for high-performance solar cells. *Nature* (2015). doi:10.1038/nature14133
  88. Ibrahim Dar, M. *et al.* Understanding the Impact of Bromide on the Photovoltaic Performance of CH<sub>3</sub>NH<sub>3</sub>PbI<sub>3</sub> Solar Cells. *Adv. Mater.* (2015). doi:10.1002/adma.201503124
  89. Yang, W. S. *et al.* Iodide management in formamidinium-lead-halide-based perovskite layers for efficient solar cells. *Science* (80-. ). (2017). doi:10.1126/science.aan2301
  90. Xie, L. Q. *et al.* Understanding the Cubic Phase Stabilization and Crystallization Kinetics in Mixed Cations and Halides Perovskite Single Crystals. *J. Am. Chem. Soc.* (2017). doi:10.1021/jacs.6b12432
  91. Kulkarni, S. A. *et al.* Band-gap tuning of lead halide perovskites using a sequential deposition process. *J. Mater. Chem. A* (2014). doi:10.1039/c4ta00435c
  92. Albadri, A. *et al.* Unraveling the Impact of Rubidium Incorporation on the Transport-Recombination Mechanisms in Highly Efficient Perovskite Solar Cells by Small-Perturbation Techniques. *J. Phys. Chem. C* (2017). doi:10.1021/acs.jpcc.7b04766
  93. Dong, Q. *et al.* Electron-hole diffusion lengths > 175  $\mu$ m in solution-grown CH<sub>3</sub>NH<sub>3</sub>PbI<sub>3</sub> single crystals. *Science* (80-. ). (2015). doi:10.1126/science.aaa5760

94. Bag, M. *et al.* Kinetics of Ion Transport in Perovskite Active Layers and Its Implications for Active Layer Stability. *J. Am. Chem. Soc.* (2015). doi:10.1021/jacs.5b08535
95. Lee, H. *et al.* Direct Experimental Evidence of Halide Ionic Migration under Bias in CH<sub>3</sub>NH<sub>3</sub>PbI<sub>3</sub>-xCl<sub>x</sub>-Based Perovskite Solar Cells Using GD-OES Analysis. *ACS Energy Lett.* (2017). doi:10.1021/acsenergylett.7b00150
96. Zhang, T. *et al.* Understanding the relationship between ion migration and the anomalous hysteresis in high-efficiency perovskite solar cells: A fresh perspective from halide substitution. *Nano Energy* (2016). doi:10.1016/j.nanoen.2016.05.052
97. Walsh, A., Scanlon, D. O., Chen, S., Gong, X. G. & Wei, S. H. Self-regulation mechanism for charged point defects in hybrid halide perovskites. *Angew. Chemie - Int. Ed.* (2015). doi:10.1002/anie.201409740
98. E, W., Ren, W. & Vanden-Eijnden, E. Simplified and improved string method for computing the minimum energy paths in barrier-crossing events. *J. Chem. Phys.* (2007). doi:10.1063/1.2720838
99. Meloni, S. *et al.* Ionic polarization-induced current-voltage hysteresis in CH<sub>3</sub>NH<sub>3</sub>PbX<sub>3</sub>perovskite solar cells. *Nat. Commun.* (2016). doi:10.1038/ncomms10334
100. Perdew, J. P. & Burke, K. Generalized gradient approximation for the exchange-correlation hole of a many-electron system. *Phys. Rev. B - Condens. Matter Mater. Phys.* (1996). doi:10.1103/PhysRevB.54.16533
101. Monkhorst, H. & Pack, J. Special points for Brillouin zone integrations. *Phys. Rev. B* (1976). doi:10.1103/PhysRevB.13.5188
102. Shi, T., Yin, W.-J. & Yan, Y. Predictions for p-Type CH<sub>3</sub>NH<sub>3</sub>PbI<sub>3</sub> Perovskites. *J. Phys. Chem. C* (2014). doi:10.1021/jp508328u
103. Gra, C., Zakeeruddin, S. M., Ro, U. & Gra, M. Entropic Stabilization of Mixed A-Cation ABX<sub>3</sub> Metal Halide Perovskites for High Performance Perovskite Solar Cells. *Energy Environ. Sci.* (2016). doi:10.1039/C5EE03255E
104. Meloni, S., Palermo, G., Ashari-Astani, N., Grätzel, M. & Rothlisberger, U. Valence and conduction band tuning in halide perovskites for solar cell applications. *J. Mater.*

*Chem. A* (2016). doi:10.1039/c6ta04949d

105. Ashari Astani, N. *et al.* Computational Characterization of the Dependence of Halide Perovskite Effective Masses on Chemical Composition and Structure. *J. Phys. Chem. C* (2017). doi:10.1021/acs.jpcc.7b04898
106. Freysoldt, C., Neugebauer, J. & Van De Walle, C. G. Fully Ab initio finite-size corrections for charged-defect supercell calculations. *Phys. Rev. Lett.* (2009). doi:10.1103/PhysRevLett.102.016402
107. Castelli, I. E., García-Lastra, J. M., Thygesen, K. S. & Jacobsen, K. W. Bandgap calculations and trends of organometal halide perovskites. *APL Mater.* **2**, (2014).
108. Lin, Q., Armin, A., Nagiri, R. C. R., Burn, P. L. & Meredith, P. Electro-optics of perovskite solar cells. *Nat. Photonics* **9**, (2015).
109. Anaraki, E. H. *et al.* Highly efficient and stable planar perovskite solar cells by solution-processed tin oxide. *Energy Environ. Sci.* (2016). doi:10.1039/C6EE02390H
110. Liu, N. *et al.* TiO<sub>2</sub>/Mg-SnO<sub>2</sub> nanoparticle composite compact layer for enhancing the performance of perovskite solar cells. *Opt. Mater. Express* **10**, (2020).
111. Son, D. Y., Im, J. H., Kim, H. S. & Park, N. G. 11% efficient perovskite solar cell based on ZnO nanorods: An effective charge collection system. *J. Phys. Chem. C* **118**, (2014).
112. Sadegh, F. *et al.* Highly efficient, stable and hysteresis-less planar perovskite solar cell based on chemical bath treated Zn<sub>2</sub>SnO<sub>4</sub> electron transport layer. *Nano Energy* **75**, (2020).
113. Oh, L. S. *et al.* Zn<sub>2</sub>SnO<sub>4</sub>-based photoelectrodes for organolead halide perovskite solar cells. *J. Phys. Chem. C* **118**, (2014).
114. Bera, A. *et al.* Fast Crystallization and Improved Stability of Perovskite Solar Cells with Zn<sub>2</sub>SnO<sub>4</sub> Electron Transporting Layer: Interface Matters. *ACS Appl. Mater. Interfaces* **7**, (2015).
115. Li, Z. Stable perovskite solar cells based on WO<sub>3</sub> nanocrystals as hole transport layer. *Chem. Lett.* **44**, (2015).

116. You, Y. *et al.* TiO<sub>2</sub>/WO<sub>3</sub> Bilayer as Electron Transport Layer for Efficient Planar Perovskite Solar Cell with Efficiency Exceeding 20%. *Adv. Mater. Interfaces* **7**, (2020).
117. Zhang, J., Shi, C., Chen, J., Wang, Y. & Li, M. Preparation of ultra-thin and high-quality WO<sub>3</sub> compact layers and comparison of WO<sub>3</sub> and TiO<sub>2</sub> compact layer thickness in planar perovskite solar cells. *J. Solid State Chem.* **238**, (2016).
118. Qin, M. *et al.* Perovskite Solar Cells Based on Low-Temperature Processed Indium Oxide Electron Selective Layers. *ACS Appl. Mater. Interfaces* **8**, (2016).
119. Apostolopoulou, A., Sygkridou, D., Rapsomanikis, A., Kalarakis, A. N. & Stathatos, E. Enhanced performance of mesostructured perovskite solar cells in ambient conditions with a composite TiO<sub>2</sub>–In<sub>2</sub>O<sub>3</sub> electron transport layer. *Sol. Energy Mater. Sol. Cells* **166**, (2017).
120. Yin, G., Steigert, A., Manley, P., Klenk, R. & Schmid, M. Enhanced absorption in tandem solar cells by applying hydrogenated In<sub>2</sub>O<sub>3</sub> as electrode. *Appl. Phys. Lett.* **107**, (2015).
121. Neophytou, M. *et al.* Enhancing the Charge Extraction and Stability of Perovskite Solar Cells Using Strontium Titanate (SrTiO<sub>3</sub>) Electron Transport Layer. *ACS Appl. Energy Mater.* (2019). doi:10.1021/acsaem.9b01567
122. Bera, A. *et al.* Perovskite oxide SrTiO<sub>3</sub> as an efficient electron transporter for hybrid perovskite solar cells. *J. Phys. Chem. C* **118**, (2014).
123. Shen, D., Zhang, W., Li, Y., Abate, A. & Wei, M. Facile Deposition of Nb<sub>2</sub>O<sub>5</sub> Thin Film as an Electron-Transporting Layer for Highly Efficient Perovskite Solar Cells. *ACS Appl. Nano Mater.* **1**, (2018).
124. Ling, X. *et al.* Room-Temperature Processed Nb<sub>2</sub>O<sub>5</sub> as the Electron-Transporting Layer for Efficient Planar Perovskite Solar Cells. *ACS Appl. Mater. Interfaces* **9**, (2017).
125. Kogo, A., Numata, Y., Ikegami, M. & Miyasaka, T. Nb<sub>2</sub>O<sub>5</sub> blocking layer for high open-circuit voltage perovskite solar cells. *Chem. Lett.* **44**, (2015).
126. Wang, X. *et al.* Cerium oxide standing out as an electron transport layer for efficient and stable perovskite solar cells processed at low temperature. *J. Mater. Chem. A* **5**,

- (2017).
127. Zhu, L. *et al.* Mesoporous BaSnO<sub>3</sub> layer based perovskite solar cells. *Chem. Commun.* **52**, (2016).
  128. Shin, S. S. *et al.* Colloidally prepared La-doped BaSnO<sub>3</sub> electrodes for efficient, photostable perovskite solar cells. *Science (80-. ).* **356**, (2017).
  129. Okamoto, Y. & Suzuki, Y. Mesoporous BaTiO<sub>3</sub>/TiO<sub>2</sub> Double Layer for Electron Transport in Perovskite Solar Cells. *J. Phys. Chem. C* **120**, (2016).
  130. Abdi-Jalebi, M. *et al.* Impact of a Mesoporous Titania-Perovskite Interface on the Performance of Hybrid Organic-Inorganic Perovskite Solar Cells. *J. Phys. Chem. Lett.* **7**, (2016).
  131. Roose, B. *et al.* Mesoporous SnO<sub>2</sub> electron selective contact enables UV-stable perovskite solar cells. *Nano Energy* **30**, (2016).
  132. Dong, Q. *et al.* Insight into perovskite solar cells based on SnO<sub>2</sub> compact electron-selective layer. *J. Phys. Chem. C* **119**, (2015).
  133. Corrigendum: Enhanced electron extraction using SnO<sub>2</sub> for high-efficiency planar-structure HC(NH<sub>2</sub>)<sub>2</sub>PbI<sub>3</sub>-based perovskite solar cells (Nature Energy (2017) 2 (16177)). *Nature Energy* **2**, (2017).
  134. Thomas, B. & Skariah, B. Spray deposited Mg-doped SnO<sub>2</sub> thin film LPG sensor: XPS and EDX analysis in relation to deposition temperature and doping. *J. Alloys Compd.* **625**, (2015).
  135. Chiodini, N., Paleari, A., Dimartino, D. & Spinolo, G. SnO<sub>2</sub> nanocrystals in SiO<sub>2</sub>: A wide-band-gap quantum-dot system. *Appl. Phys. Lett.* **81**, (2002).
  136. Kim, G. *et al.* Impact of strain relaxation on performance of a-formamidinium lead iodide perovskite solar cells. *Science (80-. ).* **370**, (2020).
  137. Amalathas, A. P. *et al.* Elucidating the role of TiCl<sub>4</sub> post-treatment on percolation of TiO<sub>2</sub> electron transport layer in perovskite solar cells. *J. Phys. D. Appl. Phys.* **53**, (2020).

138. Murakami, T. N. *et al.* Adjustment of Conduction Band Edge of Compact TiO<sub>2</sub> Layer in Perovskite Solar Cells Through TiCl<sub>4</sub> Treatment. *ACS Appl. Mater. Interfaces* **9**, (2017).
139. Yella, A., Heiniger, L. P., Gao, P., Nazeeruddin, M. K. & Grätzel, M. Nanocrystalline rutile electron extraction layer enables low-temperature solution processed perovskite photovoltaics with 13.7% efficiency. *Nano Lett.* **14**, (2014).
140. Dar, M. I., Chandiran, A. K., Grätzel, M., Nazeeruddin, M. K. & Shivashankar, S. A. Controlled synthesis of TiO<sub>2</sub> nanoparticles and nanospheres using a microwave assisted approach for their application in dye-sensitized solar cells. *J. Mater. Chem. A* **2**, (2014).

## Education

---

- June 2017-  
Present      **École Polytechnique Fédérale de Lausanne, EPFL, Laussane, Switzerland** *Doctor of Philosophy (PhD)*  
  
Department of Chemistry and Chemical Engineering  
  
Supervisor: Professor Anders Hagfeldt and Prof Michael Graetzel
- Jul 2016-  
Feb 2017      **Nanyang Technical University, Singapore**  
  
Research Assistant  
  
Supervisor: Prof. Subodh Mhaishalkar
- Jul 2011-  
May 2016      **Indian Institute of Technology Bombay, Mumbai, India**  
*Bachelor of Technology and Master of Technology*  
Department of Energy Science and Engineering  
  
Supervisor: Prof. Aswini Yella

## Publications

- Agarwalla, A., Ryusuke, U., Meloni, S., Uhl, A., Milic, J., Krishna, A., Zakeeruddin, S.M., Hagfeldt, A., Graetzel, M. Reduced halide diffusion in triple cation perovskite solar cells for improved charge extraction and operational stability. (2021) (to be submitted)
- Agarwalla, A., Krishna, A., Felix, K., Zakeeruddin, S.M., Hagfeldt, A., Graetzel, M. TiO<sub>2</sub> colloids as low temperature alternative to mesoporous TiO<sub>2</sub>. (2021) (to be submitted)
- Zhao, L., Pengyi, T., Deying, L., Dar, I.M., Arora, N., Hu, Q., Luo, J., Agarwalla, A., Liu, Y., Zakeeruddin, S.M., Hagfeldt, A., Arbiol, J., Huang, W., Gong, Q., Russell, T.P., Friend, R., Grätzel, M., Zhu, R. Enabling Grain Boundary Mitigation in Polycrystalline Perovskite Solids. *Nature* (submitted 2020)
- Lu, H. *et al.* Vapor-assisted deposition of highly efficient, stable black-phase FAPbI<sub>3</sub> perovskite solar cells. *Science* **370**, (2020).
- Tres, W. *et al.* Performance of perovskite solar cells under simulated temperature-illumination real-world operating conditions. *Nature Energy* **4**, (2019)



Xie, H. *et al.* Decoupling the effects of defects on efficiency and stability through phosphonates in stable halide perovskite solar cells. *Joule* **5**, (2021)

Zhang, J. *et al.* Intermediate Phase Enhances Inorganic Perovskite and Metal Oxide Interface for Efficient Photovoltaics. *Joule* **4**, (2020)